Imperial College London

Investigation of the Cryogenic Deformation Behaviour and Subsequent Recrystallization in Magnesium Alloy AZ31

By

KAI ZHANG

A thesis submitted for the degree of Doctor of Philosophy of Imperial College London

Department of Mechanical Engineering

Imperial College London

April 2021

Declaration of Originality

I, Kai Zhang, declare that the work presented in this thesis is my own and all resources that I used or quoted have been referenced appropriately.

Copyright Declaration

Abstract

Magnesium alloys attract great interest from industry and academia, as they are the lightest structural metals, which can be applied to achieve a weight reduction of car bodies to reduce energy consumption and air pollution. However, their ductility and strength are generally poor at room temperature, mainly because of their coarse grains and strong texture. This study aims to develop a novel method to refine grains and weaken the texture in magnesium (Mg) alloy AZ31, and investigate its underlying deformation and recrystallization mechanisms. This can contribute to improving the applications of Mg alloys.

For this purpose, the hot deformation with pre-deformation at cryogenic temperature (CT) and room temperature (RT) was conducted and compared to the direct-hot-deformed Mg alloy. Recrystallization mainly occurred near deformation bands in RT-hot-deformed and direct-hot-deformed samples, while active recrystallization occurred near twin-twin interactions in the CT-hot-deformed sample. This resulted in finer grains and a weaker texture in the CT-hot-deformed sample, and its ductility and strength improved significantly.

The pre-deformation behaviour at CT and RT was investigated with a *quasi-in-situ* Electron Backscatter Diffraction (EBSD). More twin-twin interactions were observed at CT than RT, which contributed to forming a weaker texture and finer twins, and higher hardening rates at CT. To further investigate how twinning and deformation bands evolve, rolling tests at CT and RT were conducted. With increasing strain, abundant deformation bands, evolving from $\{10\bar{1}1\}$-$\{10\bar{1}2\}$ double twins, were observed in RT-rolled samples, while abundant twins, starting from $\{10\bar{1}2\}$ tension twins to twin-twin interactions and twinning sequence, were observed in CT-rolled samples. During the subsequent annealing process, recrystallization occurred around deformation bands in the annealed RT-rolled sample, resulting in a strong basal texture. However, recrystallization occurred around twin-twin interactions in the annealed CT-rolled sample, forming the weak texture and fine grains.

Publications

- **Kai Zhang**, Zhutao Shao, Christopher Daniel, Mark Turski, Catalin Pruncu, Lihui Lang, Joseph Robson, Jun Jiang, A comparative study of plastic deformation mechanisms in room-temperature and cryogenically deformed magnesium alloy AZ31, Materials Science and Engineering: A. 2021, 807: 140821.
- **Kai Zhang**, Zhutao Shao, Jun Jiang, Effects of twin-twin interactions and deformation bands on the nucleation of recrystallization in AZ31 magnesium alloy, Materials & Design. 2020, 194: 108936.
- **Kai Zhang**, Jinghua Zheng, Yan Huang, Jun Jiang, Evolution of twinning and shear bands in magnesium alloys during cryo-rolling process, Materials & Design. 2020, 193: 108793.
- **Kai Zhang**, Jinghua Zheng, Zhutao Shao, Catalin Pruncu, Mark Turski, Carlos Guerini, Jun Jiang, Experimental investigation of the viscoplastic behaviours and microstructure evolutions of AZ31B and Elektron 717 Mg-alloys, Materials & Design. 2019, 184: 108160.
- **Kai Zhang**, Jinghua Zheng, Christopher Hopper, Jun Jiang, Enhanced plasticity at cryogenic temperature in a magnesium alloy, Materials Science and Engineering: A. 2021, 811: 141001.
- **Kai Zhang**, Zhutao Shao, Jun Jiang, Achieving fine grains and a weak texture in magnesium alloy AZ31 by cryogenic-hot deformation, Acta Materialia. (Manuscript Number: AM-S-20-03694) (Submitted)
- **Kai Zhang**, Jinghua Zheng, Jun Jiang, Enhancement of mechanical properties in magnesium alloys, Scripta Materialia. (In preparation)
- **Kai Zhang,** Jun Jiang, Effects of grain size and temperature on slip and twinning activity in a magnesium alloy, Acta Materialia. (In preparation)

- Jinghua Zheng, Catalin Pruncu, **Kai Zhang**, Kailun Zheng, Jun Jiang, Quantifying Geometrically Necessary Dislocation Density during Hot Deformation in AA6082 Al Alloy, Materials Science and Engineering: A. 2021, 814: 141158.
- Xinyu Ren, Chong Pei, Huaping Xiong, Yonglai Shang, **Kai Zhang**, Dong Liu, Jinghua Zheng, Jianguo Lin, Jun Jiang, Microstructure evolution and mechanical properties of Ti2AlNb/TiAl brazed joint using a novel Ti-Ni-Nb-Zr filler, Progress in Natural Science: Materials International, 2020, 30(3): 410-416.
- Lili Guo, Jingru Yuan, Jiuyang Pei, Ying Zhao, **Kai Zhang**, Jun Jiang, Study of the microstructure, bonding evolution and mechanical properties of continuously extruded magnesium AZ31 sheet, Materials Science and Engineering: A. 2021, 819: 141456.

Presentations

- **Kai Zhang**, Zhutao Shao, Christopher Daniel, Mark Turski, Catalin Pruncu, Lihui Lang, Joseph Robson, Jun Jiang, "The Competition between Twinning and Dislocation Slips in Magnesium Alloys at Cryogenic Temperatures", *the 3rd International Conference on Light Materials – Science and Technology 2019 (LightMAT 2019)*, Manchester, United Kingdom, November 2019.
- **Kai Zhang**, Jianguo Lin, Jun Jiang, "Investigation of Cryogenic Deformation Behaviour and Subsequent Recrystallization in Magnesium Alloys", *Oral presentations in Lightform (EPSRC) technical meeting*, London, United Kingdom, October 2020.
- **Kai Zhang**, Jun Jiang, "Cryogenic deformation with subsequent recrystallization in magnesium alloys", *Oral presentations in Lightform (EPSRC) technical meeting*, Manchester, United Kingdom, September 2019.
- **Kai Zhang**, Jianguo Lin, Jun Jiang, "Microstructure Evolution in the Thermal-Mechanical and Cryogenic Tests of Magnesium alloys", *Oral presentations in Lightform (EPSRC) technical meeting*, Cambridge, United Kingdom, September 2018.
- **Kai Zhang**, Jun Jiang, "Study the thermal-mechanical behaviours of magnesium alloys", *Oral presentations in Designing alloys for resource efficiency (DARE) (EPSRC) technical meeting*, Sheffield, United Kingdom, June 2018.
- **Kai Zhang**, Jun Jiang, "Overview of magnesium alloys", *Oral presentations in Designing alloys for resource efficiency (DARE) (EPSRC) technical meeting*, London, United Kingdom, November 2017.

Acknowledgement

I would like to thank my supervisor Dr. Jun Jiang for giving me the valuable opportunity to do a PhD and supporting my research with continuous guidance, patience and knowledge. I enjoyed doing my PhD under his supervision and learned a lot of research skills. I would also like to thank Prof. Jianguo Lin for giving me many useful and valuable suggestions for my research work. I am grateful to the financial support from the President's PhD Scholarship of Imperial College London.

I am also grateful to Prof. Fionn Dunne, Dr. Ben Britton in the Department of Materials, and Prof. Joseph Robson, Prof. João Quinta da Fonseca in The University of Manchester for their helpful suggestions and discussions. I would like to thank all of my colleagues and collaborators including Dr. Jinghua Zheng, Dr. Zhutao Shao, Dr. Catalin Pruncu, Dr. Christopher Stuart Daniel, Dr. Nan Li, Dr. Zhusheng Shi, Dr. Kailun Zheng, Dr. Junquan Yu, Dr Haoxiang Gao, Dr. Christopher Hopper, Dr. Qinmeng Luan, Dr. Yasmeen Tabassam, Dr. Fengzhen Sun, Xianyan Zhou, Zinong Tan, Yuehan Liu, Yaping Wang for helping with my research work.

I would like to thank all the technical staff in Imperial College London, Dr. Ruth Brooker, Dr. Alex Toth, Suresh Viswanathan Chettiar, Amit Choda, Mark Holloway, Tony Willis and Susan Peneycad, for their help on my experimental work.

Finally, I am very grateful to my parents, my families, and my girlfriend for providing my strongest supports and love. I offer my best wishes and blessings to all of you. Thank you.

Contents

Declaration of Originality 2

Copyright Declaration 3

Abstract 4

Publications 5

Presentations 7

Acknowledgement 8

Contents 9

List of Figures 15

List of Tables 24

List of Acronyms 25

1 Introduction 27

1.1 Background 27

1.2 Aims and objectives of the research 28

1.3 Thesis structure 29

2 Literature review 32

2.1 Deformation modes 32

2.1.1 Dislocation slip 32

2.1.2 Twinning 33

2.2 Effects of grain size and texture on mechanical properties 35

2.2.1 Grain size effects 36

2.2.2 Texture effects 38

2.3 Typical microstructures in the deformation process 40
2.3.1 Twin-twin interactions 41
2.3.2 Twinning sequence 42
2.3.3 Deformation bands 45
2.3.4 Shear bands 46
2.4 Effects of temperature on microstructures 47
2.4.1 Temperature effects on slip and twinning 47
2.4.2 Cryogenic deformation 49
2.5 Recrystallization mechanisms 51
2.5.1 Recrystallization nucleation sites 52
2.5.2 Twinning-induced dynamic recrystallization 55
2.6 Summary 58
3 Material and experimental methods 59
3.1 Material 59
3.2 Mechanical tests 59
3.2.1 Compression tests 59
3.2.2 Tensile tests 61
3.2.3 Rolling tests 62
3.3 Microstructure characterization 63
3.3.1 Electron Backscattered Diffraction (EBSD) 63
3.3.2 Etching and optical microscopy 66
4 A novel cryogenic-hot deformation method to achieve fine grains and a weak texture in Mg alloy AZ31 67
4.1 Introduction 67

4.2 Experimental programme....68
4.2.1 Material and experimental tests....68
4.2.2 Microstructure characterisation....69
4.3 Experimental results....70
4.3.1 Mechanical behaviours of deformed Mg alloy AZ31....70
4.3.2 Microstructural behaviours in the hot-deformed samples with pre-deformation....71
4.3.3 Microstructural evolution during cryogenic deformation and subsequent dynamic recrystallization....74
4.3.4 Microstructures in the hot deformation process for the direct-HD and RT-HD samples....77
4.4 Discussion....80
4.4.1 Recrystallization near twins in the CT-HD sample during hot deformation....80
4.4.2 Recrystallization in the direct-HD and RT-HD samples during hot deformation....81
4.4.3 Enhancement of ductility and strength in the hot-deformed sample with cryogenic pre-deformation....83
4.5 Summary....84
5 Deformation behaviour of Mg alloy AZ31 at cryogenic temperature....86
5.1 Introduction....86
5.2 Experimental programme....87
5.2.1 Material and experimental tests....87
5.2.2 EBSD measurements....88
5.3 Results....90
5.3.1 Mechanical behaviours of Mg alloy AZ31 at room and cryogenic temperature....90
5.3.2 Microstructure evolution of Mg alloy AZ31 at room and cryogenic temperature 91
5.3.3 Twinning behaviour of Mg alloy AZ31 at room and cryogenic temperature....95

5.3.4 Twinning and KAM behaviours of Mg alloy AZ31 at room and cryogenic temperature 98
5.4 Discussion 100
5.5 Summary 105
6 Microstructure evolution during the cryogenic rolling process 107
6.1 Introduction 107
6.2 Experimental programme 108
6.2.1 Materials and experimental tests 108
6.2.2 Microstructure characterisation 109
6.3 Results 109
6.3.1 Microstructure evolution of Mg alloy AZ31 during the RT-rolling and CT-rolling process 109
6.3.2 Typical zone analysis in the 13% RT-rolled and 13% CT-rolled Mg alloy AZ31 samples 115
6.3.3 Twinning sequence analysis 118
6.4 Discussion 121
6.4.1 Illustration of the microstructure evolution during the RT-rolling and CT-rolling process 121
6.4.2 Twinning behaviours during the CT-rolling process 123
6.4.3 Deformation bands formation during the RT-rolling process 125
6.5 Summary 127
7 Recrystallization mechanisms in twin-twin interactions and deformation bands 128
7.1 Introduction 128
7.2 Experimental programme 128

7.2.1 Material and experimental tests 128
7.2.2 Microstructure characterisation 130
7.3 Experimental results 131
7.3.1 The microstructures of the RT-rolled and CT-rolled samples 131
7.3.2 Microstructure evolution during the annealing process 132
7.3.3 Texture evolution and its mechanisms during the annealing process 134
7.3.4 Typical deformation structures in the RT-rolled and CT-rolled samples 138
7.3.5 Recrystallization in different deformation structures 139
7.3.6 Grain size evolution during the annealing process 143
7.4 Discussion 144
7.4.1 Illustration of recrystallization mechanisms in the annealed RT-rolled and CT-rolled samples 144
7.4.2 Recrystallization and texture evolution of the RT-rolled sample during the subsequent annealing process 146
7.4.3 Recrystallization and texture evolution of the CT-rolled sample during the subsequent annealing process 147
7.5 Summary 150
8 Conclusions and future work 151
8.1 Conclusions 151
8.1.1 A novel cryogenic-hot deformation method to achieve fine grains and a weak texture in Mg alloys 151
8.1.2 Deformation mechanisms at cryogenic and room temperature 151
8.1.3 Evolution of twin-twin interactions, twinning sequence and deformation bands 152
8.1.4 Recrystallization mechanisms in twin-twin interactions and deformation bands 152
8.2 Suggestions for future work 153

8.2.1 The improvement of the cryogenic-hot deformation method 153

8.2.2 The modelling of cryogenic deformation 153

8.2.3 Investigation of grain size and texture effects on deformation mechanisms in Mg alloys at cryogenic temperature 154

Reference 155

Appendix A. Grain size distribution and texture in the hot-deformed samples..... 166

Appendix B. The microstructure during the RT-rolling and CT-rolling processes 167

Appendix C. The microstructure evolution in the RT-rolled and CT-rolled samples during the annealing process 170

List of Figures

Figure 1.1 Flowchart showing the logical link of Chapter 4-7. 30

Figure 2.1 Basal, prismatic, pyramidal <a> slip systems, and first- and second-order pyramidal <c+a> slip systems in HCP materials. Shaded planes represent the slip planes, while arrows represent the Burgers vector directions [30]. 33

Figure 2.2 Schematic of (a) $\{10\bar{1}2\}$ tension twin and (b) $\{10\bar{1}1\}$ compression twin modes in Mg. Shaded planes represent the twin planes, while arrows represent the twinning shear directions [33]. 34

Figure 2.3 True-stress versus true-strain curves for rolled samples subjected to the plane-strain compression with c-axis extension and c-axis compression [41]. 35

Figure 2.4 Room-temperature tensile strain failure, as a measure of ductility, versus grain size in selected polycrystalline Mg and Mg alloys [10]. 38

Figure 2.5 Texture formation of rolled magnesium [56]. 39

Figure 2.6 Tensile elongations of the rolled Mg alloy AZ31 sheets as a function of pole intensity in (0002) pole figures. Tensile specimens were cut along planes coinciding with the rolling direction (0°) and at angles of 45° and 90° (transverse) to the rolling direction [59]. 40

Figure 2.7 Experimentally observed twin-twin interaction in single-crystal magnesium compressed along $[10\,\bar{1}\,0]$ direction [60]. (b) Schematic representation of the twin-twin interaction considered here, formed by tension twin variants T1 $(10\bar{1}2)$ and T4 $(\bar{1}012)$. Scale bar, 300 μm [61]. 41

Figure 2.8 Double tension twin structures in the magnesium specimen loaded along the [0001] direction. The secondary twin does not connect to an incoming twin: (a) a secondary twin T_{54} inside a primary twin T_5 and (b) three secondary twins T_{31} inside a primary twin T_3. The secondary twin connects to twin-twin boundaries: (c) a secondary twin T_{12} inside a primary twin T_1 and (d) two secondary twins T_{62} inside a primary twin T_6 [60]. 44

Figure 2.9 The various features are shown at an increasing scale: (a) dislocations, (b) dislocation boundaries, (c) deformation bands within a grain, (d) specimen- and grain-scale shear bands [73]. 46

Figure 2.10 Schematic illustrations showing the effect of temperature on twinning and slip [82]. 48

Figure 2.11 Estimated CRSS of the slip and twinning systems in Mg at 1% strain [35]. 49

Figure 2.12 EBSD image quality maps of the titanium rolled to thickness reductions of 5%, 10%, 15% and 20%: (a) room-temperature rolling; (b) cryogenic-temperature rolling [72]. .51

Figure 2.13 Quasi-in-situ EBSD orientation maps in cold-rolled (23% thickness reduction) samples of (a) Mg-0.4Zn, and recrystallized grains after annealing at 350 ℃ for (b) 5 s and (c) 600 s for Mg-0.4Zn alloy (d, e) (0002) pole figures showing textures of recrystallized grains in maps (b, c) respectively [90].....53

Figure 2.14 (a) c-axis orientation map and (b) corresponding (0002) and $\{11\bar{2}0\}$ pole figures showing the orientations associated with the deformed matrix and the recrystallized twin band at 370 ℃ and a compressive strain of 1 [96]. 56

Figure 2.15 (a) EBSD-Kikuchi band contrast map revealing recrystallized twins and $\{10\bar{1}2\}$ tension twins; (b) detailed view of a recrystallized twin indicating the presence of some low angle grain boundaries (thin lines) within the recrystallized structure comprised of high angle grain boundaries (bold lines); (c) neighbouring tension twin showing no recrystallization [98]. 57

Figure 3.1 Set-up of facilities for the cryogenic compression experiment. 60

Figure 3.2 (a) Set-up of facilities for the hot compression experiment with Gleeble 3800 thermo-mechanical materials simulator. (b) Test chamber and a sample with thermo-couples. 61

Figure 3.3 (a) Set-up of facilities for the tensile micro-test. (b) Micro-test machine. 62

Figure 3.4 Set-up of facilities for the rolling tests at room and cryogenic temperature, and the subsequent annealing process of the rolled samples. 63
Figure 3.5 Schematic diagram showing the experimental set-up for EBSD observations [104]. 64
Figure 4.1 (a) A schematic of the experimental compression procedures showing pre-compression at RT and CT, and the subsequent hot compression. (b) The true stress-strain compression curves for the direct-HD sample, RT-HD and CT-HD Mg alloy AZ31 samples deformed at 300 ℃, 0.01 s^{-1}, respectively. 69
Figure 4.2 The true stress-strain tension curves for the initial sample, and direct-HD, RT-HD and CT-HD samples, respectively. 70
Figure 4.3 EBSD IPF maps of (a) initial sample, and (b-d) the hot-deformed samples at 300 ℃ to a final strain of 1.08 (b) directly (direct-HD), (c) with RT-pre-deformation (RT-HD), and (d) CT-pre-deformation (CT-HD)..... 71
Figure 4.4 Average grain size in the initial, direct-HD, RT-HD, and CT-HD samples. 72
Figure 4.5 {0001} pole figures of (a) initial sample, (b) direct-HD sample, (c) RT-HD sample, and (d) CT-HD sample. The unit of the colour bar is in multiples of a uniform distribution (mud). 73
Figure 4.6 (a) IPF map and (b) grain size distribution in the CT-HD sample. 74
Figure 4.7 IPF maps of (a) the initial Mg alloy AZ31 sample and (b) the CT-deformed sample with a strain of 0.08, and the corresponding KAM maps of (c) the initial Mg alloy AZ31 sample and (d) the CT-deformed sample, and (e) the IPF map, KAM map and orientation evolution in grain A, respectively. 75
Figure 4.8 (a) IPF map, (b) band contrast map with twin boundaries, and (c) KAM map in the CT-HD sample with a final strain of 0.33, respectively. (d) IPF map, (e) {0001} pole figure, and (f) KAM map in the Zone B of this sample, respectively. 77

Figure 4.9 (a) IPF map, (b) band contrast map with twin boundaries, and (c) KAM map in the direct-HD sample with the final strain of 0.33, respectively. (d-f) IPF maps and corresponding (g-i) KAM maps in Zone C, Zone D and Zone E of this sample, respectively. 79
Figure 4.10 (a) IPF map, (c) KAM map, and the corresponding (b) enlarged IPF map and (d) KAM map in the RT-HD sample with the final strain of 0.33, respectively. 80
Figure 5.1 A schematic of the experimental compression procedure at room and cryogenic temperatures. 88
Figure 5.2 Total twinned area fraction and area fraction of $(10\bar{1}2)$-$(01\bar{1}2)$ interacting twins with a step size of 3 μm and 8 μm, respectively. Similar results are obtained for both step sizes. .90
Figure 5.3 (a) The true stress-strain compression curves of Mg alloy AZ31 at various temperatures, and (b) the calculated strain hardening rate variation as a function of true strain based on (a). 91
Figure 5.4 EBSD IPF maps of (a, b) two T4-treated Mg alloy AZ31 samples, and deformed samples after compression tests with a strain of 0.08 at (c) room temperature and (d) cryogenic temperature, respectively. Maps (a) and (c) and maps (b) and (d) are recorded in the same region of interest, before and after deformation. Observation along TD is applied to the IPF triangle. Label A-E highlight individual grains (see text for details). 93
Figure 5.5 (a) Twinned area fraction, area fraction and fraction of $(10\bar{1}2)$-$(01\bar{1}2)$ interacting twins in deformed samples after compression tests with a strain of 0.08 from room temperature (RT) to cryogenic temperature (CT), and (b) the corresponding {0001} and $\{10\bar{1}0\}$ pole figures, the unit of the colour bar is in multiples of a uniform distribution (mud). 95
Figure 5.6 Typical grain evolution of Mg alloy AZ31 in compression tests to a strain of 0.08 at room temperature. (a, b) EBSD IPF maps, (e, f) corresponding {0001} pole figures of initial and deformed grain A, respectively. (c, d) EBSD IPF maps, (g, h) corresponding {0001} pole

figures of initial and deformed grain B, respectively. The IPF key shows the colour scheme used in this figure. Observation along TD is applied to the IPF triangle.....96
Figure 5.7 Typical grains evolution of Mg alloy AZ31 in compression tests to a strain of 0.08 at cryogenic temperature. (a, b) EBSD IPF maps, (e, f) corresponding {0001} pole figures of initial and deformed grain C, respectively. (c, d) EBSD IPF maps, (g, h) corresponding {0001} pole figures of initial and deformed grain D, respectively. The IPF key shows the colour scheme used in this figure. Observation along TD is applied to the IPF triangle.....97
Figure 5.8 EBSD IPF maps of (a) initial and (b) RT-deformed grain E in compression tests at a strain of 0.08, and corresponding (c) KAM map in RT-deformed grain E, respectively. EBSD IPF maps of (d) initial and (e) CT-deformed grain C in compression tests at a strain of 0.08, and corresponding (f) KAM map and (g) enlarged map in CT-deformed grain C, respectively. 99
Figure 5.9 (a) The histograms of KAM distribution of two initial Mg alloy AZ31 samples and samples compressed to a strain of 0.08 at room temperature (RT, 20 ℃) and cryogenic temperature (CT, -196 ℃), (b) increase in average KAM value of samples compressed to a strain of 0.08 at room and cryogenic temperatures.....100
Figure 5.10 Schematic of twins and dislocation evolution in Mg alloys (a, c) at the initial state, and after deformation (b) at room temperature and (d) cryogenic temperatures with corresponding twinning behaviours, respectively.....102
Figure 6.1 Schematic diagram of the experimental rolling processes at room and cryogenic temperature. 109
Figure 6.2 Optical images and the corresponding enlarged images of the (a-b) RT-rolled and (c-d) CT-rolled Mg alloy AZ31 samples. The total TRs of the samples are (a, c) 3% and (b, d) 13%. 110

Figure 6.3 EBSD analysis of the (a-d) RT-rolled and (e-h) CT-rolled Mg alloy AZ31 samples with a total TR of 3%. (a) and (e) EBSD IPF maps, (b) and (f) band contrast maps with twin boundaries, (c) and (g) enlarged optical images, (d) and (h) misorientation distribution maps. Note that the characteristic misorientation axes and angles of the twins have been labelled using boxes and circles in (d) and (h) with the corresponding colours. 112
Figure 6.4 EBSD analysis of the (a-d) RT-rolled and (e-h) CT-rolled Mg alloy AZ31 samples with a total TR of 13%. (a) and (e) EBSD IPF maps, (b) and (f) band contrast maps with twin boundaries, (c) and (g) enlarged optical images, (d) and (h) misorientation distribution maps. The characteristic misorientation axes and angles of the twins have been labelled using boxes and circles in (d) and (h) with corresponding colours. 114
Figure 6.5 KAM maps of the RT-rolled samples with a total TR of (a) 3% and (b) 13%, and KAM maps of the CT-rolled samples with a total TR of (c) 3% and (d) 13%. 115
Figure 6.6 Microstructures in (a-d) Zone A and (e-h) Zone B of the 13% RT-rolled sample. Note that the locations of Zone A and Zone B are annotated in Figure 6.4 (a). (a, e) EBSD IPF maps, (b, f) band contrast maps with twin boundaries, (c, g) KAM maps and (d, h) {0001} pole figures. 116
Figure 6.7 Microstructures in (a-d) Zone C and (e-h) Zone D of the 13% CT-rolled sample. Note that the locations of Zone C and Zone D are annotated in Figure 6.4 (e). (a, e) EBSD IPF maps, (b, f) KAM maps, (c, g) {0001} pole figures, (d, h) misorientation distribution maps. 118
Figure 6.8 Detailed microstructure analysis of (a-d) grain E and (e-h) grain F in the 9% CT-rolled sample. (a, e) EBSD IPF maps, (b, f) KAM maps, (c, g) {0001} pole figures and (d, h) misorientation distribution maps.....121
Figure 6.9 Schematic illustration of the microstructure evolution during (a-c) the RT-rolling and (d-f) CT-rolling process. Insets plot the formation process of twin-twin interactions and

twinning sequence. Note that deformation bands are located inside grains while shear bands cross grain boundaries.....123
Figure 7.1 Schematic processing diagram of the rolling tests at room and cryogenic temperatures, and the subsequent heat treatment processes. 129
Figure 7.2 (a, c) EBSD inverse pole figure (IPF) maps, and the corresponding (b, d) band contrast (BC) maps superimposed by various twin boundaries of the room-temperature (RT)-rolled and cryogenic-temperature (CT)-rolled samples, respectively.....132
Figure 7.3 EBSD IPF maps and {0001} pole figures of recrystallized grains in the RT-rolled and CT-rolled samples during annealing at 300 ℃ for (a, d) 0, (b, e) 10 min, (c, f) 70 min, respectively. The unit of the colour bar is mud. 134
Figure 7.4 IPF maps and their corresponding {0001} pole figures of the recrystallized grains in the typical zones of the RT-rolled and CT-rolled samples during the annealing process at 300 ℃ for (a, d, i, l) 0, (b, e, j, m) 10, (c, f, k, n) 70 min, respectively. The {0001} pole figures of all recrystallized grains in Figure 7.3 of the RT-rolled and CT-rolled samples during the annealing process at 300 ℃ for (g, o) 10 and (h, p) 70 min, respectively. The unit of the colour bar is mud.....137
Figure 7.5 Typical zones in Figure 7.2 for the RT-rolled and CT-rolled samples, respectively: (a) Zone A, (b) Zone B in the RT-rolled sample, and (c) Zone C, (d) Zone D in the CT-rolled sample, where the first row presents the IPF maps in these zones; the second row shows their corresponding {0001} pole figures, and the hexagonal prisms are superimposed in these pole figures to present their orientations; the third row displays their misorientation distribution maps. 139
Figure 7.6 (a, b) IPF maps of the deformed and annealed grain A at 300 ℃ for 70 min, and (e, f) their corresponding KAM maps, respectively; (c, d) IPF maps of the deformed and annealed grain B at 300 ℃ for 70 min, and (g, h) their corresponding KAM maps, respectively. 140

Figure 7.7 (a, b) IPF maps of the deformed and annealed grain C at 300 ℃ for 70 min, and (e, f) their corresponding KAM maps, respectively; (c, d) IPF maps of the deformed and annealed grain D at 300 ℃ for 70 min, and (g, h) their corresponding KAM maps, respectively. 142
Figure 7.8 (a, b) IPF maps of deformed and annealed Zone E at 300 ℃ for 70 min, and (e, f) their corresponding KAM maps, respectively; (c, d) IPF maps of deformed and annealed Zone F at 300 ℃ for 70 min, and (g, h) their corresponding KAM maps, respectively. 143
Figure 7.9 (a) Grain size evolution of the RT-rolled and CT-rolled samples during the annealing process at 300 ℃, (b) grain size distribution in the RT-rolled and CT-rolled samples after annealing at 300 ℃ for 110 min. 144
Figure 7.10 Schematic of mechanisms in the RT-rolling and CT-rolling with subsequent annealing process: (a) the microstructure of initial Mg alloy AZ31; (b) the microstructure of Mg alloy AZ31 after the RT-rolling and CT-rolling; (c) the few static recrystallized (SRXed) grains nucleate at the initial stage of annealing process; (d) the fast generation of SRXed grains; (e) the stabilized SRXed grain generations in the recrystallization. 146
Figure A.1 Grain size distribution in the (a) direct-HD, (b) RT-HD, and (c) CT-HD samples. 166
Figure A.2 {0001} pole figures in fine-grained zones of (a) direct-HD sample, (b) RT-HD sample, and (c) CT-HD sample. The unit of the colour bar is in multiples of a uniform distribution (mud). 166
Figure B.1 Optical images and the corresponding enlarged images of the RT-rolled sample with a total TR of (a-b) 3% and (c-d) 13%. 167
Figure B.2 EBSD analysis of the (a-c) RT-rolled and (d-f) CT-rolled AZ31 samples with a total TR of 9%. (a) and (d) EBSD IPF maps. (b) and (e) band contrast maps with twin boundaries. (c) and (f) optical images with the corresponding enlarged images. 167

Figure B.3 KAM maps of (a) RT-rolled and (c) CT-rolled samples with a TR of 9%, and (b, d) their corresponding misorientation distributions, respectively. 168
Figure B.4 Detailed microstructure analysis of Zone G in the 13% CT-rolled sample. (a) EBSD IPF map, (b) {0001} pole figure and (c) misorientation distribution map. 169
Figure C.1 EBSD IPF maps and {0001} pole figures of the recrystallized grains in the RT-rolled and CT-rolled samples during annealing at 300 ℃ for (a, b) 5 min, (c, d) 110 min, respectively. The unit of the colour bar is mud. 170

List of Tables

Table 2.1 Misorientations generated between different $\{10\bar{1}2\}$ twin variants [41] 42

Table 3.1 Chemical compositions of Mg alloy AZ31 [99] 59

List of Acronyms

BC	Band contrast
CT	Cryogenic temperature
CD	Compression direction
CCD	Charged-coupled device
CPFE	Crystal plasticity finite-element
CRSS	Critical resolved shear stress
CTW	Compression twin
DFT	Density functional theory
DRX	Dynamic recrystallization
DTW	Double twin
EBSD	Electron Backscattered Diffraction
EL	Elongation to fracture
FS	Fracture strength
GBs	Grain boundaries
GND	Geometrically necessary dislocation
HAGBs	High angle grain boundaries
HCP	Hexagonal close-packed
HD	Hot deformation
IPF	Inverse pole figure
KAM	Kernel Average Misorientation
LNT	Liquid nitrogen temperature
LAGBs	Low-angle grain boundaries
Mg	Magnesium

ND	Normal direction
RD	Rolling Direction
RT	Room temperature
SSD	Statistically stored dislocation
SEM	Scanning electron microscope
SRX	Static recrystallization
TR	Thickness reduction
TTW	Tension twin
Ti	Titanium
TD	Transverse direction
YS	Yield strength

1 Introduction

1.1 Background

It is essential and challenging to reduce energy consumption and mitigate air pollution. The European Commission set the mandatory emission reduction for new cars from 122.4 grams of CO_2 per kilometre (g CO_2/km) in 2019 to 95 g CO_2/km in 2024 [1]. The UK started to take action to reduce the fuel consumption and the CO_2 emissions of passenger cars in 2001 [2]. Low-weight vehicles are a good way to achieve this aim. A 10% reduction in vehicle weight can offer up to a 7% improvement in fuel economy [3]. The weight reduction is also able to improve vehicle acceleration and braking performance [3].

Magnesium (Mg) alloys are the lightest structural metals. Their density is about 2/3 that of aluminium and 1/4 that of steel [4, 5]. Therefore, Mg alloys are promising alternatives for aluminium and steel to reduce the weight of the structural material used in automotive industries. However, the application of Mg alloys is limited, and it makes up less than 0.2% of the weight of an average vehicle, mainly due to poor mechanical properties [6-8]. One of the key issues is the poor ductility and strength of Mg alloys for applications at room temperature [9], and this is mainly attributed to their strong basal texture and coarse grains formed in the mechanical and thermo-mechanical manufacturing processes [10, 11]. Therefore, it is necessary to create a novel and effective method to refine the grains and weaken the texture in order to enhance the mechanical properties of Mg alloys.

The formation of a strong texture and coarse grains in Mg alloys is associated with recrystallization in the thermo-mechanical process [12-14]. However, it was found that the recrystallization near deformation twins, namely twin recrystallization, can weaken the texture and refine the grains. For example, twin recrystallization in the hot deformation in a Mg alloy ZK60 resulted in a weakened basal texture [15], and the recrystallization around twins can also

weaken the deformed texture and produce new orientations during the annealing process of Mg alloys [16, 17]. In addition, the recrystallization near twins was applied to refine the grains in Mg alloys significantly [15]. Therefore, it is expected that the recrystallization near twins could be an effective way to weaken the texture and refine the grains in the conventional Mg alloy AZ31.

The cryogenic deformation would be a novel way to promote twin activities for subsequent recrystallization, because twinning rather than dislocation slip generally occurs in the deformation at a lower temperature to accommodate the imposed plastic strain [18, 19]. However, the deformation mechanisms of Mg alloys at cryogenic temperatures (below room temperature) are still unclear; the microstructure behaviours at cryogenic temperatures, including twinning, texture and grain size behaviour, lack a systematic and detailed study. As the formation of new grains and texture is strongly associated with recrystallization, the investigation of the recrystallization after cryogenic deformation is also important, and it could provide a novel way to refine the grains and weaken the texture. However, the recrystallization mechanisms and microstructure evolutions in the cryogenic-deformed Mg alloys in the thermo-mechanical process are rarely reported. Therefore, it is worth investigating the cryogenic deformation behaviour and subsequent recrystallization mechanisms in Mg alloys. The corresponding room-temperature deformation is also conducted to investigate dislocations and deformation bands and their effects on recrystallization.

1.2 Aims and objectives of the research

This research aims to study the deformation behaviour of Mg alloy AZ31 at cryogenic temperature (CT) and room temperature (RT), and the corresponding recrystallization mechanisms during the thermo-mechanical process. Based on the investigation of these

mechanisms, a novel and effective method is created to refine the grains and weaken the texture. To realise this aim, four objectives were set as follows.

(1) Investigate the feasibility of a novel method combining the cryogenic and subsequent hot deformation process to achieve the weak texture and fine grains, and study the recrystallization behaviour of the cryogenic- and room-temperature-deformed samples during the hot deformation process.
(2) Investigate the microstructural and mechanical behaviours involved in the deformation process at cryogenic and room temperature, and study the relationship between twinning and dislocations, and their induced texture and microstructure behaviours.
(3) Gain an in-depth understanding of the evolution of twin-twin interactions, twinning sequence and deformation bands during the rolling process at cryogenic and room temperature.
(4) Study the microstructure evolution in the recrystallization around the twin-twin interactions and deformation bands during the annealing process of the cryogenic- and room-temperature-rolled samples, respectively, and explain mechanisms about the formation of different textures and microstructures.

1.3 Thesis structure

This thesis consists of eight chapters. Chapter 1 introduces the industrial background of Mg alloys, the aim and objectives, and the thesis structure of this research.

Chapter 2 contains the literature review of this research. The current progress of the deformation behaviour in Mg alloys, including typical deformation modes, microstructures and temperature effects, is summarized. Then, the recrystallization mechanisms of Mg alloys in the thermo-mechanical process are reviewed. The identified unsolved questions are summarized to be addressed in the following chapters.

Chapter 3 describes the material (Mg alloy AZ31), the microstructure characterization methods and mechanical testing including compression, tensile and rolling tests performed in this research.

The investigation in Chapter 4-7 is conducted to achieve the four objectives of this thesis. To clarify the logical link of Chapter 4-7, a corresponding flowchart is shown in Figure 1.1.

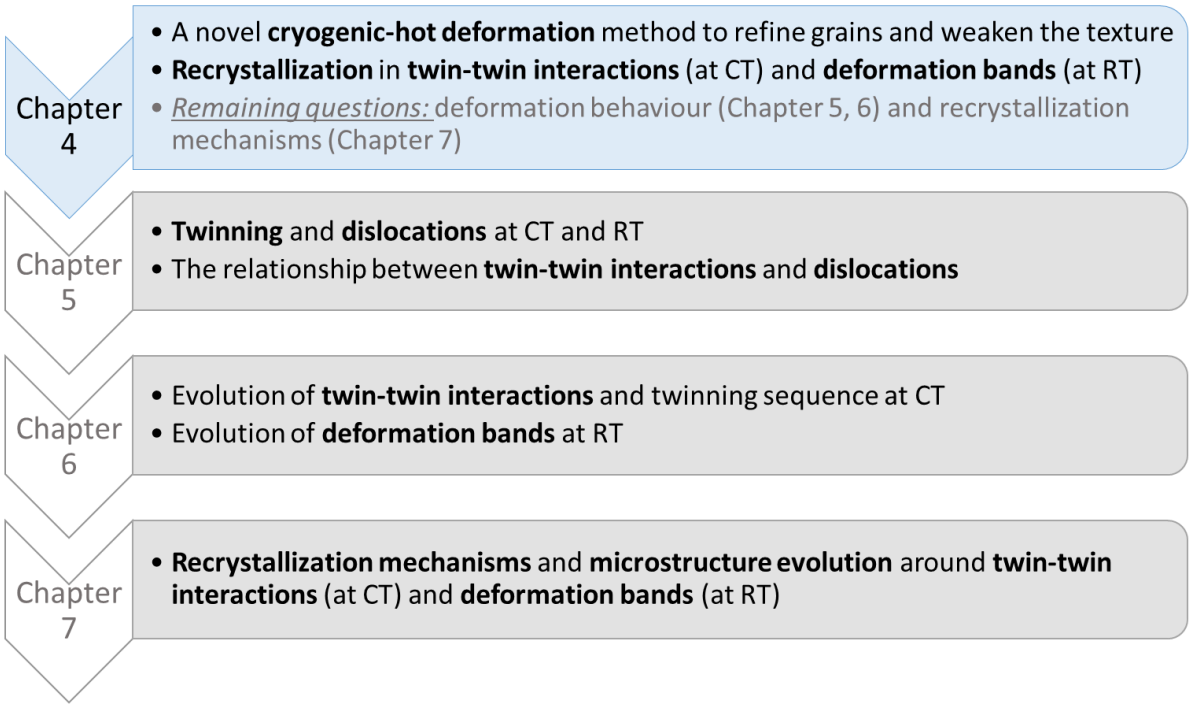

Figure 1.1 Flowchart showing the logical link of Chapter 4-7.

Chapter 4 investigates the proposed novel cryogenic-hot deformation method to refine the grains and weaken the texture in Mg alloy AZ31. The EBSD orientation mapping is conducted to analyse the microstructure in the CT-hot-deformed, RT-hot-deformed and direct-hot-deformed samples. The tensile ductility and strength of these samples are measured to link with their corresponding microstructures. The different microstructures in these samples are attributed to the various recrystallization behaviours in twin-twin interactions (CT-hot-deformed samples) and deformation bands (RT-hot-deformed and direct-hot-deformed samples). However, more detailed deformation mechanisms at CT and RT and corresponding

recrystallization mechanisms are required, leading to the systematic investigation in Chapter 5, 6 and 7.

Chapter 5 investigates the deformation behaviour of Mg alloy AZ31 at low temperatures from -196 ℃ (CT) to 20 ℃ (RT). The competition behaviour and relationship between twinning and dislocation slips at the CT and RT are established using a *quasi-in-situ* EBSD method.

Chapter 6 studies the twinning and deformation bands in the rolling process at CT and RT. The evolution of tension twins, twin-twin interactions and twinning sequence during the CT-rolling is systematically investigated. The formation and evolution of deformation bands during the RT-rolling are also studied.

Chapter 7 investigates the recrystallization mechanisms in twin-twin interactions and deformation bands in the annealed CT-rolled and RT-rolled samples, respectively. The *quasi-in-situ* EBSD method is used to observe the texture and microstructure evolution.

Chapter 8 summarises the new understandings and findings of cryogenic deformation and recrystallization according to the above chapters. The suggestions for future work are also given, based on the achieved results and conclusions.

The main work in Chapter 5, Chapter 6, and Chapter 7 has been published in Materials Science and Engineering: A [20], Materials & Design [21] and Materials & Design [22], respectively. The main work in Chapter 4 was submitted to Acta Materialia [23].

2 Literature review

This chapter focuses on reviewing the previous work about the deformation mechanisms and recrystallization in Mg alloys. Section 2.1 introduces the main deformation modes, including dislocation slip and twinning. Section 2.2 clarifies the effects of grain size and texture on the ductility and strength. Section 2.3 introduces the typical microstructures in the deformed Mg alloys. Section 2.4 presents the effects of temperature on dislocation slip and twinning, and highlights the cryogenic deformation behaviour. Finally, the research on recrystallization mechanisms, particularly twin recrystallization, is reviewed in Section 2.5.

2.1 Deformation modes

2.1.1 Dislocation slip

Magnesium has a hexagonal close-packed (HCP) structure, as shown in Figure 2.1. The predominant slip modes are basal slip (3 (0001)<11 $\bar{2}$ 0> systems), prismatic slip (3 {10$\bar{1}$0}<11$\bar{2}$0> systems) and second-order pyramidal slip (6 {11$\bar{2}$2}<11$\bar{2}$3> systems). The most commonly observed slip is the basal slip, because the basal slip has the lowest critical resolved shear stress (CRSS) value at room temperature. There are three basal slip systems with <a> type Burgers vector gliding on (0001) basal planes, and these three <a> type Burgers vectors are co-planar within basal planes, so it only has two independent easy-slip systems of this type. This fails to meet the so-called Von Mises deformation criterion [24] for uniform plastic deformation, i.e. five independent easy-slip systems are required for the uniform arbitrary strain of a polycrystalline material [7]. As twinning and non-basal slips can provide additional deformation modes to fulfil the criterion, twinning and non-basal slips are important for achieving the uniform plastic deformation in Mg alloys.

However, the difference in the critical resolved shear stress (CRSS) between the basal slip and non-basal slip systems is significant, e.g. the ratio of CRSS between pyramidal <c+a> slip and

basal slip in pure magnesium can be 12-40 [25-27]. Therefore, the active slip system at room temperature is limited to basal slip. Non-basal slips are difficult to be activated, resulting in the poor ductility of Mg and its alloys [9, 26]. As suggested from the atomic density functional theory (DFT) simulation [10, 28], the poor ductility of pure Mg at room temperature was attributed to the reduced mobility of pyramidal slips. If the non-basal slips can be promoted as suggested by recent studies, the ductility of the Mg or Mg alloys can be significantly improved [9, 28, 29].

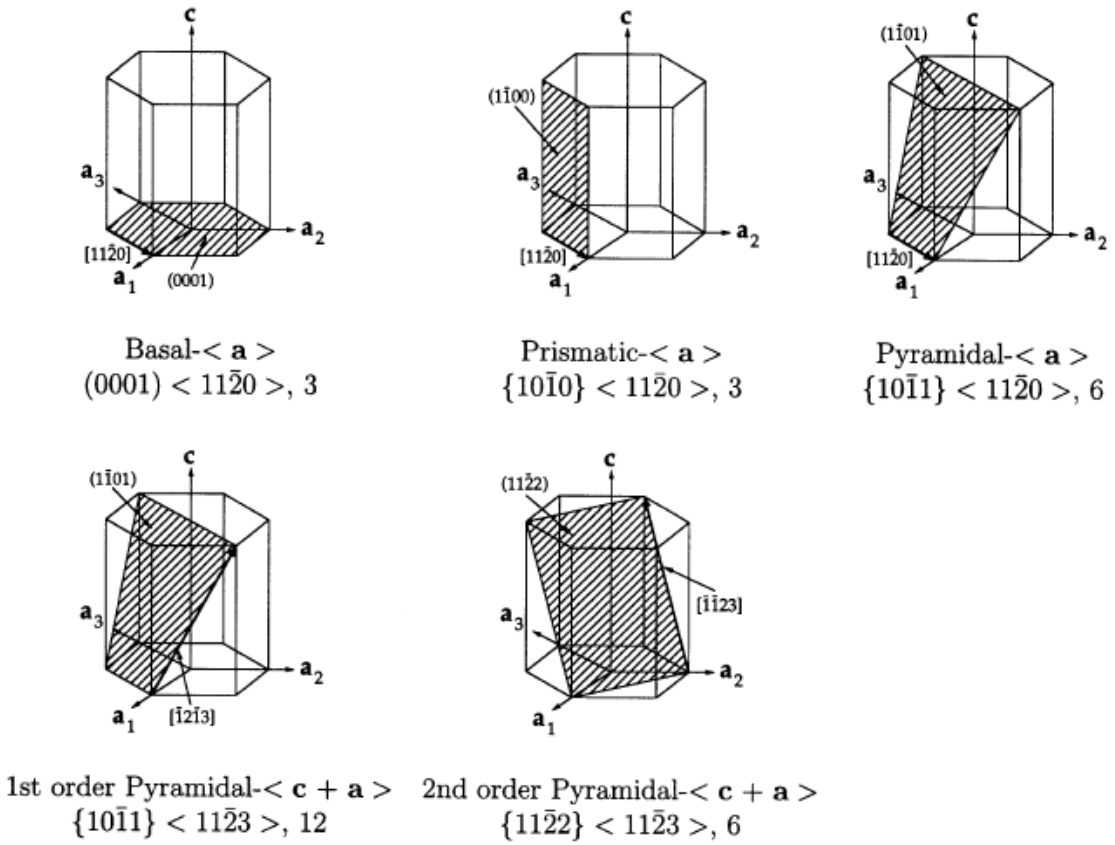

Figure 2.1 Basal, prismatic, pyramidal <a> slip systems, and first- and second-order pyramidal <c+a> slip systems in HCP materials. Shaded planes represent the slip planes, while arrows represent the Burgers vector directions [30].

2.1.2 Twinning

Twinning is often activated in Mg alloys as an additional mode to the dislocation slip to accommodate the plastic strain [27, 31]. In Figure 2.2, the main twin modes are {10$\bar{1}$2}<10$\bar{1}$1>

tension twins (TTWs) (6 systems) and $\{10\bar{1}1\}<10\bar{1}2>$ compression twins (CTWs) (6 systems) [27, 31]. The $\{10\bar{1}2\}$ TTWs can be generated by tension stress along the *c*-axis, while $\{10\bar{1}1\}$ CTWs can be activated by compression stress along the *c*-axis. In Figure 2.2, TTWs and CTWs reorientate the *c*-axis of the twin crystal by ~86° and ~56° about the $<11\bar{2}0>$ axis, respectively. Besides, CTWs are generally fine and could reorient the crystals for continuing deforming by the soft modes of the basal slips or secondary TTWs [32]. The secondary TTWs tend to nucleate inside CTWs and then overtake the fine CTW lamella to form $\{10\bar{1}1\}$-$\{10\bar{1}2\}$ double twins (DTWs) [26, 31].

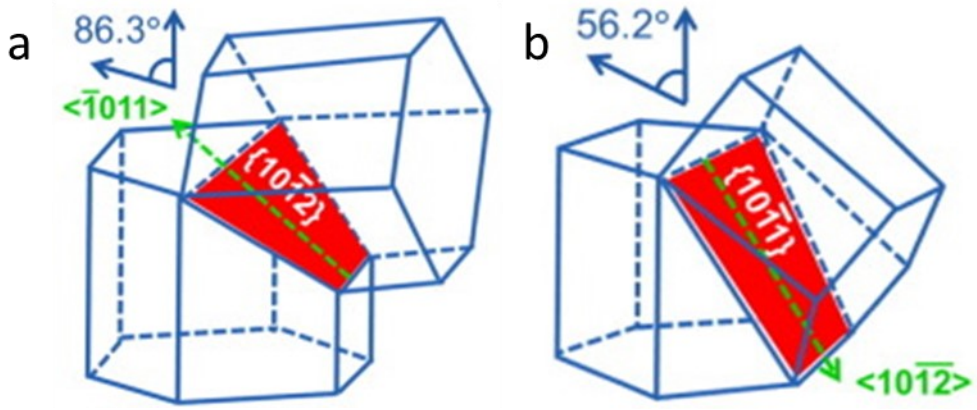

Figure 2.2 Schematic of (a) $\{10\bar{1}2\}$ tension twin and (b) $\{10\bar{1}1\}$ compression twin modes in Mg. Shaded planes represent the twin planes, while arrows represent the twinning shear directions [33].

The CRSS value of $\{10\bar{1}2\}$ TTWs is commonly lower than that of non-basal slips, so it is easy to activate TTWs instead of non-basal slips at a low temperature [34, 35]. TTWs are generally extended along the *c*-axis in magnesium and can increase the uniform elongation in tensile tests [36]. TTWs can be observed in a local crystal having the *c*-axis oriented perpendicular to the compression axis or the tension axis parallel to the *c*-axis [37, 38]. TTWs can reach profuse levels and even overtake the whole grain [26], resulting in the formation of the typical strong basal texture with *c*-axes of most grains parallel to the compression direction [39]. For example, in a compression test with the compression direction perpendicular to the *c*-axis of most grains (denoted "*c*-axis extension"), approximately 80% of the parent grains were twinned in

compression with the 8% strain, through twinning the deformed areas were reoriented to plastically hard to be deformed orientations [40]. As a result, in Figure 2.3, a rapid hardening in a sigmoidal (S-shaped) compressive flow curve was observed after a low-stress plateau in the compression with the *c*-axis extension [40, 41]. Besides, the twin boundaries could also act as barriers to the motion of dislocations, resulting in additional hardening effects [42, 43]. However, when the compression direction was parallel to the *c*-axis of most grains (denoted "*c*-axis compression"), the stress-strain curve showed a smooth elastic-plastic transition after the linear elasticity, in which $\{10\bar{1}1\}$ CTWs could be activated [44, 45].

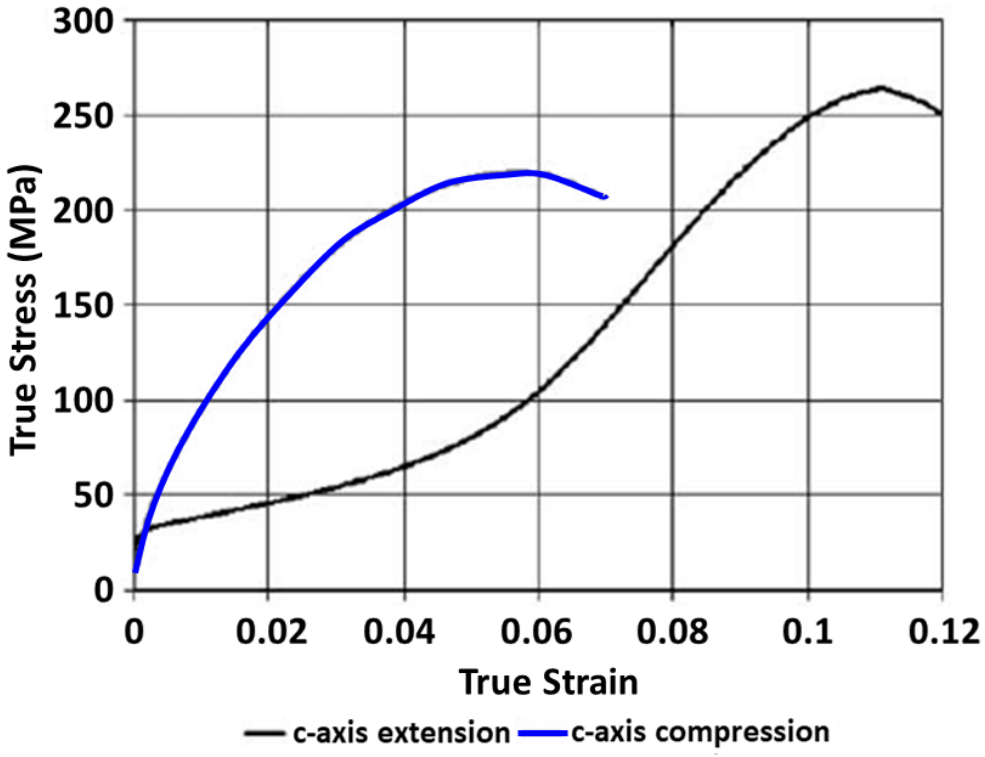

Figure 2.3 True-stress versus true-strain curves for rolled samples subjected to the plane-strain compression with c-axis extension and c-axis compression [41].

2.2 Effects of grain size and texture on mechanical properties

Grain size and texture are two key microstructures that affect the ductility and strength of Mg alloys. With the aim of refining the grains and weakening the texture, it is worth clarifying the relationship between these two microstructures with the ductility and strength.

2.2.1 Grain size effects

Fine grains generally contribute to improving the strength and ductility of Mg and Mg alloys [9, 10]. For example, the exceptionally high yield strength of ~380 MPa in Mg alloy AZ31 with ultrafine grains of 0.65 μm was achieved via extrusion at 175 ℃ [46]. The finer grain size results in the higher yield strength, according to the empirical Hall-Petch law [47, 48], namely:

$$\sigma_y = \sigma_0 + kd^{-\frac{1}{2}} \quad (1)$$

Where σ_y is the yield stress, σ_0 is the lattice friction stress when dislocations move on the slip plane, and k is a constant named the Hall-Petch slope. The physical meaning of the Hall-Petch effect is based on considering grain boundaries as barriers where dislocation pile-ups lead to increasing the yield strength of the material. In a finer grain size material, as the total grain boundary area increases, its yield strength is higher [49]. N. J. Petch [50] also found that the grain size dependence of the fracture stress obeyed the relationship in Equation (1). The fracture stress is the stress required for the crack propagation, and grain boundaries are main barriers to crack propagation. Therefore, more grain boundaries in fine-grained materials can suppress crack propagation more effectively, resulting in higher fracture stress.

As shown in Figure 2.4, the ductility of Mg alloys generally increases with decreasing grain size [10]. This could be attributed to more active non-basal slips [9, 51] and limited twins in the fine-grained sample [19, 52]. The non-basal slip systems in a fine-grained Mg alloy AZ31 were activated around grain boundaries due to the additional shear stress used to achieve compatibility between deformed grains, as the basal slip systems cannot achieve the compatibility near grain boundaries without non-basal slips [51]. Recently it was found that a submicrometer-size Mg crystal sample exhibits a higher ductility than its bulk sample, because the small crystal size would generate high stress, resulting in the activation of more non-basal <c+a> dislocations to accommodate the plasticity [9]. The twin activities were limited in the

fine-grained Mg alloys, because the twinning-dominated deformation would change to be slip-dominated when the grain size was reduced, and this transition was accompanied by a change in Hall-Petch slope [19, 52]. Twins generally nucleated in the regions with the stress concentration, such as grain boundaries [7], as the stress concentration was generated by the dislocation pile-ups near grain boundaries [19]. Therefore, in most cases, similar to slip stress, the stress to initiate twinning also obeys the Hall-Petch relationship, and it can be represented by [19]:

$$\sigma_T = \sigma_{T0} + k_T d^{-\frac{1}{2}} \quad (2)$$

The slope k_T for twinning is much larger than the slope k_S for the slip, as confirmed by the experimental results [52]. Therefore, it is more difficult to activate twinning in fine-grained samples. The limited twinning activities would be related to the high ductility in fine-grained Mg alloys, because twins are generally associated with the fractures in Mg alloys [31, 53, 54]. It was reported that $\{10\bar{1}1\}$-$\{10\bar{1}2\}$ double twins could be responsible for the fractures, because these twins could induce strain softening and generate twin sized voids locally [31]. The strain softening would be attributed to more favourably oriented for basal slips in double twins than parent grains. As a result, the twins were deformed more heavily than parent grains, and the large incompatibility at the boundary between twins and parent grains can result in fractures [53]. Besides, grain boundaries provide obstacles for the micro-cracks to propagate, more grain boundaries in fine-grained Mg alloys will make it more difficult for micro-cracks to propagate [50]. This will be beneficial to the higher ductility in fine-grained Mg alloys [55]. The micro-cracks proposed in Ref [50] could mainly refer to intragranular cracks rather than intergranular cracks, as intergranular cracks near more grain boundaries could be detrimental to ductility.

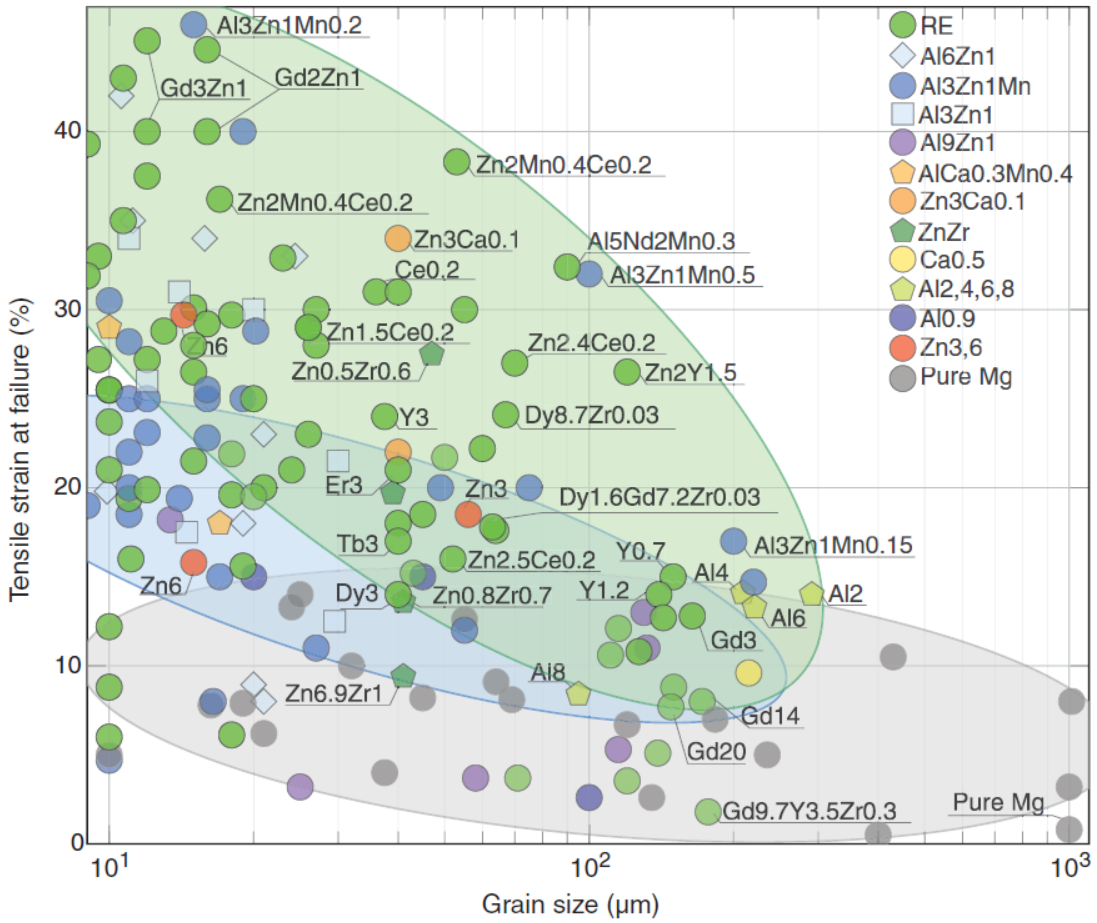

Figure 2.4 Room-temperature tensile strain failure, as a measure of ductility, versus grain size in selected polycrystalline Mg and Mg alloys [10].

2.2.2 Texture effects

Besides grain size, texture also has a significant effect on the mechanical properties of Mg alloys, because the texture affects the activation of potential slip systems [7]. It is easy to form a strong texture in Mg alloys during thermo-mechanical processes, such as the rolling process. Figure 2.5 shows the mechanism of a strong basal texture formation in Mg during the rolling process [56]. When the compression direction is perpendicular to the *c*-axis direction of a Mg crystal, it is easy for the Mg crystal to rotate on a $\{10\bar{1}2\}$ plane, resulting in the formation of the $\{10\bar{1}2\}$ tension twinning and its *c*-axis parallel to the compression direction. However, when the compression direction is parallel to the *c*-axis of the Mg crystal, the *c*-axis direction

remains virtually unchanged, as it is difficult for $\{10\bar{1}2\}$ tension twinning to occur in this orientation. Therefore, the *c*-axes of these Mg crystals are parallel to the compression direction or normal direction after the rolling process, resulting in the formation of a strong basal texture. The strong basal texture results in poor ductility when the loading direction is parallel to the normal direction, because of the difficulty activating the basal slips (the resolved loading angle on the basal plane is nearly zero) and the limited ability to accommodate the compression along the *c*-axis [57]. Although the strong texture can result in the hardening in the *c*-axis compression test (Figure 2.3), it leads to low ductility in this loading direction. Figure 2.5 shows the formation of strong basal texture which is mainly related to tension twins, while the relationship between the formation of basal texture and recrystallization is not shown, which would be related to the preferential basal grain growth of Mg alloy [13, 58].

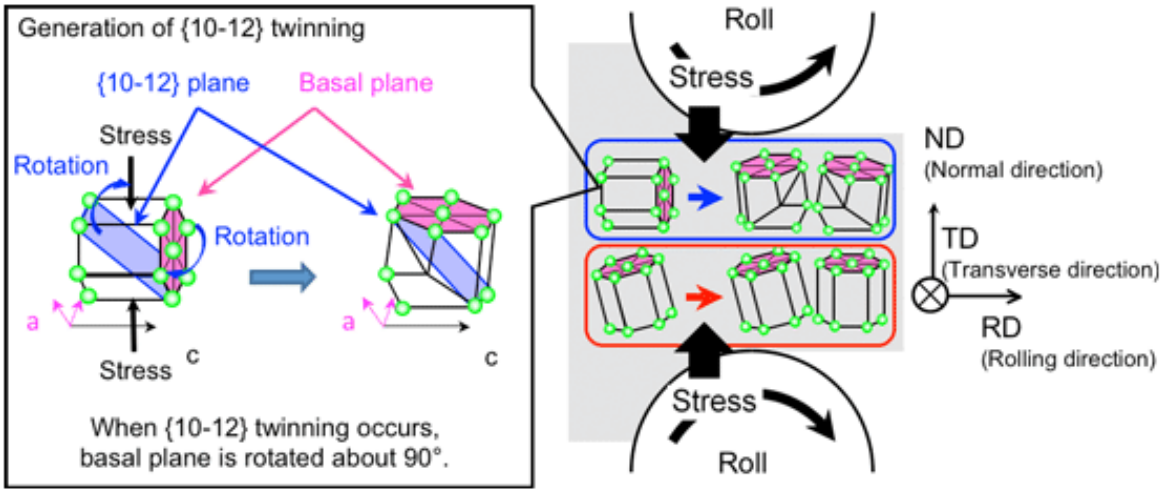

Figure 2.5 Texture formation of rolled magnesium [56].

If Mg alloys show a weak texture, many grains would have the *c*-axes tilted away from the normal direction of the samples, so the basal slip systems can be readily activated to accommodate the plastic deformation due to higher resolved shear stress on the basal planes [59]. For example, in Figure 2.6, the elongation of the rolled Mg alloy AZ31 sheets increases with decreasing texture pole intensity, indicating that the weaker texture in Mg alloys can

contribute to the higher ductility [60], while the grain size which is not considered in this work could also affect the ductility. Therefore, to improve the ductility and strength of Mg alloys, it is necessary to find a novel and effective method to weaken the texture and refine the grains.

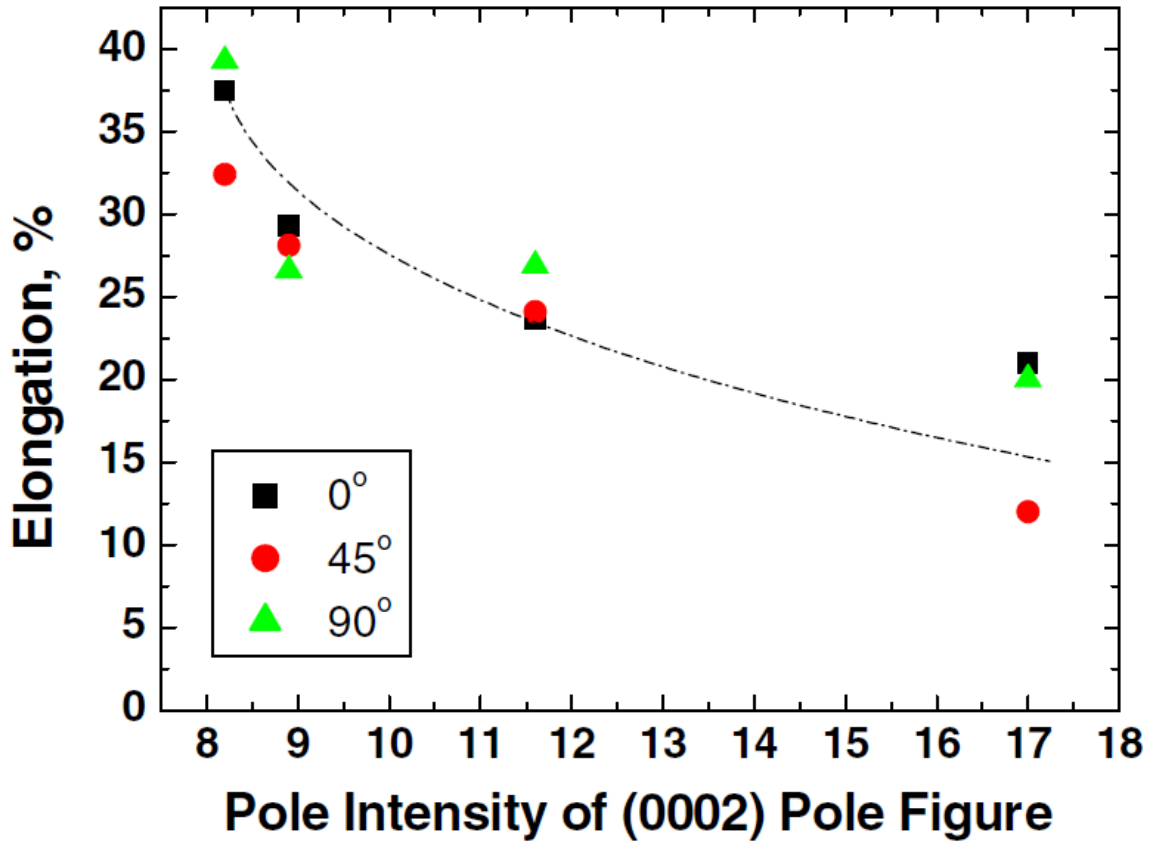

Figure 2.6 Tensile elongations of the rolled Mg alloy AZ31 sheets as a function of pole intensity in (0002) pole figures. Tensile specimens were cut along planes coinciding with the rolling direction (0°) and at angles of 45° and 90° (transverse) to the rolling direction [60].

2.3 Typical microstructures in the deformation process

The formation of fine grains and a weak texture in Mg alloys is related to the mechanical and thermo-mechanical processes. For optimizing grain size and texture, it is essential to understand the typical microstructures in these processes. This section summarizes the up-to-date research on typical microstructures, including twin-twin interactions, twinning sequence, deformation bands and shear bands.

2.3.1 Twin-twin interactions

TTW can form on any one of six $\{10\bar{1}2\}$ planes in grains of Mg, and these TTWs would interact to form twin-twin interactions, including $(10\bar{1}2)$-$(01\bar{1}2)$, $(10\bar{1}2)$-$(\bar{1}012)$ and $(10\bar{1}2)$-$(0\bar{1}12)$ [41], as shown in Table 2.1. For example, in Figure 2.7 (a), tension twin variants T1 and T4 form the twin-twin interaction in a single crystal Mg compressed along the $[10\bar{1}0]$ direction [61]. The twin variants T1 and T4 are in $(10\bar{1}2)$ and $(\bar{1}012)$ planes respectively, as shown in Figure 2.7 (b) [62]. As twins generally cannot transmit across twin boundary, twin-twin interactions can form twin-twin boundaries that contain boundary dislocations [61, 63, 64]. Twin-twin interactions can also prevent twin propagation and promote secondary twins, resulting in twinning-induced grain refinement [61, 64].

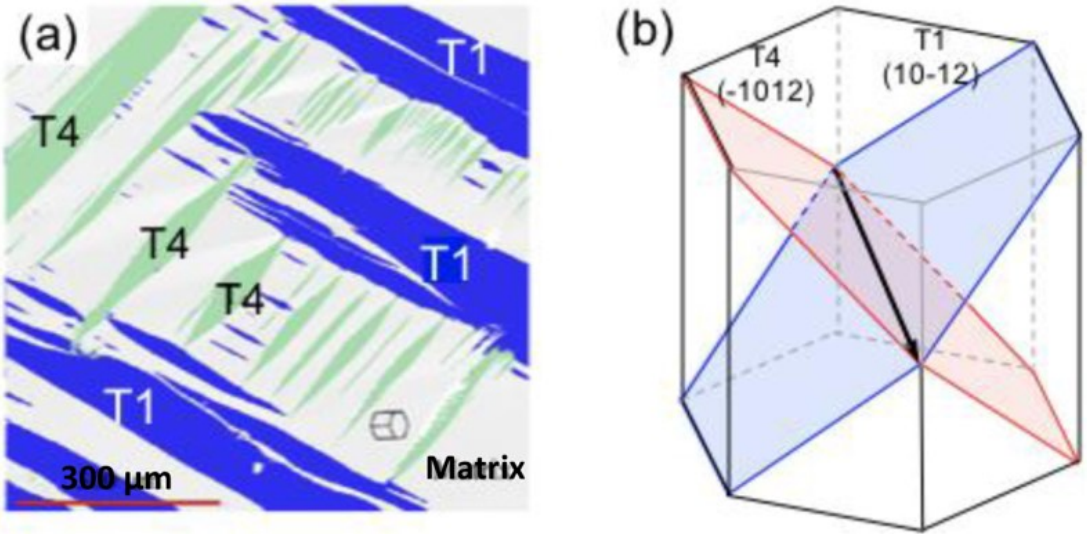

Figure 2.7 Experimentally observed twin-twin interaction in single-crystal magnesium compressed along $[10\bar{1}0]$ direction [61]. (b) Schematic representation of the twin-twin interaction considered here, formed by tension twin variants T1 $(10\bar{1}2)$ and T4 $(\bar{1}012)$. Scale bar, 300 µm [62].

The twin-twin interactions can contribute to an enhanced strain hardening rate [65, 66] due to its significant twinning-induced grain refinement [64] and high-stress fields [61, 62]. The twin-twin hardening was investigated by comparing two interacting twin variants in one grain with a single twin variant in another grain [64]. It was found that the twin nucleation rate was faster

in the two twin variants condition, while the twin propagation rate was faster in the one twin variant condition. As the stress for twin nucleation was generally higher than that for twin propagation [45], and the Hall-Petch effect was induced by the twin segmentation of two interacting twins, it was suggested that the grain with two interacting variants should show a higher hardening rate than the grain with a single variant [64]. Additionally, a 3D full-field crystal plasticity model and large-scale molecular dynamics indicated that the local stress fields were generated after the initial formation of the twin-twin interactions. The predicted stress concentration resulting from twin-twin interactions can locally increase the strength, which can enhance the global strength of the material if there are abundant twin-twin interactions. The stress field near twin-twin interactions can also contribute to the nucleation of new twins [62]. Altering the loading directions was found to increase the twin-twin interactions volume fraction [61, 63]. However, in practice, changing the loading directions in a continuous manufacturing process would considerably reduce the productivity. Another effective method to promote twin-twin interactions is needed. Also, experimental results of the effects of twin-twin interactions on strength and texture, and its relationship with dislocations are unavailable in the literature.

Table 2.1 Misorientations generated between different {10$\bar{1}$2} twin variants [41]

Type of twin	Misorientation angle/axis
(10$\bar{1}$2)- ($\bar{1}$012)	7.4° <1$\bar{2}$10>
(10$\bar{1}$2)- (01$\bar{1}$2)	60.0° <10$\bar{1}$0>
(10$\bar{1}$2)- (0$\bar{1}$12)	60.4° <8$\bar{1}\bar{7}$0>

2.3.2 Twinning sequence

The twinning sequence, forming subsequent twins in existing twins, also occurs to accommodate the imposed plastic deformation [18, 67]. Regarding the Mg, the frequent

twinning sequence is $\{10\bar{1}1\}$-$\{10\bar{1}2\}$ DTWs, i.e. secondary TTWs form in primary CTWs [26, 31]. However, the formation of sequential TTWs in TTWs is rarely reported in Mg alloys, and this could be attributed to the *c*-axis of primary TTWs almost parallel to the compression direction which is unfavourable to the secondary TTWs [68, 69]. Until now, only few research have observed the sequential TTWs in Mg alloys, which were activated by changing the loading directions and generating multiaxial stress fields [68, 70, 71]. For example, the sequential double tension twins were obtained at RT by compressing the sample in the rolling direction (RD) and subsequently in the transverse direction (TD) [68]. The double tension twins were also observed in a pure Mg single crystal during the rolling process, and this anomalous twin behaviour could be attributed to the local deformation response in the multiaxial stress fields [71]. As shown in Figure 2.8, the sequential TTWs, i.e. double tension twin structures, were observed in a Mg single crystal under compression-tension cyclic loading along the [0001] direction. There are two double tension twin structures in Figure 2.8. In Figure 2.8 (a) and (b), the secondary twins T_{54} and T_{31} form in the primary twins T_5 and T_3, respectively, while these secondary twins do not connect other twins T_4 and T_1 that interact with the primary twins T_5 and T_3. Another double tension twin structure is shown in Figure 2.8 (c) and (d). The secondary tension twins T_{12} and T_{62} in the primary twins T_1 and T_6 connect to another twin T_2 that interacts with the primary twins T_1 and T_6. The formation of these double tension twins could be attributed to the change of the applied loading or the local stresses generated from other features such as interacting twins, as secondary tension twins hardly occur in primary tension twins without changing the stress state in the primary twins [61].

Besides, the double tension twinning was observed in a Mg-8Al-0.5Zn alloy in compression at the cryogenic temperature, and this could be due to the difficulty activating non-basal slips to accommodate the deformation [72]. The high-order twinning sequence was observed in the cryogenic-rolled titanium (HCP metal), namely, tension twin → compression twin → tension

twin, and the active twinning behaviour could be attributed to the suppression of dislocation slips [18] and significant local stress concentrations in the cryogenic rolling [73]. Therefore, cryogenic rolling would be a potential way to promote the twinning sequence and twin-twin interactions. The relationships between the twinning sequence and twin-twin interactions, and their concurrent interactions with dislocations, can also be studied with cryogenic rolling comprehensively.

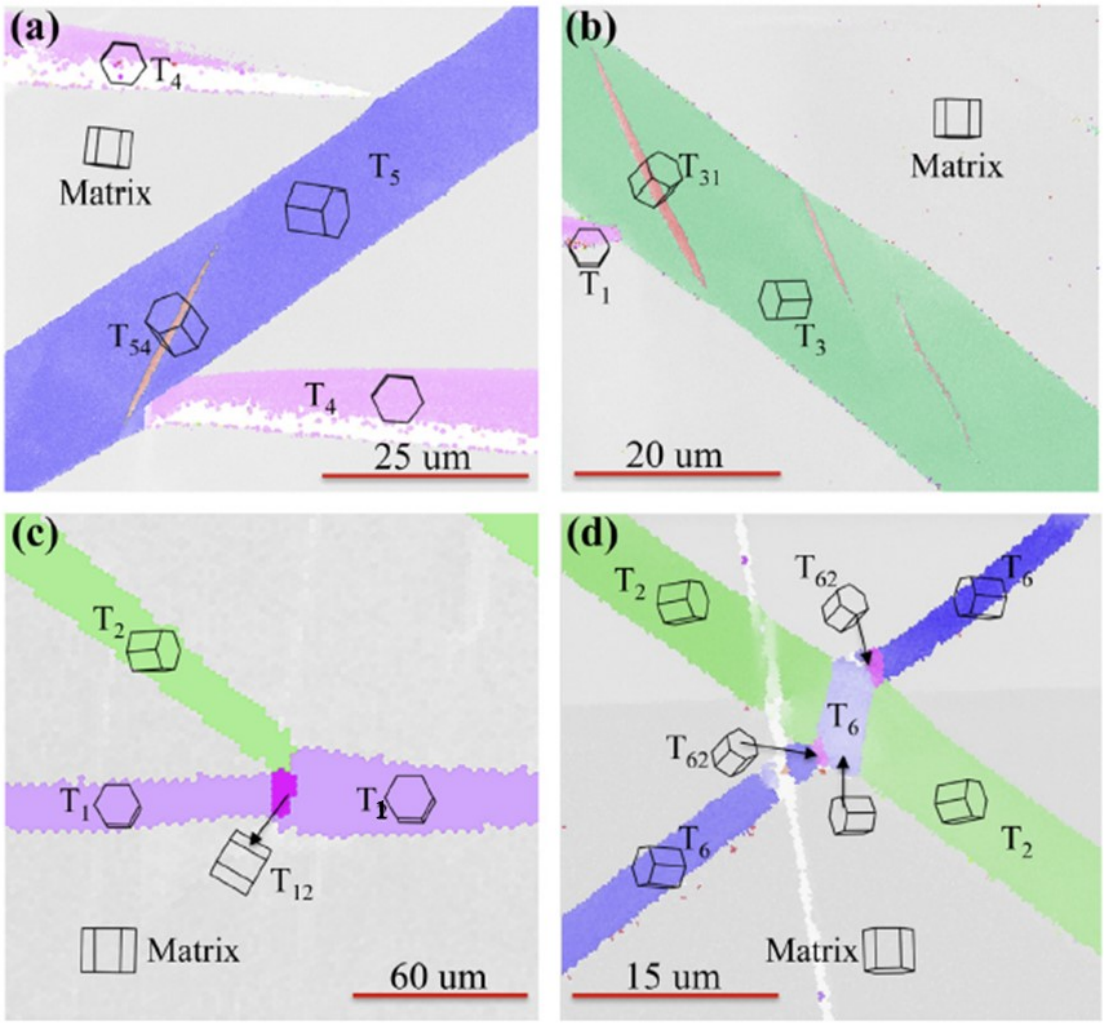

Figure 2.8 Double tension twin structures in the magnesium specimen loaded along the [0001] direction. The secondary twin does not connect to an incoming twin: (a) a secondary twin T_{54} inside a primary twin T_5 and (b) three secondary twins T_{31} inside a primary twin T_3. The secondary twin connects to twin-twin boundaries: (c) a secondary twin T_{12} inside a primary twin T_1 and (d) two secondary twins T_{62} inside a primary twin T_6 [61].

2.3.3 Deformation bands

Deformation bands are generally found in individual grains, particularly in coarse-grained materials, as shown in Figure 2.9 (c). Deformation bands could originate from dislocations [74] or twins [75]. The resulting deformation bands deform on different slip systems and may develop different orientations from the orientations present elsewhere in this grain. This could result from the inhomogeneous stress transmitted by neighbouring grains or the intrinsic instability of grains during plastic deformation [74]. In Figure 2.9 (c), the orientation of region C is different from that in region A, and the deformation bands occur with approximately parallel sides and involve a double orientation change of A to C and then C to A. This special type of deformation bands is named a kink band [74, 76]. This kind of deformation bands was observed in the Al-1%Mg alloy and mainly associated with dislocation slips, while the formation of deformation bands in Mg alloys was not investigated in this Ref [74].

However, the formation of deformation bands in Mg alloys was mainly related to twins [75]. It was found that abundant twins, especially compression and double twins, were concentrated along deformation bands in the MgNd0.04 alloy during the rolling process [75]. The compression and double twins were also observed in the narrow deformation bands in AZ31B Mg alloy sheet after tensile tests [53]. The deformation bands can be identified by their black colour in optical microscopy after etching, as these bands contained extensive strain localization [77]. However, the formation of deformation bands and its relationship with deformation twins and dislocations in Mg alloys are still unclear. It requires an in-depth investigation to reveal how deformation bands in Mg alloys evolve from twins and dislocations.

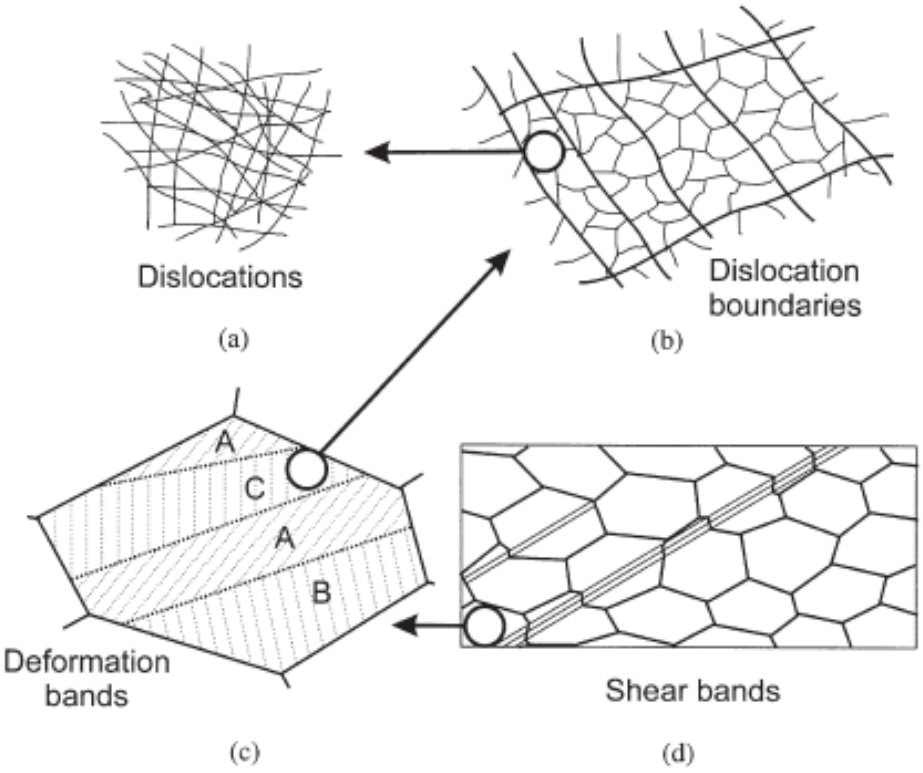

Figure 2.9 The various features are shown at an increasing scale: (a) dislocations, (b) dislocation boundaries, (c) deformation bands within a grain, (d) specimen- and grain-scale shear bands [74].

2.3.4 Shear bands

Shear bands are the main deformation microstructure in the cold rolling process at room temperature [14]. As shown in Figure 2.9 (c) and (d), shear bands generally show non-crystallographic orientations and are associated with deformation bands, while shear bands can pass through grain boundaries or even extend through the specimen [74]. This would be its main difference from deformation bands which are generally found in the individual grains [74].

Similar to deformation bands, the generation of shear bands is associated with the local plasticity accommodated by dislocation slips [78] or twinning [74]. The formation of shear bands in Mg alloys is generally suggested to result from twinning [79, 80]. It is proposed that the CTWs and DTWs will reorient the grains to more favourable orientations for basal slips by 56° and 38°, respectively, and further deformation will result in the connection of these newly

formed twins and form the shear bands [80, 81]. The dislocation density is higher around the shear bands, due to their intensive shear strains [82]. As the formation of shear bands in Mg alloys is strongly related to twins and deformation bands, an in-depth investigation on how shear bands and deformation bands form and evolve would be essential. Rolling tests at room temperature can be an effective method to conduct this investigation, as deformation bands and shear bands were generally observed in the rolling process [14, 75].

2.4 Effects of temperature on microstructures

The temperature has a significant influence on the microstructures of Mg alloys in the deformation process. It is necessary to reveal the effects of temperature on these microstructures and achieve different microstructures. As cryogenic deformation is a promising method to optimize microstructures, and its mechanisms are not well understood, this section also summarizes the up-to-date research on cryogenic deformation.

2.4.1 Temperature effects on slip and twinning

It is generally accepted that the CRSS of twinning is almost independent of temperature, while the CRSS of dislocation slip increases with decreasing temperature [19, 83], as shown in Figure 2.10. As the temperature decreases from T to T_1, the difference of the CRSS between twinning and dislocation slip decreases from $\Delta\sigma_r$ at room temperature to $\Delta\sigma_c$ at cryogenic temperature. Therefore, at the high-temperature T, the onset of deformation is generally related to slip due to the lower CRSS of slip. At the lower temperature T_1, as the value of $\Delta\sigma_c$ is small, the onset of deformation would be related to both slip and twinning. It is worth noting that the temperature dependence of twinning stress and its mechanism are still under debate [19]. For example, as shown in Figure 2.11, the CRSS of tension twin is insensitive to temperature, while the CRSS of compression twin decreases with increasing temperature.

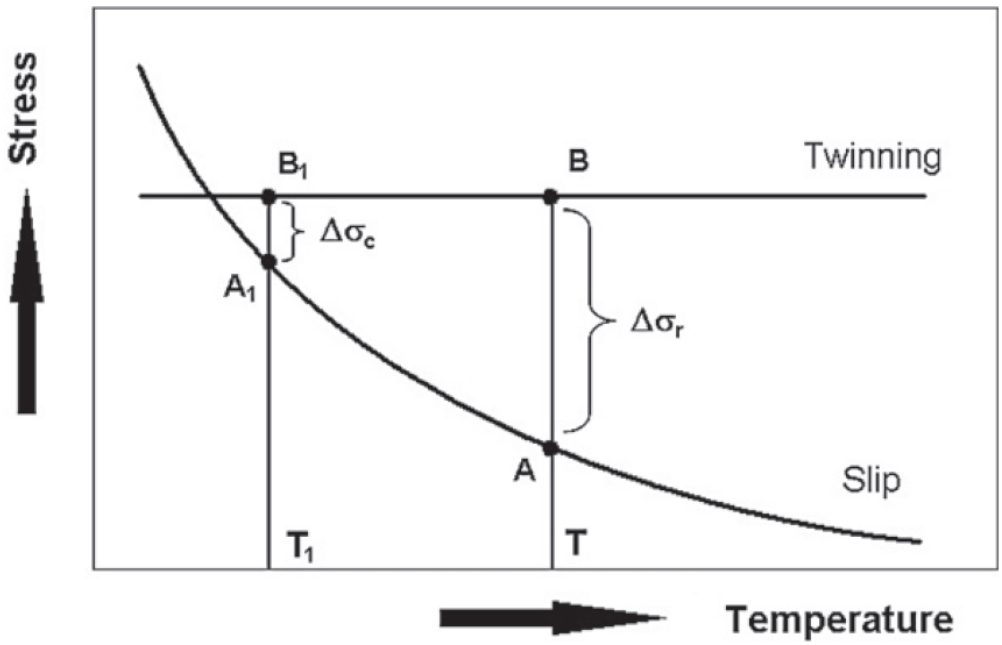

Figure 2.10 Schematic illustrations showing the effect of temperature on twinning and slip [83].

Besides, the temperature sensitivities of individual dislocation slip systems and twinning modes in Mg are different, leading to their different activities as the deformation temperature changes. Figure 2.11 plots the estimated CRSS values of individual slip systems and twinning modes in Mg at 1% strain. The $\{10\bar{1}2\}$ tension twins and basal slips are considered to be approximately athermal, whereas the other slip and twinning modes, including $\{10\,\bar{1}\,1\}$ compression twins are thermally activated to different extents, as their CRSS values increase markedly with decreasing temperature [35, 84]. Therefore, as temperature decreases, it could be easier for $\{10\bar{1}2\}$ tension twins to activate, due to their lower CRSS values.

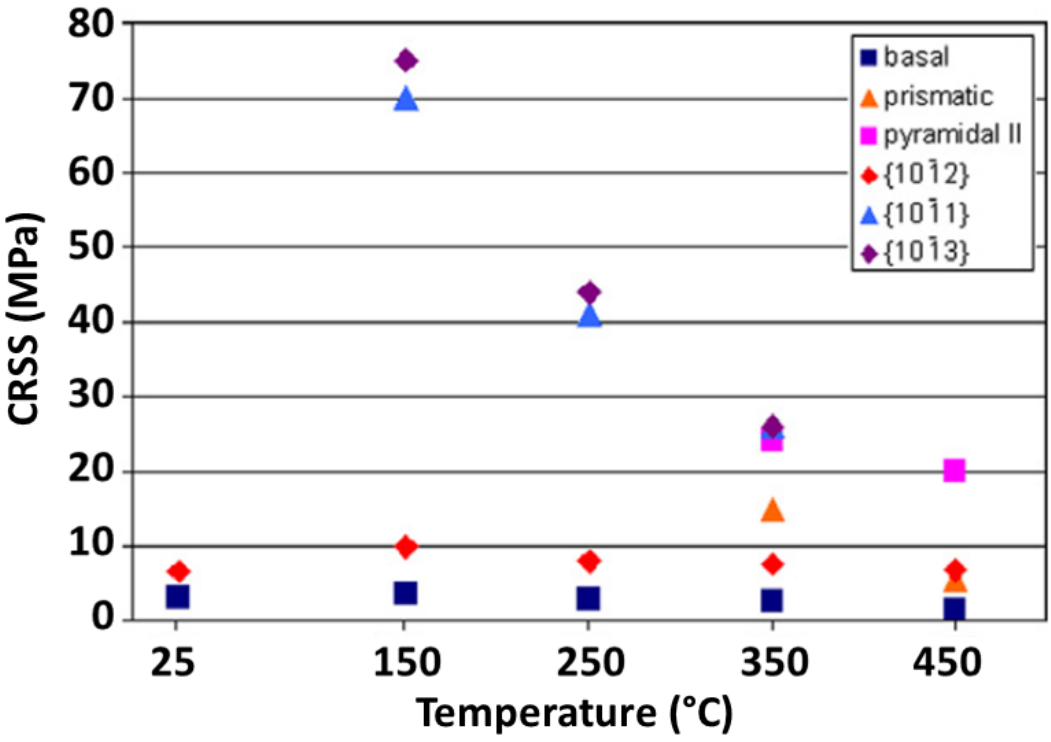

Figure 2.11 Estimated CRSS of the slip and twinning systems in Mg at 1% strain [35].

2.4.2 Cryogenic deformation

Deformation at cryogenic temperature (CT) is a unique testing condition for understanding the fundamental deformation behaviours of Mg alloys, since thermally activated modes can be suppressed. It is also of potential industrial interest if unique textures can be produced using the cryogenic deformation to reduce the strong basal textures produced in conventional Mg alloys (e.g. AZ31) [7, 85].

For this reason, several CT deformation studies have been conducted [72, 86, 87]. A common feature observed was a higher hardening rate at CT [86, 87]. The mechanical behaviour was used to calibrate the visco-plastic self-consistent (VPSC) model, and the model predicted a slight increase in the tension twin activities at CT [86]. The high hardening rate of Mg alloy AZ80 at CT was explained as a result of a combination of texture hardening and reduced dynamic recovery which was a softening mechanism [86]. Although VPSC modelling can provide insights into the operating deformation mechanisms, it does not provide definitive

proof of the behaviour. Revealing the microstructure evolution experimentally in the same regions of interest would provide novel insights into the underlying deformation mechanisms during the cryogenic deformation.

The cryogenic rolling is a potential way to refine the grains. For example, nanostructures were formed in pure titanium (HCP metal) due to extensive twins [83]. As shown in Figure 2.12, the twinned area fraction of pure titanium (Ti) remained higher in cryogenic-temperature (CT) rolling than in room-temperature (RT) rolling, as the thickness reduction (TR) increased from 5% to 20% [73]. The reason would be that more twins in the CT-rolling were activated to accommodate the *c*-axis strain of crystal structure due to the limited <c+a> slips at a lower temperature. Regarding the twin structure, thinner twins and more individual twins in each twinned grain were generated in the CT-rolling than in the RT-rolling. With increasing TR, the number of individual twins increased without apparent twin growth in the CT-rolling. These results indicated that twin nucleation rather than twin growth was the predominant process in the CT-rolling. New twins generally nucleated near grain boundaries, because the local stress concentration at grain boundaries can provide a driving force for twin nucleation [88]. In Ti, the CRSS for slip increased with decreasing temperature, so there were insufficient slip systems to relax the strain misfit with the adjacent grains at CT, resulting in the low deformation compatibility of grains and significant local stress concentration near grain boundaries. The significant stress concentration near grain boundaries in the CT-rolling promoted the twin nucleation and the formation of more individual thin twins [73]. These numerous and thin twins in the CT-rolling of Ti resulted in significant twinning-induced grain refinement. Due to its potential benefit to grain refinement, it is important to study the CT-rolling of Mg alloys. The CT-rolling could also provide a novel way to promote rarely observed twin-twin interactions and twinning sequence and study their behaviours, so the remaining questions mentioned in Section 2.3.1 and 2.3.2 can be well addressed. As the twinning behaviours in Mg alloys are

different from titanium due to their different c/a ratios which could affect the twinning shear values of different twins [89], it would be worth exploiting the different twinning behaviours in Mg alloys during the CT-rolling process.

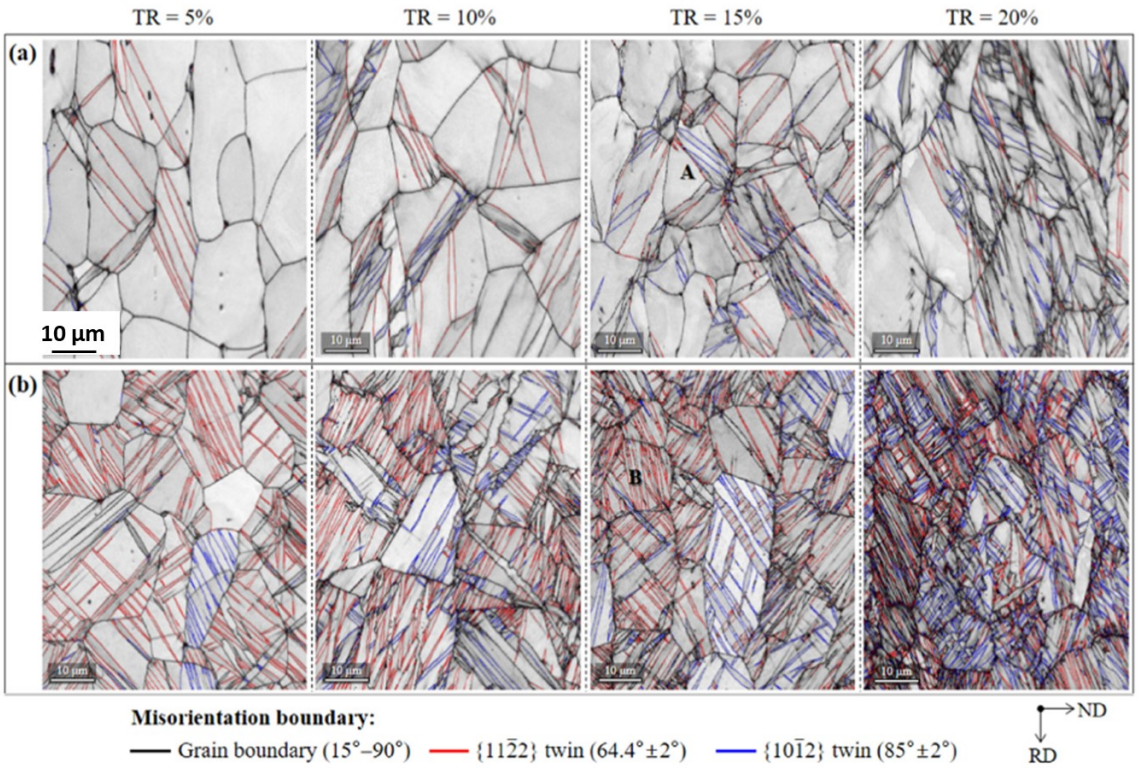

Figure 2.12 EBSD image quality maps of the titanium rolled to thickness reductions of 5%, 10%, 15% and 20%: (a) room-temperature rolling; (b) cryogenic-temperature rolling [73].

2.5 Recrystallization mechanisms

To significantly optimize the grain size and texture, the investigation of recrystallization in these microstructures of deformed Mg alloys is essential. Section 2.5 introduces the recrystallization mechanisms including typical recrystallization nucleation sites and twinning-induced dynamic recrystallization.

2.5.1 Recrystallization nucleation sites

Recrystallization occurs in the thermo-mechanical processing of Mg alloys and has a significant effect on their microstructural and mechanical behaviours [74]. Recrystallization is defined as the formation of a new grain structure by the migration and formation of high angle grain boundaries driven by the stored plastic strain energy [74, 90]. The strain-induced grain boundary migration includes the bulging of a part of pre-existing grain boundary and the formation of the region behind the migrating boundary with a lower dislocation density. The driving force for this grain boundary migration results from the difference of dislocation density on opposite sides of boundaries which are related to the difference of stored energy. The orientation of the new grain is generally similar to the parent grain, so the recrystallization texture could be similar to the texture of the pre-deformed sample [74].

Static recrystallization (SRX) refers to the recrystallization during the annealing process. The typical recrystallization nucleation sites in Mg alloys include deformation twins and deformation bands, which have a significant influence on the texture formation [16, 74, 91]. Twin recrystallization generally contributes to texture weakening [16, 92], while the recrystallization around deformation bands and shear bands results in texture strengthening in conventional Mg alloys [82, 91]. As shown in Figure 2.13 (a), some deformation bands and shear bands formed in the cold-rolled Mg-0.4Zn alloy. After annealing at 350 ℃ for 5 s, recrystallized grains formed and occupied these deformed bands (Figure 2.13 (b)). The recrystallized grains resulted in the formation of the basal texture (Figure 2.13 (d)). As the annealing time increased to 600 s, those recrystallized grains grew and resulted in a stronger basal texture, as shown in Figure 2.13 (c) and (e). These results indicated that the recrystallization around deformation bands and shear bands would form a stronger texture with increasing annealing time [82, 91].

This formation of the stronger texture in the annealed samples was due to the preferential grain growth of the recrystallized basal grains whose *c*-axes were almost parallel to the parent grains and which consumed the grains with other orientations [91]. Note that in the cold-rolled Mg-0.4Zn alloy, the *c*-axes of most grains were parallel to the normal direction and resulted in the strong basal texture (Figure 2.5) [56]. As recrystallized grains generally inherited the orientation of these parent grains, the strong texture would be preserved and strengthened by the preferential grain growth of these recrystallized basal grains [91]. This preferential grain growth was also observed in Mg alloy AZ31, contributing to forming the strong basal texture [13, 58]. The preferential basal grain growth could result from the anisotropic grain boundary energy and mobility in AZ31 alloys, i.e. low energy and mobility of low angle grain boundaries could be responsible for the texture strengthening [13].

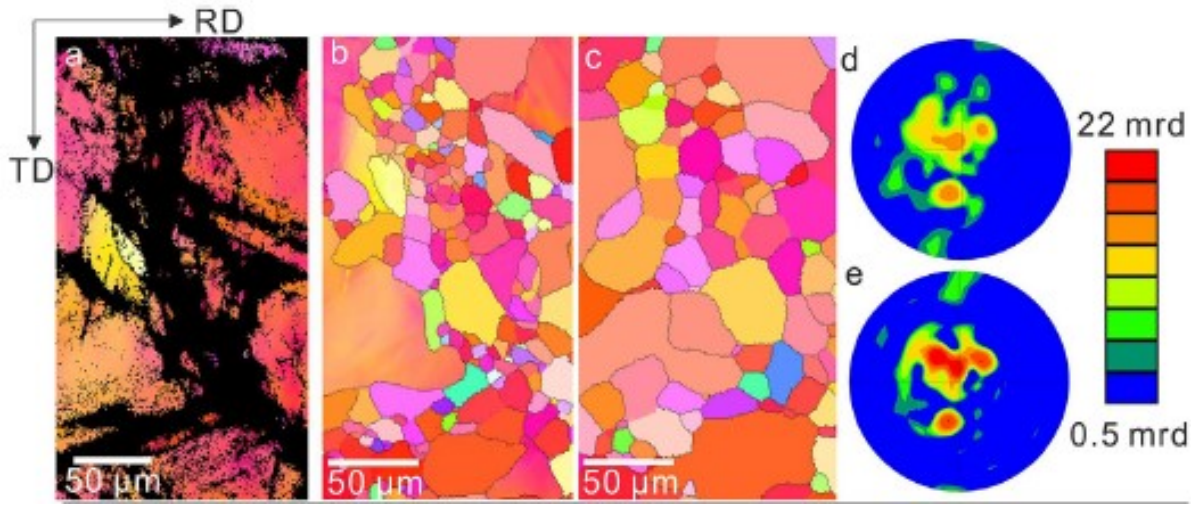

Figure 2.13 Quasi-in-situ EBSD orientation maps in cold-rolled (23% thickness reduction) samples of (a) Mg-0.4Zn, and recrystallized grains after annealing at 350 °C for (b) 5 s and (c) 600 s for Mg-0.4Zn alloy (d, e) (0002) pole figures showing textures of recrystallized grains in maps (b, c) respectively [91].

Deformation twins are also found to act as recrystallization nucleation sites, and the twin recrystallization can usually weaken the texture [16, 92, 93]. Recrystallization was observed near DTWs in an Mg alloy AZ31 sample [17]. It was reasonable to observe the recrystallization

in the DTWs, because they contained high stored energy to provide the large driving force for recrystallization [26, 31], and the stored energy was directly proportional to the dislocation density [74]. The high dislocation density in DTWs would be attributed to their favourable orientation for basal slips, so dislocations tended to accumulate in these fine twins. These DTWs can also affect the recrystallization texture, as they provided a distribution of new orientations [17].

However, tension twins (TTWs), the most common twin type in Mg alloys, are generally difficult to recrystallize [93]. This would be attributed to the following reasons. Firstly, compared to the high CRSS and fine structures in DTWs, the CRSS of TTWs is low, and TTWs can become profuse and coarse at low strains [94]. This would result in low stored energy, which cannot meet the requirement to activate recrystallization [17]. Secondly, it could be difficult for dislocations to accumulate around the boundaries of TTWs, because basal slips were observed to transmit across these twin boundaries to reduce dislocation pile-ups [95] and relieve the local stress near the twin boundaries [93]. Therefore, there are insufficient dislocations and stored energy to activate the recrystallization process around the TTWs.

Differing from a tension twin on its own, twin-twin interactions would create dense twin boundaries and fine structures, resulting in twinning-induced grain refinement and blocking the dislocation slips effectively [64]. High dislocation density could be introduced around twin-twin interactions, contributing to the occurrence of active recrystallization. However, very few studies were conducted on the recrystallization in twin-twin interactions, and the corresponding texture and microstructure evolutions were still unclear.

According to the literature and analysis in Section 2.4.2, extensive twins were expected to form in the cryogenic deformation due to the limited dislocation slips to accommodate the deformation. Those abundant twins in the cryogenically deformed Mg alloys would provide

potential nucleation sites for recrystallization. More importantly, the twin recrystallization in cryogenically deformed Mg alloys can provide a novel way to change the texture and refine the grains. However, the twin recrystallization mechanisms in this process have not been revealed and investigated.

2.5.2 Twinning-induced dynamic recrystallization

Dynamic recrystallization (DRX) is the recrystallization that occurs during deformation at elevated temperatures. Compared to static recrystallization, grain refinement is more effective in twinning-induced dynamic recrystallization [7]. Twinning-induced dynamic recrystallization is specific to Mg alloys. Its nucleation usually results from the subdivision of the primary twin by transversal low-angle grain boundaries (LAGBs) in interiors of these twins, and then these transversal LAGBs would transform into high angle grain boundaries (HAGBs) by increasing their misorientations. Furthermore, with the twin boundaries transforming into random HAGBs, the nuclei bounded by the twin boundaries would transform into recrystallized grains [7].

The dynamic recrystallization was observed in $\{10\bar{1}1\}$ CTWs of a Mg single crystal during the plane-strain compression along the *c*-axis at 370 ℃ [96]. It was found that the recrystallized grains remained the initial *c*-axis orientation of the $\{10\bar{1}1\}$ CTW host, and the basal planes of these grains were randomly rotated around the *c*-axis to form a fibre texture. Figure 2.14 (a) presents the *c*-axis orientation map with respect to the orientation of the *c*-axes relative to the compression direction, the recrystallized grains in the $\{10\bar{1}1\}$ CTW showed the same *c*-axis orientation. This was also confirmed by the (0002) pole figure in Figure 2.14 (b), as the *c*-axes of the recrystallized grains were tilted away from the basal plane normal of the matrix with an angle of ~56°. The $\{11\bar{2}0\}$ pole figure in Figure 2.14 (b) also indicates that there is a shared $[11\bar{2}0]$ rotation axis between the recrystallization grains and the matrix. The angle (~56°) and

[$11\bar{2}0$] rotation axis between the recrystallized grains and the matrix are consistent with the rotation angle and axis of {$10\bar{1}1$} CTW, because {$10\bar{1}1$} CTW generally represents a rotation angle of ~56° around the <$11\bar{2}0$> axis. The reason for the recrystallization in the {$10\bar{1}1$} CTW would be that the compression twin provided favourable orientations for the basal slip and accumulated abundant dislocations for activating recrystallization at a large compressive strain of 1. The dynamic recrystallization near twins was also investigated in a magnesium single crystal during the plane-strain compression along the <$11\bar{2}0$> direction. It was found that the recrystallized grains were rotated around the *c*-axis of their parent twin by an average of 30°, resulting in the formation of the weak texture [97].

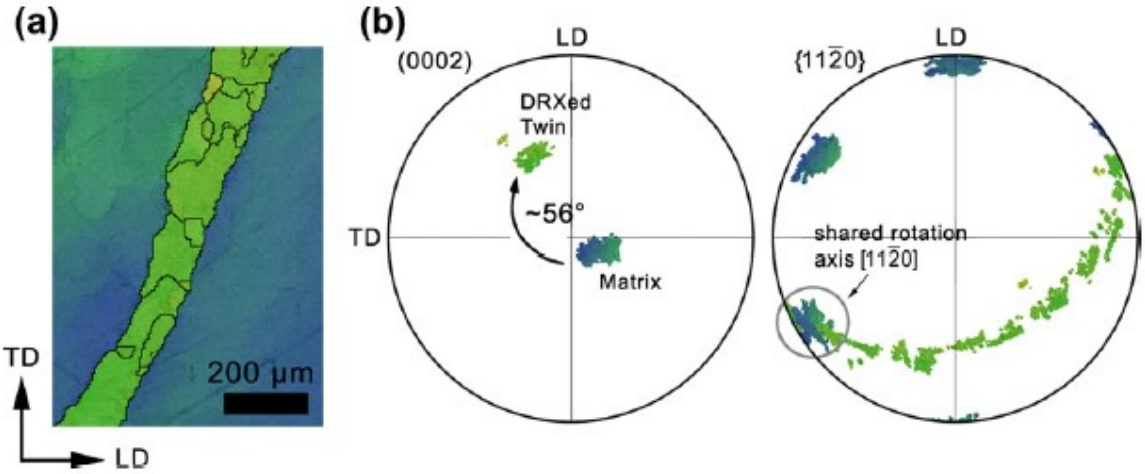

Figure 2.14 (a) c-axis orientation map and (b) corresponding (0002) and {11$\bar{2}$0} pole figures showing the orientations associated with the deformed matrix and the recrystallized twin band at 370 °C and a compressive strain of 1 [96].

The twinning-induced dynamic recrystallization to weaken the texture and refine the grains was also demonstrated in polycrystalline Mg alloys [15, 98]. For example, the twin recrystallization was observed in an extruded Mg alloy AZ31 during compression tests at a high temperature. As shown in Figure 2.15 (a) and (b), recrystallized grains were located in the twins. Some low angle grain boundaries were also observed in the recrystallized twin structure. These low angle grain boundaries firstly formed inside the twin, and gradually accumulated

dislocations and eventually transformed into high angle grain boundaries. As a result, the original twin was fragmented to create new fine grains. It was also found that the recrystallization texture in these twins contributed to weakening the overall texture. The DRX was not observed in those tension twins without low angle grain boundaries (Figure 2.15 (c)), due to few dislocation accumulations in the tension twin [98]. Similar to these recrystallization twins, twin-twin interactions show fine structures and can also accumulate dislocations, so it should be feasible to observe dynamic recrystallization near twin-twin interactions. However, the research on dynamic recrystallization near twin-twin interactions is rarely reported and requires further investigation.

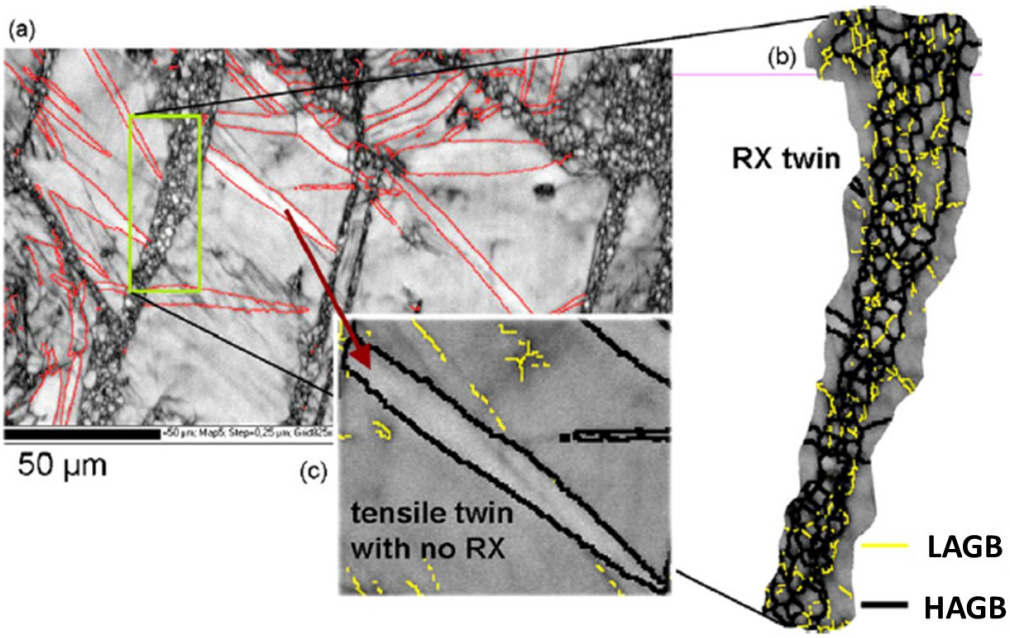

Figure 2.15 (a) EBSD-Kikuchi band contrast map revealing recrystallized twins and {10$\bar{1}$2} tension twins; (b) detailed view of a recrystallized twin indicating the presence of some low angle grain boundaries (thin lines) within the recrystallized structure comprised of high angle grain boundaries (bold lines); (c) neighbouring tension twin showing no recrystallization [98].

2.6 Summary

In this chapter, the main deformation and recrystallization mechanisms in Mg alloys are reviewed. Based on the up-to-date literature, some unsolved scientific questions are identified as follows.

(1) It is unclear how the hot deformation (dynamic recrystallization) combined with pre-deformation at CT and RT affects mechanical properties (i.e. ductility and strength) and microstructures (i.e. texture and grain size). This question is addressed in Chapter 4.

(2) The effects of temperature on dislocation and twinning behaviours, particularly twin-twin interactions, are not well understood at RT and CT. This question is addressed in Chapter 5.

(3) It is still unclear how twin-twin interactions, twinning sequence and deformation bands evolve at different strains and their relationships with dislocations. This question is addressed in Chapter 6.

(4) The recrystallization mechanisms in twin-twin interactions and deformation bands are unclear, and the corresponding microstructure and texture evolution are not reported. This question is addressed in Chapter 4 and 7.

3 Material and experimental methods

3.1 Material

In this section, the material applied in this work is presented. An as-cast magnesium (Mg) alloy AZ31 (Mg-Al-Zn alloys class) was used to conduct the compression and rolling tests at room and cryogenic temperature, subsequent hot deformation and annealing processes. The Mg alloy AZ31 is one of the most commonly used Mg alloys. It was provided by Magnesium Elektron Ltd. The T4 heat treatment was conducted for the as-cast samples at 385 ℃ for 4 hours and then at 420 ℃ for 12 hours to achieve the solution heat-treated state. Table 3.1 presents the chemical compositions of this alloy. For clarity, the general experimental material and methods were introduced in Chapter 3, the specific experimental methods of each chapter were presented in the corresponding chapter.

Table 3.1 Chemical compositions of Mg alloy AZ31 [99]

	Mg	Fe	Mn	Zn	Al	Ca	Ni	Si	Cu	TO
wt%	Bal.	0.004	0.32	0.95	3.1	<0.005	0.0006	0.02	<0.0005	<0.3

TO = Total Others

3.2 Mechanical tests

3.2.1 Compression tests

Compression tests at room and cryogenic temperatures were conducted with an Instron 5584 machine to investigate the mechanical behaviours and microstructures at these temperatures. The set-up of facilities is shown in Figure 3.1. This machine with a 100 kN load cell was equipped with an environmental chamber for cooling the samples. The temperature inside this chamber can be controlled down to -110 ℃, and thermometer 1 was applied to measure the

real-time temperature in the chamber. During the tests at liquid nitrogen temperature (LNT, cryogenic temperature), the samples were immersed in the liquid nitrogen to make the temperature of these samples be -196 ℃. Thermometer 2 was applied to measure the temperature of the sample. The temperature of these testing samples was measured via a RS 5511 digital thermometer, which provided real-time temperature data. Cubic testing samples with 10×10×10 mm^3 were manufactured using an electro-discharged machine (EDM) [100, 101].

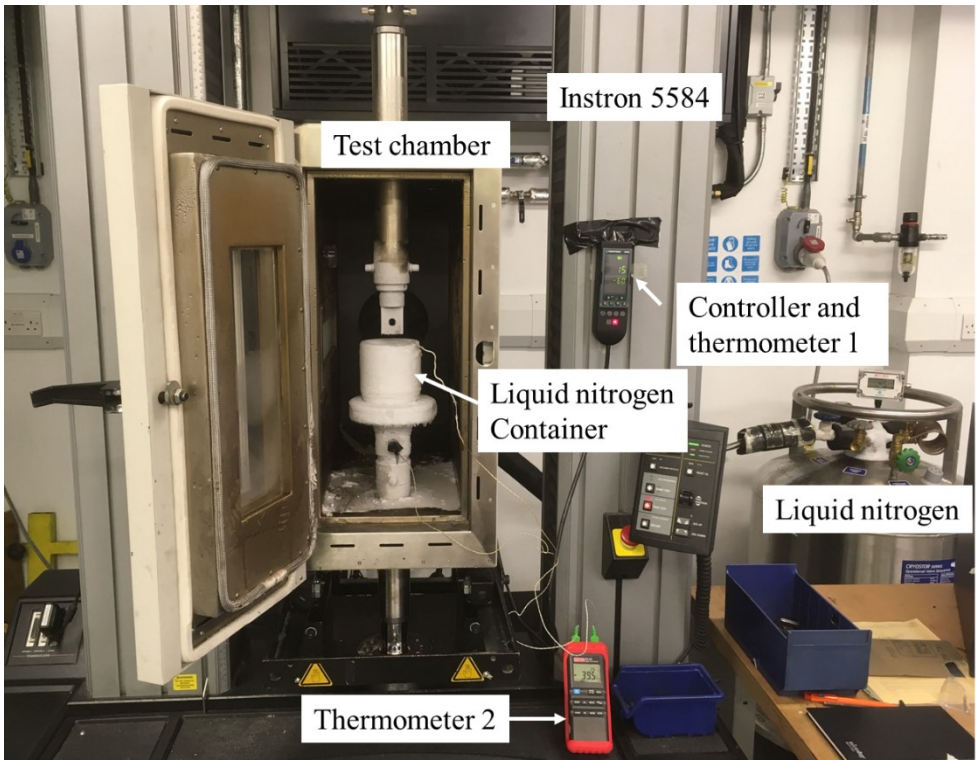

Figure 3.1 Set-up of facilities for the cryogenic compression experiment.

To optimize the grain size and texture in Mg alloys, compression tests at the elevated temperature were conducted with Gleeble 3800 thermo-mechanical materials simulator. This machine has a load capacity of 200 kN in compression tests. Figure 3.2 shows the set-up of facilities for hot compression tests. The materials simulator consists of a control console, a test chamber and a control computer. The sample was fixed between the two grips in the test chamber. A pair of thermo-couples was welded in the centre of the sample surface, and they

were applied to accurately measure the temperature of the sample and provide signals for the feedback control of the temperature. The samples were firstly heated with a heating rate of 5 °C/s to the target temperature and then conducted with the hot compression tests at 300 °C. After that, the air quenching with a cooling rate of 5 °C/s was conducted immediately to retain the microstructure of these hot-deformed samples.

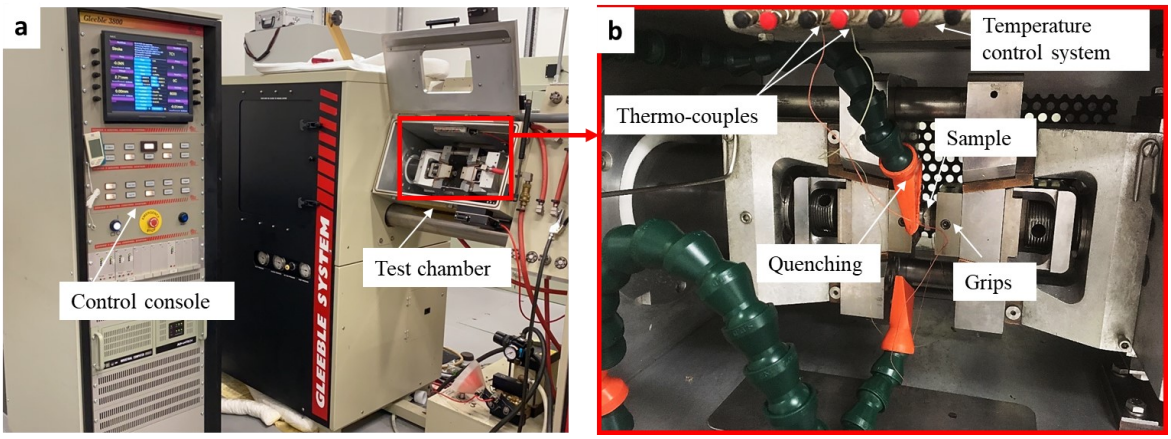

Figure 3.2 (a) Set-up of facilities for the hot compression experiment with Gleeble 3800 thermo-mechanical materials simulator. (b) Test chamber and a sample with thermo-couples.

3.2.2 Tensile tests

Tensile tests were applied to measure the mechanical properties of these hot-deformed samples. As the maximum length of the hot-deformed samples was about 16 mm, the tensile specimens machined from these samples were small-scale. A Deben micro-test machine with a 2 kN load cell was applied to measure the strain-stress curves of these small-scale specimens in tensile tests, as shown in Figure 3.3. In Figure 3.3 (b), two grips were used to fix the specimens. The control system was used to control the moving speed and measure the force. The displacement and force during tensile tests were recorded in the system.

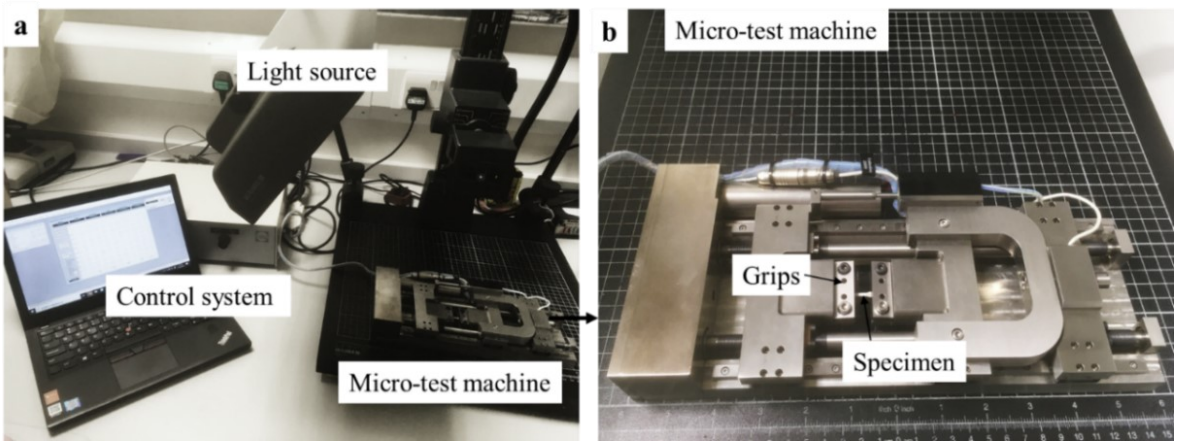

Figure 3.3 (a) Set-up of facilities for the tensile micro-test. (b) Micro-test machine.

3.2.3 Rolling tests

Rolling tests at cryogenic temperature (CT) and room temperature (RT) were applied to study the evolutions of twin-twin interactions and deformation bands, respectively. As shown in Figure 3.4, the rolling tests were conducted with a DRM C130 rolling mill. This rolling mill was used for the sample with a thickness of 3 mm. During the cryogenic rolling process, the samples were immersed in liquid nitrogen for about 30 min to ensure that the entire samples reached the target liquid nitrogen temperature, and then the rolling tests were conducted immediately [21].

To study the recrystallization mechanisms in twin-twin interactions and deformation bands, the CT-rolled and RT-rolled samples were subsequently moved to the adjacent Lenton furnace for the annealing process. A thermometer was used to monitor the actual temperature in the chamber of this furnace. After the annealing process, these samples were water quenched immediately to retain their microstructures.

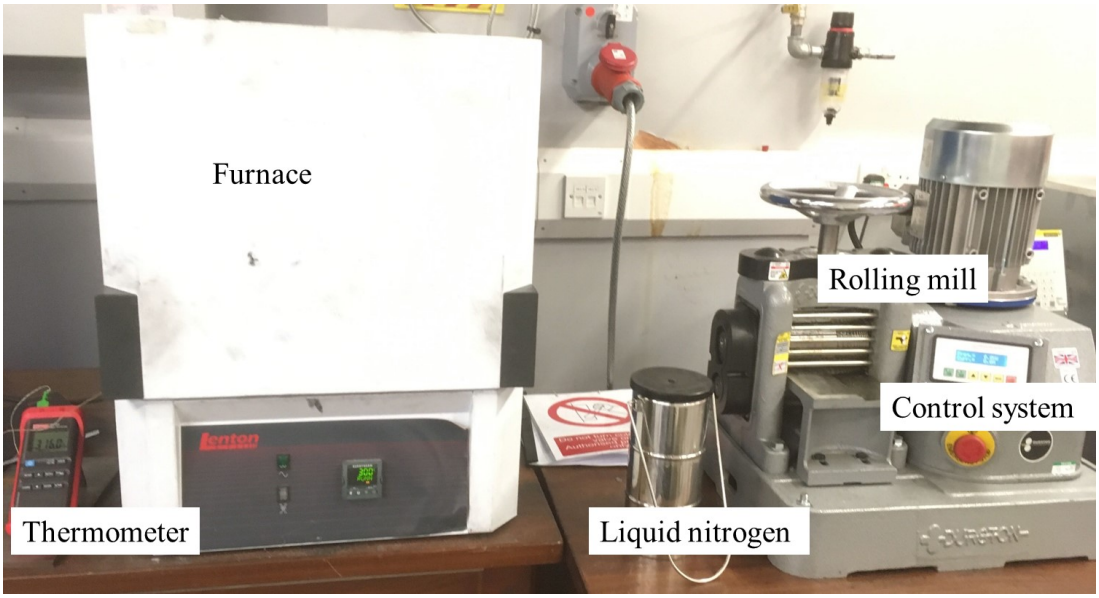

Figure 3.4 Set-up of facilities for the rolling tests at room and cryogenic temperature, and the subsequent annealing process of the rolled samples.

3.3 Microstructure characterization

3.3.1 Electron Backscattered Diffraction (EBSD)

EBSD is applied to analyse the microstructure of these samples, including dislocation, grain orientation, twinning and twin-twin interactions. The selection of EBSD as an appropriate characterisation tool in this work is based on its easy access, simple sample preparation, and relatively statistical representative sampling of grains. The microstructure obtained by EBSD can also be linked with the corresponding macroscopic mechanical properties.

EBSD is a scanning electron microscope-based characterization technique that can obtain the crystallographic information of the probed points. The schematic diagram of the EBSD is shown in Figure 3.5. The EBSD sample is generally tilted by 70° to maximise the intensity of backscattered electrons. A charged-coupled device (CCD) camera is placed at the end of the detector to capture the electron diffraction pattern image formed on the phosphor screen. This technique can be used to measure crystal orientation, crystal type, grain morphology, grain size

and texture [102, 103]. Twin crystallographic information can be accurately determined using EBSD [26, 104].

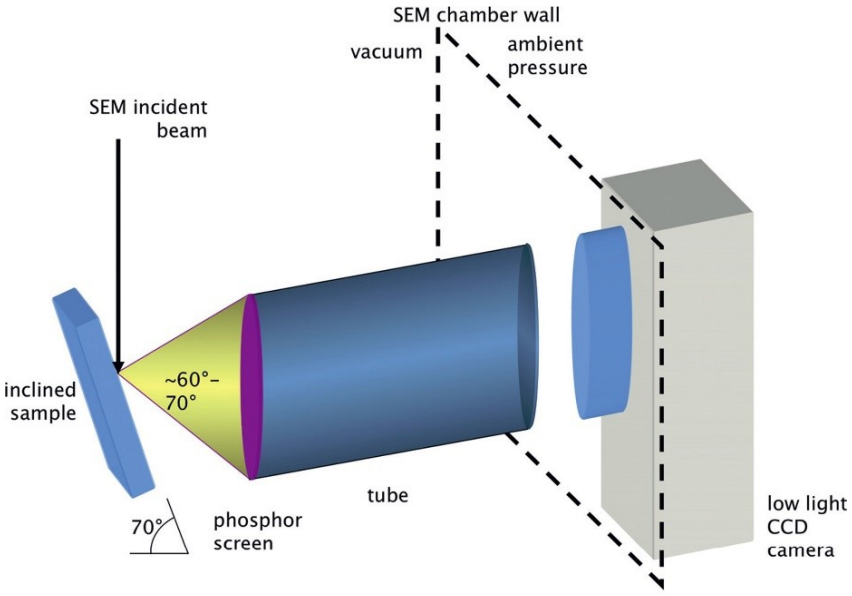

Figure 3.5 Schematic diagram showing the experimental set-up for EBSD observations [105].

EBSD is also becoming more accepted as a robust tool to estimate the distribution of geometrically necessary dislocations (GNDs) in polycrystalline materials [106, 107]. Dislocations can be classified as statistically stored dislocations (SSDs) and geometrically necessary dislocations (GNDs) [107, 108]. GNDs are generated to accommodate the deformation gradient while the SSDs accumulate due to random trapping processes during deformation [108]. GNDs can be obtained from the misorientation values in EBSD, as GNDs can accommodate the lattice curvature and have a geometric effect on the plastic deformation [108]. SSDs cannot accommodate the lattice curvature and were assumed to have no geometrical plastic effect [109], so they cannot contribute to the misorientation measurement in EBSD [106].

In the thesis, the Kernel Average Misorientation (KAM) map (or local misorientation map) is applied to represent GND density distribution. KAM values are calculated using the average

misorientation value between the probed pixel and its surrounding pixels, and then this average value is assigned to that pixel [110]. For a given pixel *j*, the KAM value is calculated by [111]:

$$\mathrm{KAM}(j) = \left[\frac{1}{K}\right]\sum_{k}\omega_{jk} \tag{3}$$

Where *K* is the number of pixels around the pixel number *j* (5 pixels in this work) and ω_{jk} is the misorientation angle between pixel *j* and *k*. The GND density ρ_{GND} can be estimated from the misorientation angle θ between the measuring points at a given distance from each other [110]:

$$\rho_{GND} = \frac{2\theta}{ub} \tag{4}$$

Where *u* is the unit length and *b* is the magnitude of the Burgers vector. The KAM value is generally used for the misorientation angle θ and directly correlated with GND density [112]. Therefore, it is reasonable to represent the GND density distribution with the KAM map [110, 113].

The HKL CHANNEL 5 software was applied to analyse the EBSD data including the KAM map. The twin boundaries were highlighted according to their specific misorientation around the axis, for example, $\{10\bar{1}2\}$ TTWs show ~ 86° about an $<11\bar{2}0>$ axis. The misorientation distribution map was also applied to identify the twin types in the deformed samples, for example, $\{10\bar{1}2\}$ TTWs can be identified by the misorientation peak at ~86° about the $<11\bar{2}0>$ axis in the map. The grain size was calculated with a critical misorientation of 5° and a minimum grain area of 10 pixels. The average grain size was weighed by area fraction and included boundary grains. The texture in these samples was analysed using the pole figure, because the pole figure was a typical statistical method to represent the positions and intensities of specific crystallographic orientations of the grains and widely used to present the texture of

Mg alloys [16, 114]. The subset figures of the EBSD information were obtained using the subset selection component in the software.

In the sample preparation for the EBSD measurements, the testing samples were ground with 2500 and 4000 grit SiC paper for ~ 5 minutes and then polished with OPS suspension for ~15 minutes. They were placed in a Hitachi 3400 SEM microscope with a Bruker e-Flash, Quantax Esprit 2.1 EBSD system. The 25 KeV electron beam was selected to conduct the EBSD tests.

3.3.2 Etching and optical microscopy

To identify the deformation bands and twins in the rolled samples, the surfaces of Rolling Direction (RD) × Normal Direction (ND) of these samples were prepared for optical microscopic examinations. The rolled samples were mechanically polished using P4000 SiC grinding papers and OPS suspension. Then, the samples were chemical-etched using mixed solutions of 1 ml nitric acid, 1 ml acetic acid, 1 ml oxalic acid and 150 ml water for about 30 s. A Zeiss optical microscope was employed to observe the microstructure of these etched samples.

4 A novel cryogenic-hot deformation method to achieve fine grains and a weak texture in Mg alloy AZ31

4.1 Introduction

The mechanical properties of Mg alloy AZ31 including ductility and strength after hot deformation processes are limited, due to the formed coarse grains and strong texture. In this chapter, the novel method combining hot compression with the pre-deformation at cryogenic and room temperature was developed to refine the grains and weaken the texture, resulting in the improved ductility and strength of Mg alloy AZ31. The direct hot compression, which was a common thermo-mechanical process, was also conducted as a benchmark.

To examine the effects of pre-deformation, the mechanical properties of hot-deformed samples with pre-deformation at cryogenic temperature (CT-HD) and room temperature (RT-HD) were measured with tensile tests, compared with direct-hot-deformed (direct-HD) samples. To explain the mechanical properties of these samples, their underlying microstructures, including texture and grain size, were characterised using EBSD. Furthermore, the dynamic recrystallization mechanisms of these hot-deformed samples near twins and deformation bands during the hot deformation were revealed with the detailed microstructure analysis. The evolution of twins and dislocations in the cryogenic deformation was briefly introduced in this chapter, while the more comprehensive research on the mechanical behaviours and their relationship with the microstructures in the cryogenic and room-temperature deformation was conducted in subsequent Chapter 5. This chapter demonstrates that the proposed cryogenic-hot deformation process can be a potential innovative manufacturing method for producing high-performance Mg alloys with fine grains and a weak texture.

4.2 Experimental programme

4.2.1 Material and experimental tests

The material used in this research was an as-cast Mg alloy AZ31 (Mg-Al-Zn alloys class) in a T4 temper. The dimension of these samples was 10 mm × 10 mm × 10 mm. A schematic of the experimental approach is illustrated in Figure 4.1 (a). The samples were pre-compressed with an Instron 5584 machine at a nominal strain rate of 1 s^{-1}, room temperature (RT) and cryogenic temperature (CT) (liquid nitrogen temperature) to a strain of 0.08. To achieve CT, these samples were immersed in liquid nitrogen during the compression tests, as shown in Figure 3.1 in the methodology Section 3.2.1.

The subsequent uniaxial compression tests at high temperature were conducted with a Gleeble 3800 materials thermo-mechanical simulator, as shown in Figure 3.2. As the recrystallization temperature of Mg alloy AZ31 is generally between 250 and 450 °C [115], the hot compression tests of the RT-deformed and CT-deformed samples were conducted at 300 °C, 0.01 s^{-1} to the final strain of about 0.33 and 1.08. As a benchmark, the hot compression tests at the same temperature and strain rate were also directly conducted on the as-cast samples to the same final strain of 0.33 and 1.08.

Figure 4.1 (b) plots the true stress-strain curves in the hot compression of the direct-HD, RT-HD and CT-HD samples, respectively. The flow stress in these curves all shows an increase and a subsequent decrease with increasing strain, indicating a softening in the late stage of the compression test. The decrease in flow stress could be mainly attributed to the occurrence of dynamic recrystallization. The detailed microstructure analysis of the recrystallization can be seen in the following section.

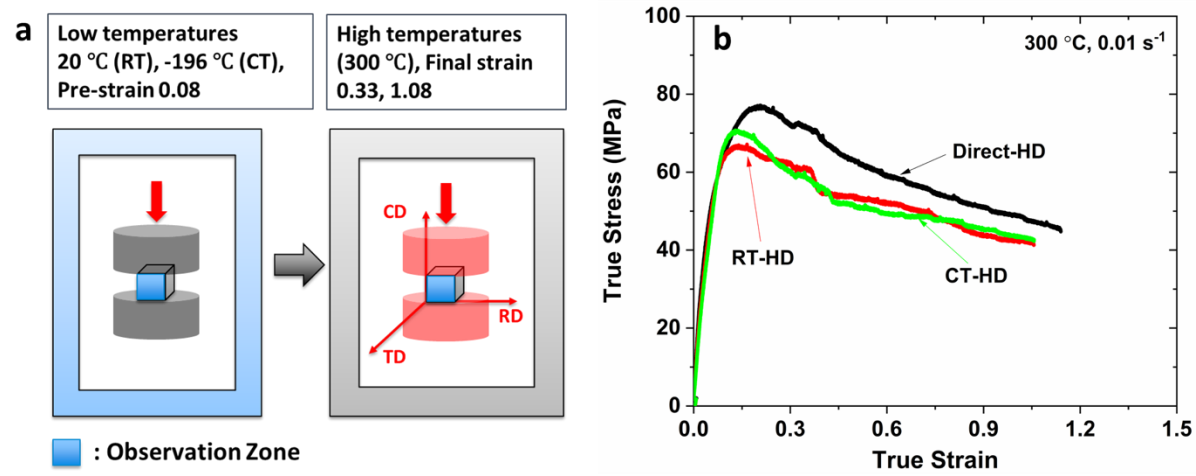

Figure 4.1 (a) A schematic of the experimental compression procedures showing pre-compression at RT and CT, and the subsequent hot compression. (b) The true stress-strain compression curves for the direct-HD sample, RT-HD and CT-HD Mg alloy AZ31 samples deformed at 300 °C, 0.01 s^{-1}, respectively.

Tensile tests at room temperature were conducted to evaluate the mechanical properties of the direct-HD, RT-HD and CT-HD AZ31 samples with the final imposed compression strain of 1.08. These tests were carried out using a Deben micro-test machine at a speed of 0.2 mm/min (Figure 3.4). The tensile specimens with gauge dimensions of 5 mm × 2 mm × 0.5 mm were machined along the central part of these hot-deformed samples. At least three tests were conducted for each condition to ensure the reliability of the results.

4.2.2 Microstructure characterisation

EBSD was applied to characterise the microstructure of these samples. These EBSD measurements were conducted with a Hitachi 3400 scanning electron microscope (SEM) equipped with a Bruker e-Flash, Quantax Esprit 2.1 system. The hot-deformed samples were scanned at a step size of 1.5 µm which was sufficient to obtain all essential information, and a step size of 0.8 µm was selected to obtain more detailed information of the smaller zone. The CT-deformed sample was scanned at a step size of 3 µm. The HKL CHANNEL 5 software was applied to analyse the EBSD data, including grain size, texture (pole figure) and KAM maps, and the analysis details can be seen in Section 3.3.1.

4.3 Experimental results

4.3.1 Mechanical behaviours of deformed Mg alloy AZ31

The true stress-strain curves of tensile tests are presented in Figure 4.2. The ductility (elongation to fracture, EL), 0.2% proof stress (yield strength, YS), fracture strength (FS) and of the initial sample are 15%, 56 MPa, and 211 MPa, respectively. Regarding the initial sample after hot compression tests at 300 °C directly (direct-hot-deformed sample, direct-HD), the YS, FS of the direct-HD sample increase to 92 MPa, 253 MPa, but its EL decreases to 10%. However, the RT-deformed sample after hot deformation (RT-HD) shows an increase in EL, YS and FS to 17%, 98 MPa and 301 MPa, respectively. The CT-deformed sample after hot deformation (CT-HD) shows the highest EL, YS and FS of 21%, 111 MPa and 321 MPa, which show the increasing rate of 40%, 98% and 52%, compared to the initial sample. The EL and FS of the CT-HD sample increase by 110% and 27%, compared to the direct-HD sample.

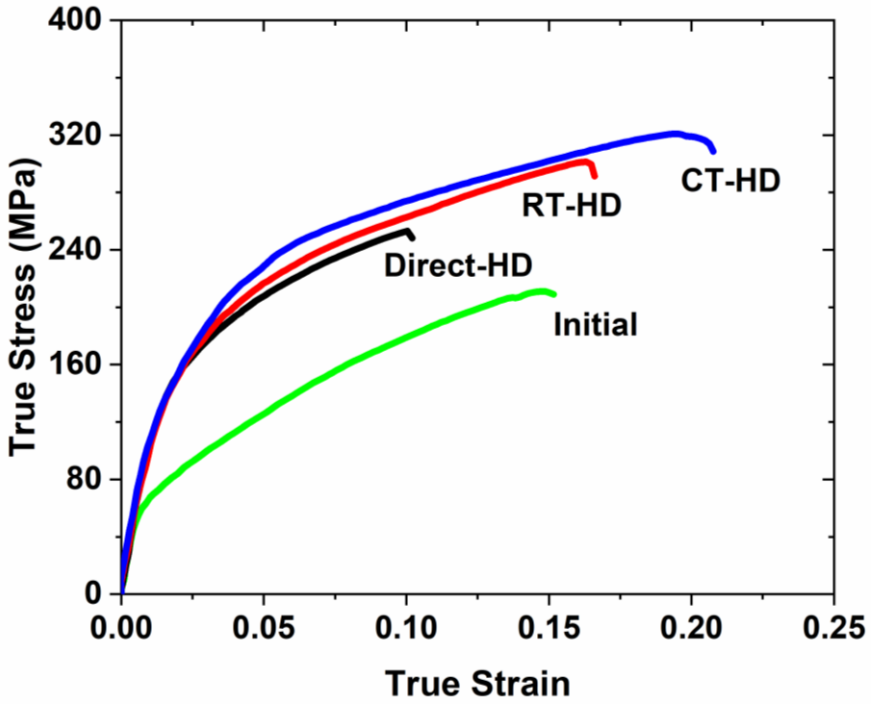

Figure 4.2 The true stress-strain tension curves for the initial sample, and direct-HD, RT-HD and CT-HD samples, respectively.

4.3.2 Microstructural behaviours in the hot-deformed samples with pre-deformation

The microstructural behaviours of these hot-deformed samples with a final strain of 1.08 are analysed to explain the mechanical behaviours in Figure 4.2. The inverse pole figure (IPF) maps of these samples are plotted in Figure 4.3. The IPF map of the initial sample is plotted in Figure 4.3 (a), and it shows the homogenous microstructure with coarse grains. In Figure 4.3 (b), after hot compression tests at 300 ℃ for the initial sample directly (direct-HD), the microstructure of this direct-HD sample is inhomogeneous with some coarse grains. The hot-deformed sample with RT-pre-deformation (RT-HD) also consists of coarse and fine grains, but the grains in the RT-HD sample are much finer than those in the direct-HD sample, as shown in Figure 4.3 (b) and (c). The hot-deformed sample with CT-pre-deformation (CT-HD) (Figure 4.3 (d)) shows a much finer microstructure with fewer coarse grains than the RT-HD sample. These results indicate that pre-deformation, especially at CT, would significantly enhance the grain refinement in the subsequent hot deformation process.

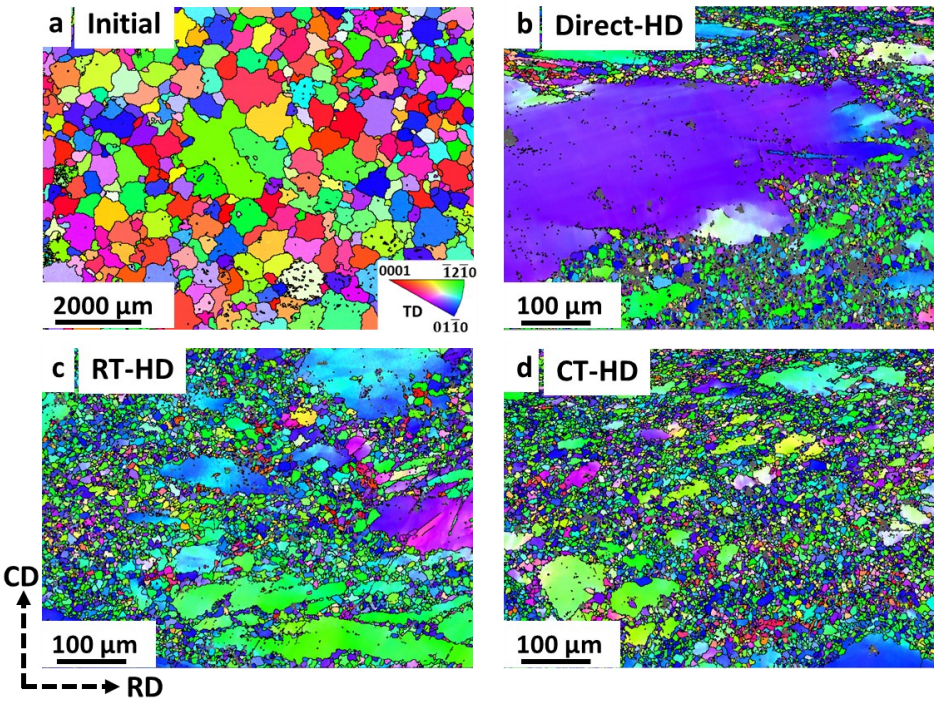

Figure 4.3 EBSD IPF maps of (a) initial sample, and (b-d) the hot-deformed samples at 300 ℃ to a final strain of 1.08 (b) directly (direct-HD), (c) with RT-pre-deformation (RT-HD), and (d) CT-pre-deformation (CT-HD).

The average grain sizes of these samples are calculated and plotted in Figure 4.4 to compare their grain size information quantitatively. The average grain size of the initial sample is 565 μm. The average grain size of the direct-HD sample is 205 μm. However, the average grain size of the RT-HD sample is 39 μm, which is one-fifth of that of the direct-HD sample. This indicates that the pre-deformation contributes to the effective grain refinement. The CT-HD sample shows a much finer average grain size with 17 μm, compared to the RT-HD sample, indicating that the grain refinement in the hot deformation process with the CT-pre-deformation is more effective than that with the RT-pre-deformation. Besides, the fine-grained microstructure in the CT-HD sample would contribute to its high strength and ductility, as shown in Figure 4.2. The grain size distribution of these hot-deformed samples is shown in Supplementary Figure A.1. More coarse grains are observed in the direct-HD and RT-HD samples, while the fine grains dominate in the CT-HD sample. This indicates that the grain refinement is more effective in the CT-HD sample.

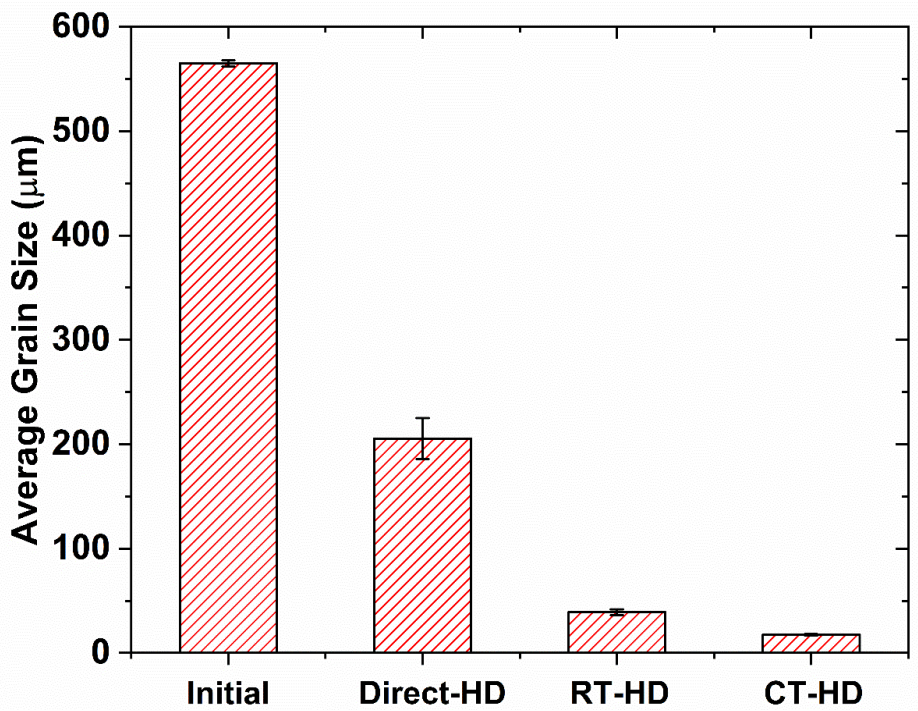

Figure 4.4 Average grain size in the initial, direct-HD, RT-HD, and CT-HD samples.

The texture analysis is also conducted for these hot-deformed samples, and their corresponding {0001} pole figures are plotted in Figure 4.5. As the initial sample is an as-cast alloy, its texture is random and weak (Figure 4.5 (a)). Regarding the hot-deformed samples, the direct-HD sample shows the strongest texture with a maximum intensity of 70.31 mud in Figure 4.5 (b). The texture of the RT-HD sample (Figure 4.5 (c)) is weaker than that of the direct-HD sample, and the CT-HD sample shows the weakest texture with 10.03 mud in Figure 4.5 (d). This result indicates that pre-deformation, especially CT-deformation, weakens the texture in the hot deformation process. The weaker texture in the CT-HD sample would contribute to its higher ductility (Figure 4.2). The different textures and grain sizes in these hot-deformed samples would be attributed to their different recrystallization behaviours in the hot deformation processes. In addition, the {0001} pole figures in fine-grained zones of these hot-deformed samples are shown in Supplementary Figure A.2. The fine-grained zone is defined as the grains whose size are smaller than 25 μm. It is found that the CT-HD sample also shows the weakest texture in the fine-grained zone.

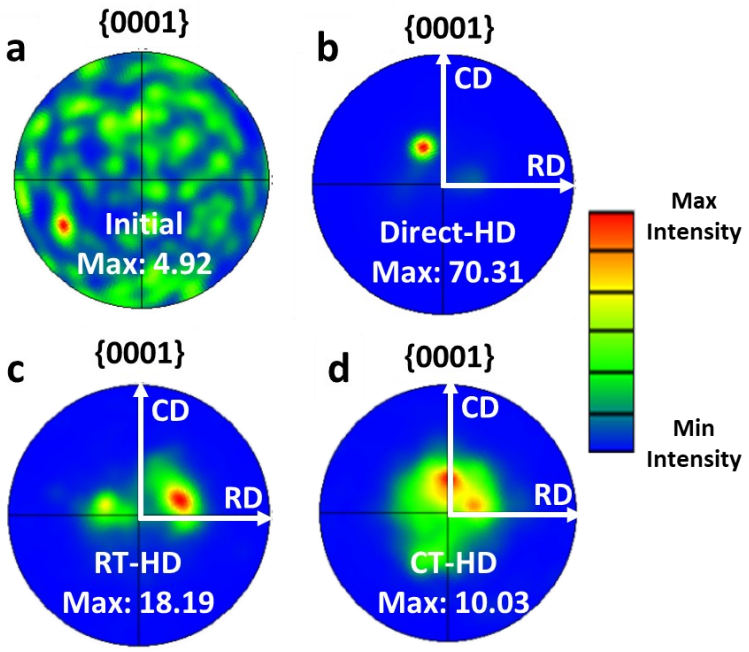

Figure 4.5 {0001} pole figures of (a) initial sample, (b) direct-HD sample, (c) RT-HD sample, and (d) CT-HD sample. The unit of the colour bar is in multiples of a uniform distribution (mud).

Figure 4.6 plots the detailed microstructure analysis of the fine-grained zone in the CT-HD sample. It shows a homogenous microstructure and ultra-fine grains with an average grain size of 7 μm, as shown in Figure 4.6 (a) and (b). Compared to the average grain size of 565 μm in the initial sample, the significant grain refinement by about 80 times is achieved in the CT-deformed sample after the hot deformation. This result confirms that cryogenic pre-deformation combined with hot deformation would result in significant grain refinement.

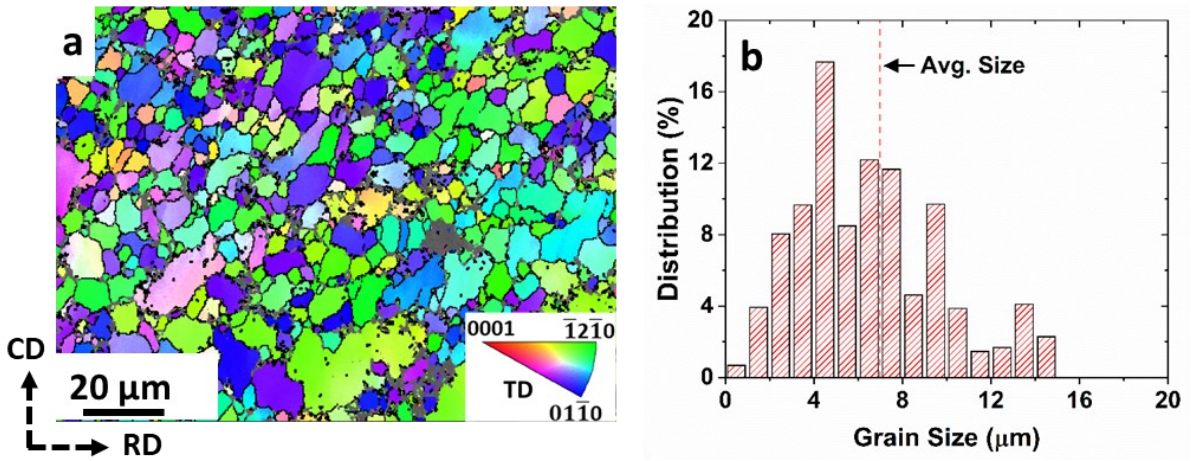

Figure 4.6 (a) IPF map and (b) grain size distribution in the CT-HD sample.

4.3.3 Microstructural evolution during cryogenic deformation and subsequent dynamic recrystallization

As shown in the previous section, the CT-deformed sample after hot deformation shows the homogenous microstructure with fine grains and the weak texture. In order to understand the deformation and recrystallization mechanisms in this cryogenic-hot process, a systematic microstructure analysis is conducted.

A *quasi-in-situ* EBSD analysis is conducted for the CT-deformed sample with a strain of 0.08 to investigate the deformation mechanism, and its microstructure evolution is shown in Figure 4.7. The microstructure of the initial sample is shown in Figure 4.7 (a), and its KAM value is low (Figure 4.7 (c)). After deformation at CT, abundant twin boundaries, especially $(10\bar{1}2)$-

(01$\bar{1}$2) twin-twin interactions, are generated in the sample. Grain A is selected to show the twinning behaviour during the cryogenic deformation in detail. In Figure 4.7 (e), two tension twin variants A2 and A3 are generated in the matrix AM1 to form (10$\bar{1}$2)-(01$\bar{1}$2) twin-twin interactions, and almost the entire grain A is consumed by these two twin variants. These two twin variants A2 and A3 show different orientations and are located away from the centre of the {0001} pole figure, contributing to weakening the texture. In addition, the KAM value is high around these twin boundaries, especially the interacting twin boundaries, indicating that the dislocation density is high in these sites, as shown in Figure 4.7 (d) and (e). These sites with high dislocation density, mainly the boundaries of twins and twin-twin interactions, would be the preferential recrystallized sites and enhance the recrystallization in the subsequent hot deformation process. The relationship between twin-twin interactions and texture, and the relationship between dislocation and twinning at room-temperature and cryogenic deformation are comprehensively investigated in Chapter 5.

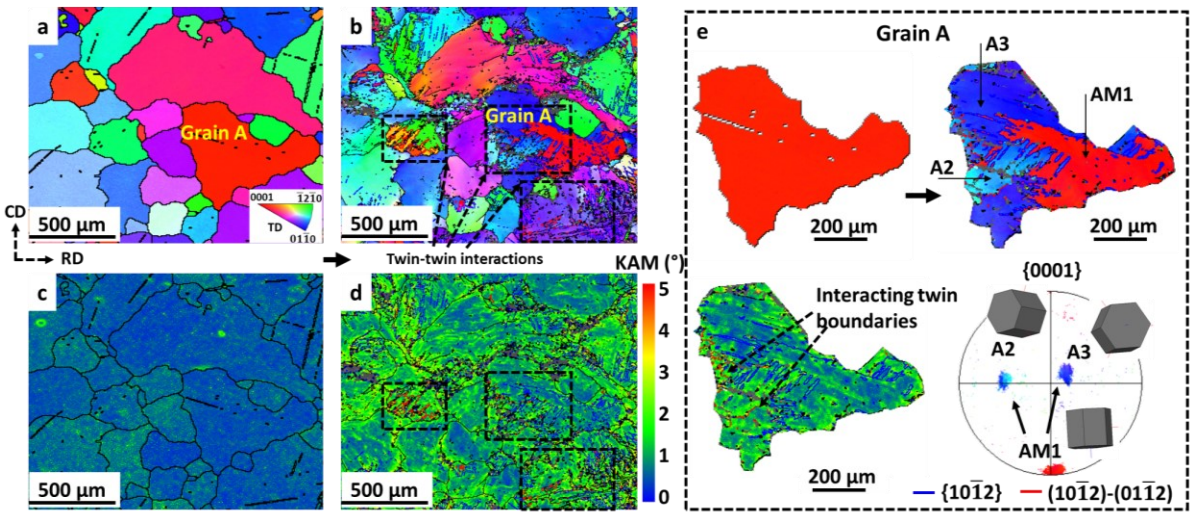

Figure 4.7 IPF maps of (a) the initial Mg alloy AZ31 sample and (b) the CT-deformed sample with a strain of 0.08, and the corresponding KAM maps of (c) the initial Mg alloy AZ31 sample and (d) the CT-deformed sample, and (e) the IPF map, KAM map and orientation evolution in grain A, respectively.

The microstructure analysis of the CT-deformed sample during the subsequent hot compression process at 300 ℃ is shown in Figure 4.8. As shown in Figure 4.8 (a) and (b), at

the final deformation strain of 0.33, some recrystallized grains with fine structures are observed and mainly located around the twin boundaries, especially the boundaries of $(10\bar{1}2)$-$(01\bar{1}2)$ twin-twin interactions. According to its KAM map in Figure 4.8 (c), the KAM value is high near some remaining twin boundaries, which could become the recrystallization sites and contribute to further recrystallization. Therefore, the twins and twin-twin interactions in the CT-deformed sample provide abundant sites for active dynamic recrystallization in the hot deformation process. The active recrystallization can result in the formation of the homogenous microstructure and fine grains in Figure 4.3 (d).

The typical Zone B in Figure 4.8 (a) is selected to analyse the recrystallization mechanisms in the CT-deformed sample. As shown in Figure 4.8 (d), abundant recrystallized grains are located in the regions that show elongated shapes similar to those of the twin bands and are bounded by matrix grains of identical orientations. Although the character of twin boundaries is lost after dynamic recrystallization, the misorientations between the recrystallized grains and their neighbour matrix grains still share the $[11\bar{2}0]$ axis or the $[01\bar{1}0]$ axis or their equivalent axes. The results indicate that these recrystallized grains are generated around the boundaries of $(10\bar{1}2)$-$(01\bar{1}2)$ twin-twin interactions, as these twin-twin interactions are formed by two $\{10\bar{1}2\}$ TTWs and occupy the $[11\bar{2}0]$ axis or the $[01\bar{1}0]$ axis. In Figure 4.8 (e), the orientations of these recrystallized grains, such as grain B1, B2 and B3, are different from the orientation of the matrix BM, and a broad and weak texture with the maximum pole density being located along the RD is shown in the {0001} pole figure. The various orientations would also promote the activation of dislocation slips and result in dislocation accumulations near the boundaries. According to Figure 4.8 (f), the KAM value is high near the boundaries, which could promote further recrystallization in the hot deformation process. Therefore, the dynamic recrystallization around twin-twin interactions is active, resulting in texture weakening and grain refinement.

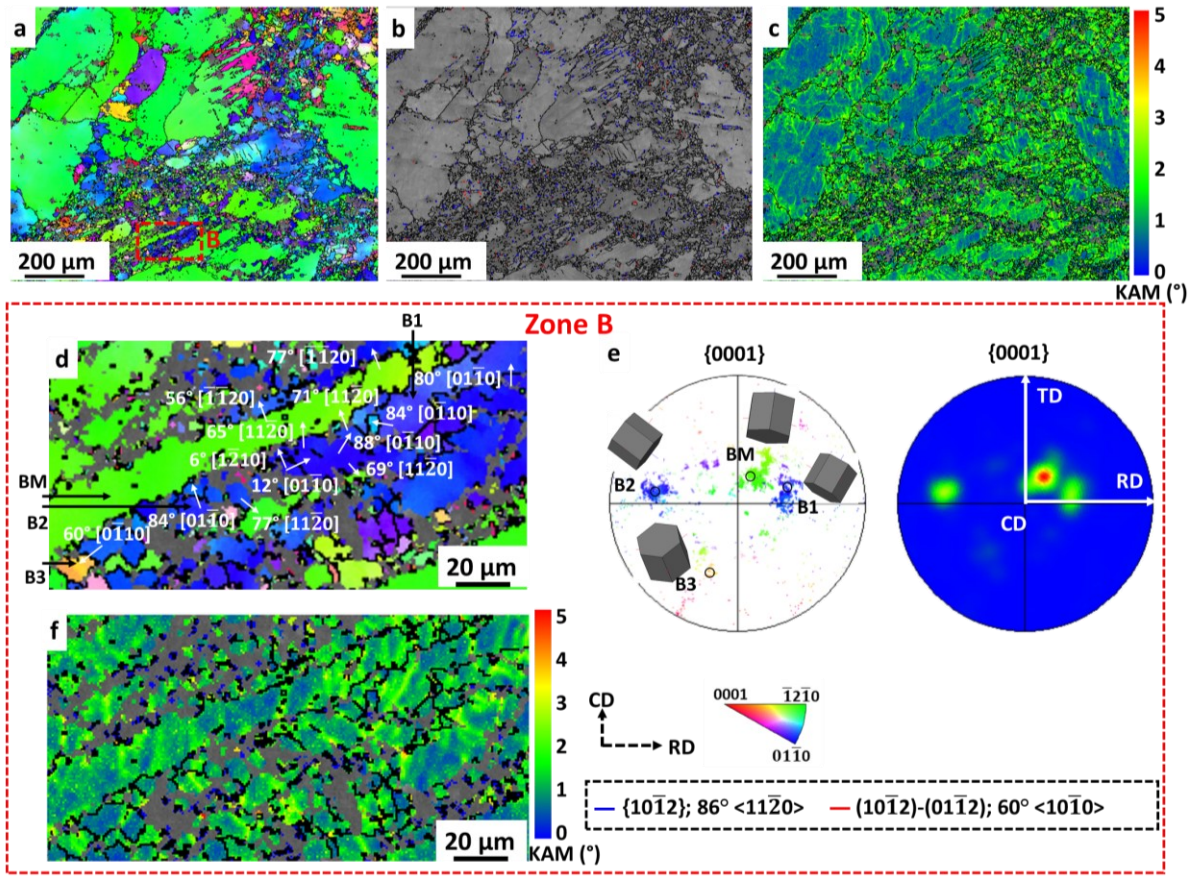

Figure 4.8 (a) IPF map, (b) band contrast map with twin boundaries, and (c) KAM map in the CT-HD sample with a final strain of 0.33, respectively. (d) IPF map, (e) {0001} pole figure, and (f) KAM map in the Zone B of this sample, respectively.

4.3.4 Microstructures in the hot deformation process for the direct-HD and RT-HD samples

The microstructure analysis of the direct-HD and RT-HD samples with a total strain of 0.33 was conducted to study the dynamic recrystallization behaviours. The detailed investigation of the microstructures in the RT-deformed sample was conducted in Chapter 5 and 6. Figure 4.9 (a-c) shows the IPF map, the band contrast map with twin boundaries, and the KAM map of the direct-HD sample. The recrystallized area fraction is low in this sample, and the dynamic recrystallization mainly occurs around the deformation bands including the deformed areas near grain boundaries.

Figure 4.9 (d-i) plots three typical zones in this area. The main recrystallization region in this sample is around deformation bands, as shown in Figure 4.9 (d) and (g). Abundant recrystallized grains are fine and located around the deformation bands in Zone C, while almost no recrystallization occurs in the regions away from the deformation bands. This could be attributed to the high KAM value around the narrow region of deformation bands, which would accumulate abundant dislocations and provide sufficient stored energy to promote recrystallization. In Figure 4.9 (e), TTWs are observed in Zone D and show the coarse structure. According to Figure 4.9 (h), some sites with high KAM values spread in the twin variant D1 and show 'string-like' feature from one twin boundary to another twin boundary. In Figure 4.9 (f) and (i), the CTWs also show the coarse structure, and few sites with high KAM values are distributed in the twin variant E1. However, no recrystallized grains are observed around these TTWs or CTWs. These results indicate that deformation bands are the preferential sites for recrystallization in the direct-HD sample, compared to TTWs and CTWs.

Compared with the CT-HD sample (Figure 4.8), fewer recrystallized areas are observed in the direct-HD sample. The recrystallization in the hot deformation of the direct-HD sample mainly occurs around the deformation bands and grain boundaries, while in the CT-HD sample, the twin boundaries are the main recrystallization sites. Therefore, more recrystallized sites near twin boundaries in the hot deformation of the CT-HD sample would enhance the recrystallization and form the fine-grained microstructure.

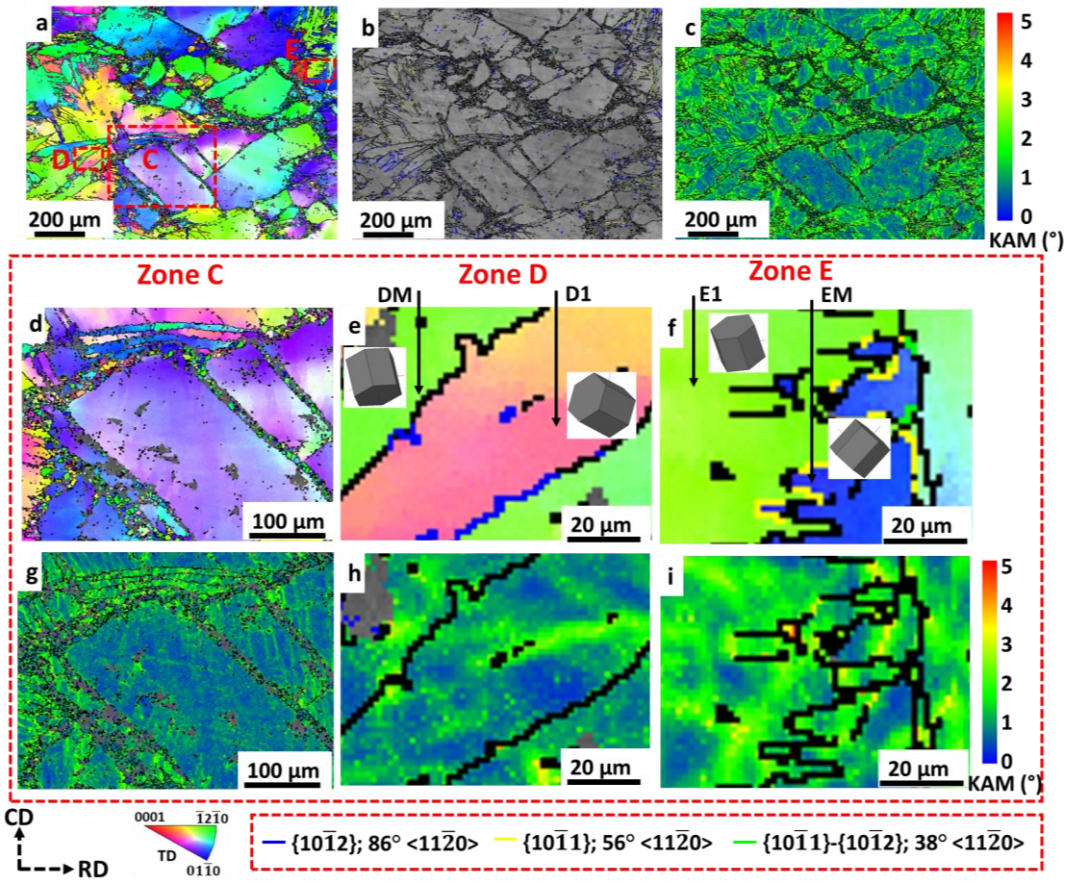

Figure 4.9 (a) IPF map, (b) band contrast map with twin boundaries, and (c) KAM map in the direct-HD sample with the final strain of 0.33, respectively. (d-f) IPF maps and corresponding (g-i) KAM maps in Zone C, Zone D and Zone E of this sample, respectively.

Figure 4.10 plots the microstructure analysis of the RT-HD sample with the total strain of 0.33 in hot deformation. Similar to the direct-HD sample (Figure 4.9), in Figure 4.10, dynamic recrystallization mainly occurs around the deformation bands including the deformed areas near grain boundaries, but more sites with high KAM values are observed in the RT-HD sample, which would promote its dynamic recrystallization. Figure 4.10 (b) shows a typical zone where recrystallized grains are located in the narrow regions of deformation bands. In Figure 4.10 (c) and (d), the KAM value is high around the deformation bands, which would provide the stored energy for further recrystallization. Furthermore, the detailed analysis of recrystallization mechanisms and corresponding microstructure evolution near deformation bands and twin-

twin interactions in the RT-deformed and CT-deformed samples was comprehensively conducted in Chapter 7.

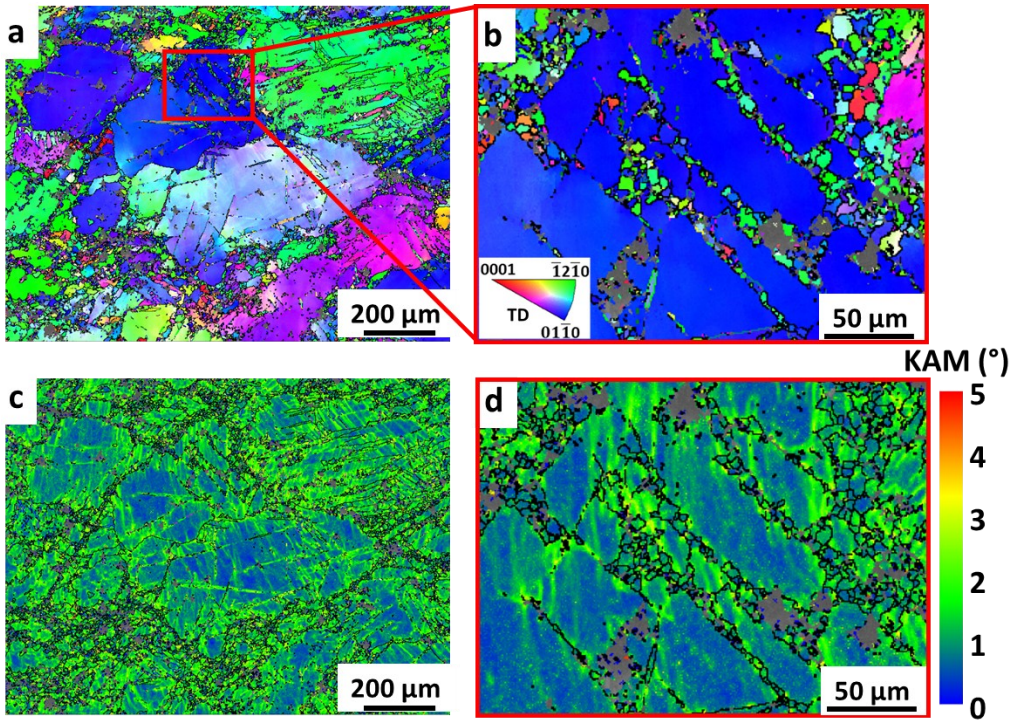

Figure 4.10 (a) IPF map, (c) KAM map, and the corresponding (b) enlarged IPF map and (d) KAM map in the RT-HD sample with the final strain of 0.33, respectively.

4.4 Discussion

4.4.1 Recrystallization near twins in the CT-HD sample during hot deformation

The significant grain refinement and texture weakening in the CT-HD sample would be attributed to its abundant twins and active twinning-induced dynamic recrystallization during the subsequent hot deformation. As shown in Figure 4.7, abundant twins, especially $(10\bar{1}2)$-$(01\bar{1}2)$ twin-twin interactions, are generated in the CT-deformed sample. The quantitative analysis of twinning behaviours in the cryogenic deformation will be conducted in Chapter 5, and the reason for the active twinning behaviours will also be explained in the next chapter.

The reasons for the high KAM values in twin-twin interactions are as follows. Firstly, as the twin propagation will be prevented by another twin variant in twin-twin interactions, the

structure of twin-twin interactions is generally fine. The fine structures can block the dislocation slips effectively and result in high KAM values, according to the boundary strengthening effects [107]. Secondly, the various orientations in the twin variants of twin-twin interactions provide many favourable paths for dislocation slips, and this can promote the dislocation accumulations further.

As the high KAM values in twin-twin interactions can provide sufficient stored energy to activate the recrystallization, the abundant twin boundaries in the CT-deformed sample can be regarded as the preferential recrystallization nucleation sites. In Figure 4.8, during the early stage of dynamic recrystallization, many new grains nucleate in the twin-twin interactions, and this results in significant grain refinement. The characteristics of the twin boundaries remain, indicating that the twin relationship is not changed by the dynamic recrystallization. The recrystallization around the twin-twin interactions could be attributed to the high activity of dislocation slips and the formation of subgrain boundaries in twin-twin interactions, which gradually transform into high angle grain boundaries (HAGBs) and form the recrystallized grains [12, 96]. As the orientations of recrystallized grains in these twin-twin interactions are various, it would contribute to forming the weak and scattered texture in the CT-HD sample. Therefore, twinning-induced dynamic recrystallization around twin-twin interactions plays an important role in achieving fine grains and the weak texture in the hot deformation process of the CT-HD sample.

4.4.2 Recrystallization in the direct-HD and RT-HD samples during hot deformation

The twin recrystallization is rarely observed in the direct-HD sample during the early stage of hot deformation, as shown in Figure 4.9. Almost no recrystallization is observed around the boundaries of TTWs and CTWs, and this phenomenon could be attributed to their coarse structures and the low KAM values near these twin boundaries. Unlike the twin-twin interactions with high KAM values near boundaries, the KAM values are generally low in most

areas of TTWs and CTWs and spread around these twins, which would result in difficulty accumulating enough dislocations to activate the recrystallization. Therefore, compared to TTWs and CTWs in the direct-HD samples, more active recrystallization behaviours in twin-twin interactions of the CT-HD sample could be attributed to its fine structures and high KAM values around twin boundaries, as these twin boundaries would provide abundant recrystallization sites, as shown in Figure 4.8 and Figure 4.9.

The recrystallization in the direct-hot deformed sample mainly occurs around the deformation bands including the deformed areas near the grain boundaries, as shown in Figure 4.9. This could be attributed to the narrow structure of deformation bands in which abundant dislocations accumulate to activate recrystallization. However, compared to abundant twin boundaries in the CT-HD sample, the density of deformation bands in the direct-HD sample is limited, resulting in a low recrystallized area fraction and inefficient grain refinement. Unlike twin recrystallization, the recrystallization near the deformation bands and grain boundaries generally contributes to texture strengthening in Mg alloy AZ31, and this could be attributed to its oriented basal grain growth [13, 82].

Regarding the RT-HD sample, its main recrystallization sites are also deformation bands including the areas near grain boundaries (Figure 4.10). However, after pre-deformation at RT, more dislocations accumulate in the RT-HD sample, which would provide more stored energy for recrystallization than that in the initial sample. As a result, the recrystallization in the RT-HD sample is much more active than that in the direct-HD sample. However, compared to the CT-HD sample, the less active recrystallization in the RT-HD sample could result from its fewer recrystallization sites near twin boundaries.

In this chapter, it is found that twin-twin interactions are the main recrystallization sites in the CT-HD sample, while deformation bands play an important role in the recrystallization of

direct-HD and RT-HD samples. However, the microstructure and texture evolution in these two recrystallization sites is still unclear. To address this question, the *quasi-in-situ* EBSD will be applied to study the microstructure evolution during the recrystallization in twin-twin interactions and deformation bands in Chapter 7.

4.4.3 Enhancement of ductility and strength in the hot-deformed sample with cryogenic pre-deformation

Compared to the direct-hot-deformed and initial sample, a significant improvement of ductility and strength was achieved in the hot-deformed samples with pre-deformation, particularly cryogenic deformation, because of the formation of finer grains and the weaker texture in these samples, as seen in Figure 4.4 and Figure 4.5. The strength of Mg alloy AZ31 generally increased with decreasing grain size, as suggested by the Hall-Petch hardening relationship [47, 48]. The high ductility of the hot-deformed sample with cryogenic pre-deformation could be due to the combination of fine grains and the weak texture. (i) The ductility of Mg alloys generally increases with decreasing grain size [10], due to the limited twins and enhanced non-basal slips in the fine-grained sample. Dislocation slips rather than twins generally dominate the deformation in the finer grain size [52], as grain boundaries have larger strengthening effects on twinning than dislocation slips [19]. The limited twins in the fine-grain sample can be beneficial to the high ductility, because the twins, such as $\{10\bar{1}1\}$-$\{10\bar{1}2\}$ double twins, are generally associated with fractures [31, 53, 54]. Besides, more grain boundaries in the fine-grained sample could suppress crack propagation, as it is difficult for cracks to propagate through grain boundaries [50]. (ii) Non-basal slips in a fine-grained Mg alloy AZ31 were activated near grain boundaries due to the additional shear stress to achieve compatibility between deformed grains, because only the basal slip systems cannot achieve the compatibility near grain boundaries [51]. Non-basal <c+a> slips were also observed in fine Mg crystal due to the high stress. This would accommodate the strain along the *c*-axis of the Mg crystal,

resulting in high ductility [9]. (iii) As shown in Figure 4.5, regarding the hot-deformed samples, the weakest texture was formed in the CT-HD sample, which would result in more grains with various orientations to readily activate slips [10, 116], thus improving the ductility.

4.5 Summary

In this chapter, hot compression tests were conducted for initial, RT-pre-deformed and CT-pre-deformed Mg alloy AZ31 to find a novel and effective method to enhance the mechanical properties and optimize the microstructure. The dynamic recrystallization around twinning and deformation bands was also investigated. The following conclusions were made:

(1) The mechanical properties of hot-deformed Mg alloys were significantly enhanced with pre-deformation, especially cryogenic deformation. The ductility and fracture strength of the hot-deformed sample with cryogenic pre-deformation (cryogenic-hot-deformed) increased by 110% and 27%, compared to the direct-hot-deformed sample.

(2) The effective grain refinement from 565 μm to 7 μm was achieved with the hot compression combined with the cryogenic pre-deformation. This cryogenic-hot-deformed sample also showed a homogenous microstructure and a weak texture of 10.03 mud, compared to a strong texture of 70.31 mud in the direct-hot-deformed sample.

(3) Abundant twins, especially twin-twin interactions, were generated during the cryogenic deformation. These twin-twin interactions with high KAM values in the CT-deformed sample provided abundant sites for active recrystallization during the hot compression, resulting in significant grain refinement and texture weakening.

(4) The main recrystallization sites in the direct-hot-deformed and RT-hot-deformed samples during the hot deformation were deformation bands with high KAM values,

while inactive recrystallization was observed near the TTWs with coarse structures due to their low KAM values.

This chapter demonstrates that it is feasible to apply the cryogenic-hot deformation method to refine the grains and weaken the texture, thus improving the ductility and strength of Mg alloy AZ31. However, the deformation mechanisms at room and cryogenic temperature and subsequent recrystallization mechanisms need further investigations. Therefore, the following chapters will focus on revealing these mechanisms. Chapter 5 demonstrates how twins and dislocations evolve during the cryogenic and room-temperature deformation, and their relationship with texture and strain hardening in compression tests. Chapter 6 shows the evolutions of twin-twin interactions, twinning sequence and deformation bands, and the relationship between these deformation structures with dislocations. Furthermore, Chapter 7 reveals the microstructure evolution and recrystallization mechanisms in twin-twin interactions and deformation bands using a *quasi-in-situ* EBSD method.

5 Deformation behaviour of Mg alloy AZ31 at cryogenic temperature

5.1 Introduction

The cryogenic-hot deformation method to refine the grains and weaken the texture in Mg alloy AZ31 was studied in Chapter 4, and the dynamic recrystallization mechanisms in the direct-HD, RT-HD and CT-HD samples were also investigated. More detailed research on the deformation behaviour at room and cryogenic temperatures (RT and CT) is necessary to understand the mechanisms involved in these deformation processes, as twins and dislocations play an important role in the deformation and recrystallization processes.

In this chapter, the deformation behaviour of Mg alloy AZ31 during the compression tests at CT and RT was studied to understand how twins and dislocations affect the flow stress and strain hardening. Cryogenic deformation suppresses the dislocation activities and enables the effects of dislocation slip and twinning on plasticity to be separately interrogated. A *quasi-in-situ* EBSD method was used to trace the evolution and distribution of twins and local misorientation, in the same group of grains before and after plastic deformation at RT and CT, respectively. Based on these results, the effects of temperature on twins and dislocations were studied. The effects of tension twins and twin-twin interactions on texture formation and dislocation distribution in the RT and CT deformation were also investigated.

5.2 Experimental programme

5.2.1 Material and experimental tests

In this study, the geometry of Mg alloy AZ31 samples for compression tests is a cuboid, with dimensions of 10 mm × 10 mm × 10 mm (details of the material are shown in Section 3.1). The cubic sample is used to conduct the *quasi-in-situ* EBSD, as its flat surface can be scanned with EBSD before and after deformation. The schematic of the experimental approach is illustrated in Figure 5.1. The CD, RD, and TD directions of the cube are defined as shown in Figure 5.1, which is used to define the directions on the following inverse pole figures and pole figures. In order to study the mechanical behaviour, some samples were compressed to failure with a nominal strain rate of 1 s^{-1} using an Instron 5584 machine at various temperatures (20 ℃, -60 ℃, -86 ℃, and -196 ℃). 20 ℃ was selected as room temperature. -196 ℃ was chosen, as it is the most common cryogenic temperature and easy to be achieved with liquid nitrogen. -60 ℃ and -86 ℃ were selected to study the deformation behaviours between 20 and -196 ℃. The strain rate was applied to make it closer to the high strain rate encountered in industrial thermomechanical processes [117]. Other samples were compressed at the same strain rate to a strain of about 0.08 at these temperatures, to observe the corresponding microstructure evolution.

An Instron attached environmental chamber was used with liquid nitrogen to cool down the samples in Figure 3.1. Three tests were repeated for each condition to ensure the reliability of the results. The strain was measured based on the displacement output of the machine, and the stress-strain curves were all corrected for compliance, because it is practically hard to measure the strain with an extensometer or digital image correlation in compression tests at such low temperatures. A commercial lubricant was applied in the compression tests to reduce the friction between the sample and the platens.

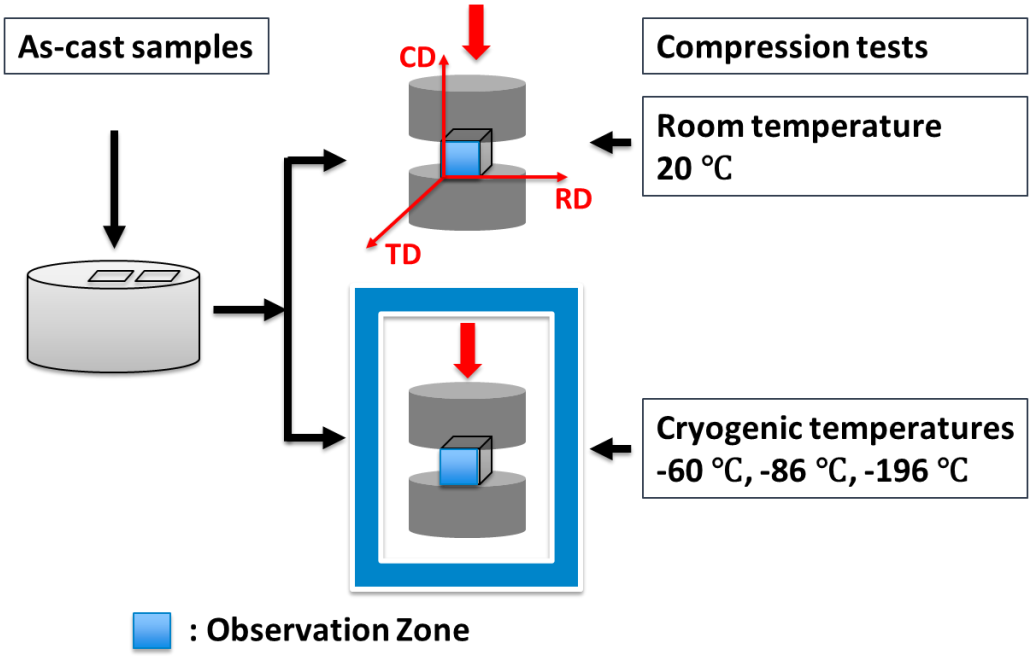

Figure 5.1 A schematic of the experimental compression procedure at room and cryogenic temperatures.

5.2.2 EBSD measurements

Prior to compression testing, samples were prepared for EBSD characterisation in a Hitachi 3400 SEM microscope (details are shown in Section 3.3.1). A 25 KeV electron beam was selected to map the 2500 µm × 1900 µm area. A step size of 8 µm was chosen to conduct the EBSD analysis. This relatively large step size was chosen to enable statistically representative regions of the microstructure to be captured in a reasonable time. As demonstrated later, for the strain and grain size used in this study, the twins are much thicker than this step size. To confirm that this step size does not lead to a miscounting of the twin fractions or interactions, maps were also produced with a step size of 3 µm, and the statistics from both were compared (Figure 5.2). As demonstrated in this figure, both step sizes give the same statistics regarding the area fraction of twins and interacting twins, within the error of the measurement. A finer step size of 0.5 µm was chosen to obtain the detailed information near twin boundaries. The corner of the sample was used as a reference point for the scanned area. Then, the same region of interest was relocated and scanned using the EBSD after compression testing with a strain

of 0.08. Texture analysis requires a large number of grains to be sampled. As the T4-treated as-cast Mg alloy AZ31 has a large grain size, EBSD maps with a size of 10 mm × 10 mm were captured using TESCAN MIRA3 FEG-SEM equipped with an Oxford Symmetry EBSD detector.

The HKL CHANNEL 5 software was applied to analyse the EBSD data. The twin boundaries were highlighted according to their specific misorientation around the axis. The image with identified twin boundaries was then imported into the image processing package ImageJ, and the area formed by these twin boundaries was calculated and divided by the total area of the image. This value was used to represent the area fraction of twinning. The area fraction of interacting twins was calculated from the area of the twin variants which form twin-twin interactions, divided by the overall area of the image, and the inset in Figure 5.2 shows the schematic figure of the interacting twins between twin variants T1 and T2. As the calculation of the twinned area fraction is based on the analysis of exactly the same region of interest, it properly accounts for the effect of twins that have engulfed the entire grains (so that no twin boundaries are presented inside the twinned grain). Such grains make an essential contribution to the overall twinned area fraction but would be usually missed in a conventional analysis where only the post-deformation microstructure is studied.

The fraction of interacting twins was calculated from the number of twin-twin interactions divided by the total number of twins in the image. Each data was measured four times, and the average values with uncertainties were presented. The measured twin thickness was estimated as the minor axis of an ellipse fitted to the twins, and the true twin thickness was corrected by multiplying the cosine of the angle between the twin plane and the normal to the sample [118].

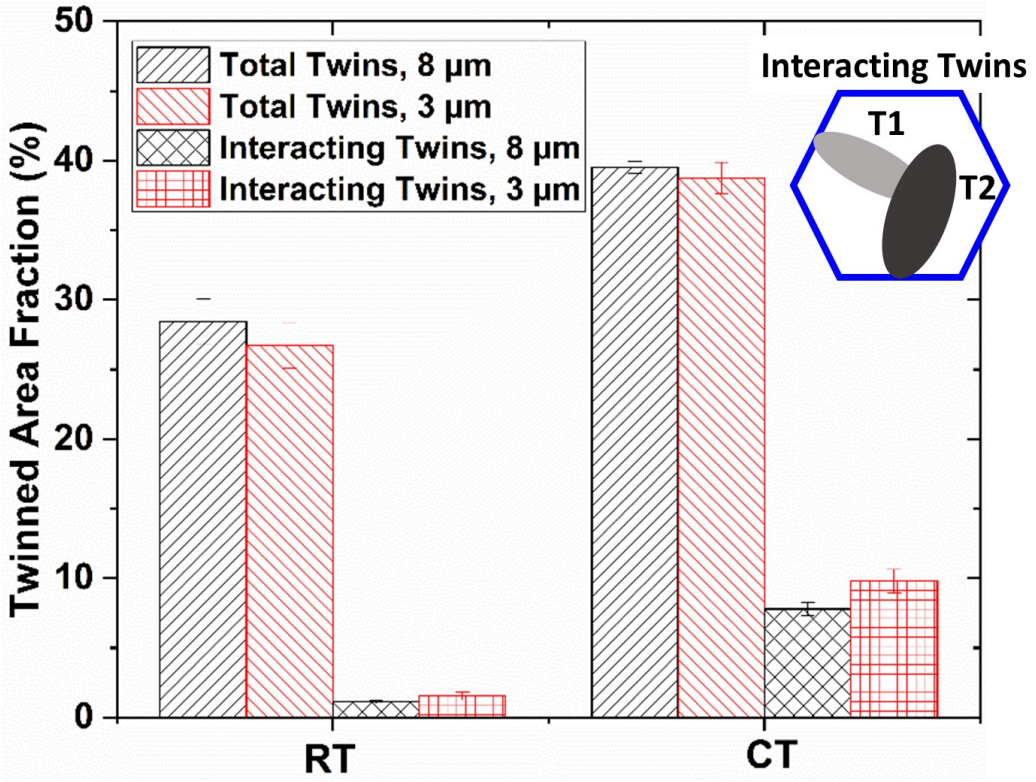

Figure 5.2 Total twinned area fraction and area fraction of (10$\bar{1}$2)-(01$\bar{1}$2) interacting twins with a step size of 3 µm and 8 µm, respectively. Similar results are obtained for both step sizes.

5.3 Results

5.3.1 Mechanical behaviours of Mg alloy AZ31 at room and cryogenic temperature

The true stress-strain curves are presented in Figure 5.3 (a), showing a significant increase in flow stress and a mild decrease in strain to failure with decreasing temperature from 20 °C to -196 °C. The estimated yield strength for the as-cast Mg alloy AZ31 at room temperature (20 °C) is only ~ 60 MPa, which is in agreement with the literature [119]. The stress-strain curve at cryogenic temperature (-196 °C) is almost linear, which indicates a significantly high strain hardening rate during the plastic deformation. As shown in Figure 5.3 (b), a considerable increase in the strain hardening rate is observed as the temperature is reduced from 20 °C to -196 °C. The drop in true stress recorded towards the end of the curves in Figure 5.3 (a) is associated with the onset of fracture.

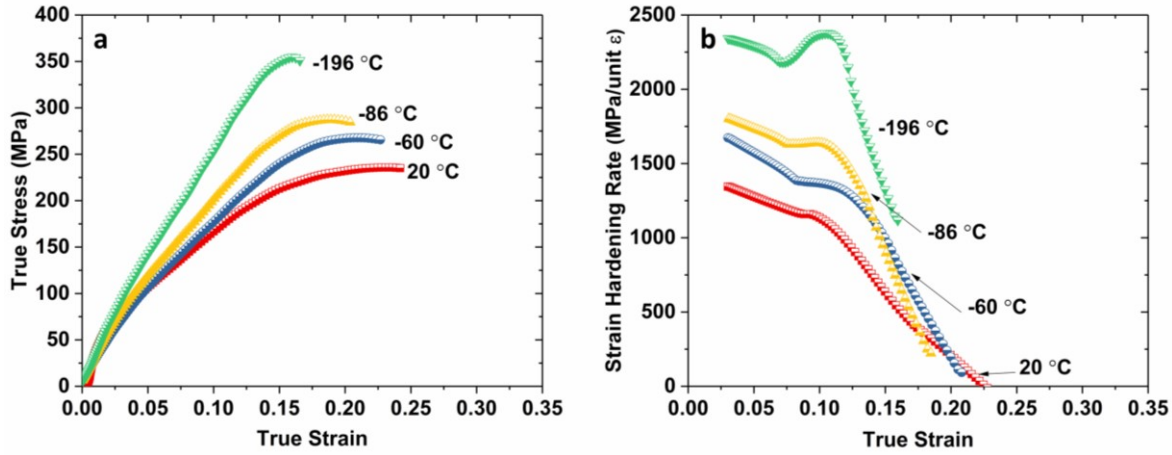

Figure 5.3 (a) The true stress-strain compression curves of Mg alloy AZ31 at various temperatures, and (b) the calculated strain hardening rate variation as a function of true strain based on (a).

5.3.2 Microstructure evolution of Mg alloy AZ31 at room and cryogenic temperature

The microstructure evolution in the same regions of interest before and after deformation at room and cryogenic temperatures can be seen in Figure 5.4. Figure 5.4 (a-b) plots the initially T4-treated microstructure (IPF colouring) in two samples. These IPF maps show the initial microstructure and highlight the lack of significant twins in the T4-treated undeformed samples. The small number of fine twins in the T4-treated microstructure were probably introduced during the grinding and polishing process, and were difficult to avoid in the material with this large grain size. The analysis of the same regions after deformation enabled the small contribution from these twins to be accounted for.

Figure 5.4 (c-d) illustrates how the microstructure in Figure 5.4 (a-b) developed after 0.08 plastic compressive strain at 20 ℃ and -196 ℃, which represents deformation at room and cryogenic temperature, respectively. It is clear that in all samples, a large volume fraction of twins was generated after plastic deformation. This result is consistent with the result observed by neutron diffraction, where the twinned area fraction observed at a strain of 0.05 was ~ 15% at 20 ℃ [86]. This also indicates that the twinned area fraction at a strain of 0.08 would be higher than ~ 15%, and it was within the plastic deformation region.

As the exact regions of interest are traced before and after plastic deformation, it is possible to identify the grains that have undergone a complete reorientation due to twinning, where the twin boundaries are no longer visible. These grains are completely or almost completely consumed and occupied by the newly formed twins. A reliable estimate of the twinned area fraction requires capturing these fully twinned grains, which is only possible by mapping the same region prior to deformation. Relying only on the as-deformed EBSD maps and determining the twinned fraction from the twin boundaries visible within partly twinned grains gives a large underestimate of the true twinned fraction. For example, the twinned area fraction ignoring fully twinned grains (in the RT-deformed sample) is about 14% which is only half that of the true twinned area fraction, measured as approximately 28%.

A few grains (A, B, C, D, E) are selected and highlighted as examples of twin-induced grain reorientation, such as grain B in the RT-deformed sample and grain C in the CT-deformed sample in Figure 5.4, Figure 5.6 and Figure 5.7. However, unlike grain B in the RT-deformed sample which has only a single twin variant (Figure 5.4 and Figure 5.6), grain C (deformed at CT) shows a number of different twin variants (Figure 5.4 and Figure 5.7). This difference could be attributed to the change in the activation stress for twinning and dislocation slip as a function of temperature [19].

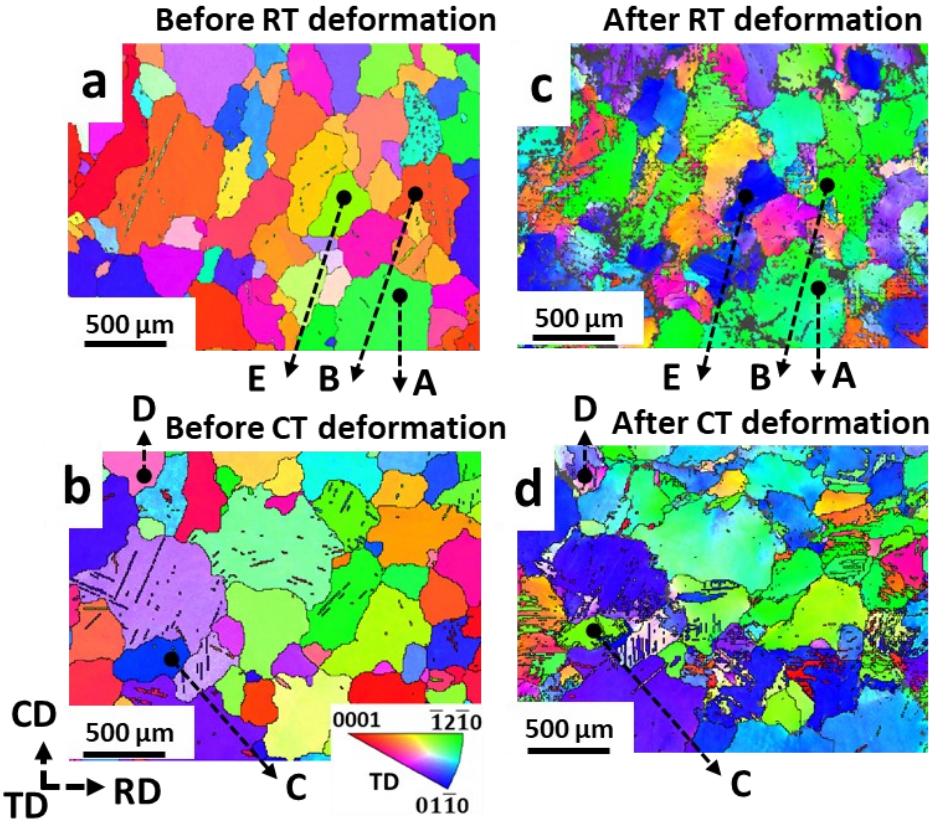

Figure 5.4 EBSD IPF maps of (a, b) two T4-treated Mg alloy AZ31 samples, and deformed samples after compression tests with a strain of 0.08 at (c) room temperature and (d) cryogenic temperature, respectively. Maps (a) and (c) and maps (b) and (d) are recorded in the same region of interest, before and after deformation. Observation along TD is applied to the IPF triangle. Label A-E highlight individual grains (see text for details).

The main twinning modes in these deformed samples are identified as the $\{10\bar{1}2\}$ TTWs and $(10\bar{1}2)$-$(01\bar{1}2)$ twin-twin interactions. TTWs can be identified by the reorientation of the *c*-axis by ~ 86° about an $<11\bar{2}0>$ axis [26]. $(10\bar{1}2)$-$(01\bar{1}2)$ twin-twin interactions exhibit a characteristic misorientation angle of ~ 60° about an $<10\bar{1}0>$ axis, and the misorientation relationship occurs between twins that form on the $(10\bar{1}2)$ and $(01\bar{1}2)$ planes [41]. The total twinned area fraction, area fraction and fraction of the $(10\bar{1}2)$-$(01\bar{1}2)$ interacting twins are summarised and plotted in Figure 5.5 (a).

The twinned area fraction is the lowest at ~ 28% for the deformed samples at 20 °C. As the temperature decreases to -86 °C, the twinned area fraction shows an increasing trend to ~ 43%, and then remains constant (within the error of the measurements) until -196 °C, indicating a

saturation of the twinned area fraction. These results are consistent with the twinned area fraction measured by neutron diffraction previously, where it was found that the twinned area fraction was ~ 30% for a strain of 0.10 at room temperature and a higher twinned area fraction was also observed at -196 °C [86]. In addition, the area fraction of the $(10\bar{1}2)$-$(01\bar{1}2)$ interacting twins in the RT-deformed sample is low. This result demonstrates that the main twinning mode in the RT-deformed sample is $\{10\bar{1}2\}$ TTW, which generally forms a single variant within grains. There is a sharp increase in the area fraction of interacting twins when the temperature decreases from 20 °C to -196 °C, which is also reflected in the increasing number fraction of interacting twins, increasing from 12% at 20 °C to 42% at -196 °C. At cryogenic temperatures more variants form in a single grain, leading to a greater number and area fraction of twin-twin interactions. This trend of twin variants is consistent with the results reported in Ref [120], where it was found that more twins nucleated in Mg-3Al-1Zn alloy with decreasing temperature from 200 ℃ to 25 ℃.

The higher density of $(10\bar{1}2)$-$(01\bar{1}2)$ twin-twin interactions in the CT-deformed samples may contribute to the increase of the strain hardening rate (Figure 5.3 (b)). As shown in Figure 5.4, Figure 5.6 and Figure 5.7, compared to most $\{10\bar{1}2\}$ TTWs, twin-twin interactions result in the denser distribution of narrower twins. These twin-twin interactions divide the grains into smaller blocks and result in a twinning-induced grain refinement, which is expected to provide the additional Hall-Petch strengthening [65].

Figure 5.5 (b) shows the $\{0001\}$ and $\{10\bar{1}0\}$ pole figures for the T4-treated AZ31 samples compressed to a strain of 0.08 at room temperature (20 °C, RT) and cryogenic temperature (-196 °C, CT). There is a typical basal fibre texture generated in the RT-deformed sample [121], which mainly concentrates in the centre of the $\{0001\}$ pole figure. However, when the sample

is compressed at CT, the texture becomes weaker, and the maxima are slightly tilted away from the compression direction toward the RD.

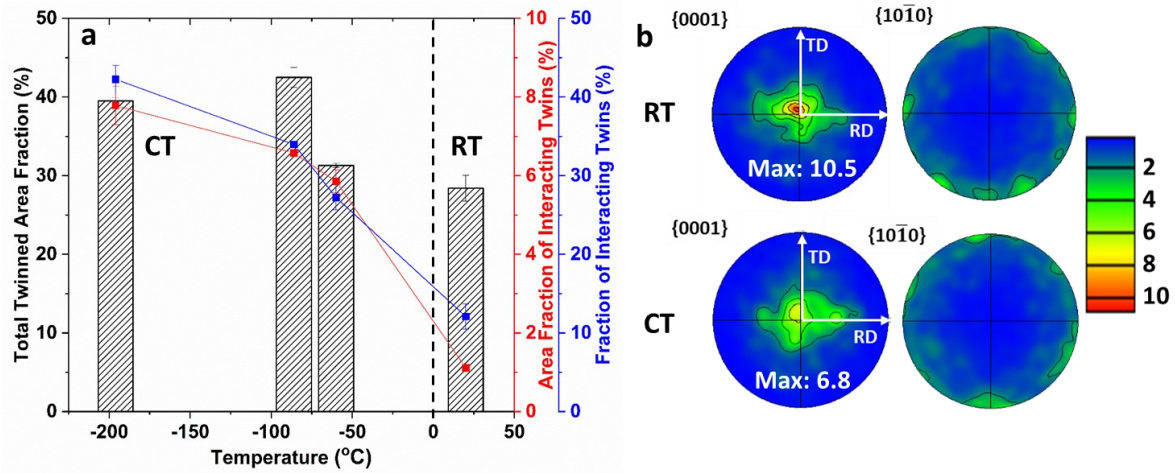

Figure 5.5 (a) Twinned area fraction, area fraction and fraction of (10$\bar{1}$2)-(01$\bar{1}$2) interacting twins in deformed samples after compression tests with a strain of 0.08 from room temperature (RT) to cryogenic temperature (CT), and (b) the corresponding {0001} and {10$\bar{1}$0} pole figures, the unit of the colour bar is in multiples of a uniform distribution (mud).

5.3.3 Twinning behaviour of Mg alloy AZ31 at room and cryogenic temperature

The detailed analyses on single grains are conducted for the RT-deformed and CT-deformed samples to study the twinning behaviours. Figure 5.6 (a, b) shows the initial and RT-deformed grain A. According to the pole figures in Figure 5.6 (e, f), the *c*-axis of the initial grain A is almost parallel to the compression direction (CD), and its orientation does not change much, which is expected because this grain is unfavourably oriented for deformation by either TTW or basal slip. Therefore, grain A can be identified as hard grain. Grain A contains some streaks of pixels, which are identified as the {10$\bar{1}$1}-{10$\bar{1}$2} double twins, according to the specific misorientation and axis of the twin boundaries, namely 38° <11$\bar{2}$0>. This is expected for the *c*-axis compression experienced by this grain [41].

In contrast, grain B is favourably oriented for TTW formation, and almost all of this grain is twinned, as shown in Figure 5.6 (c, d). Only a very small portion towards the top of the grain

retains the original matrix orientation, with a sharp boundary between the regions that correspond to a TTW boundary. In these figures, AM1 and BM1 refer to the matrix, and B2 refers to the specific $\{10\bar{1}2\}$ TTW variant observed. As shown in Figure 5.6 (g), the *c*-axis of initial grain B is almost normal to the CD. After the compression test, most of this grain is rotated by TTW towards the CD, and its orientation is similar to that of grain A (Figure 5.6 (f, h)). As grain B is easier to be deformed and different from grain A, grain B can be identified as soft grain.

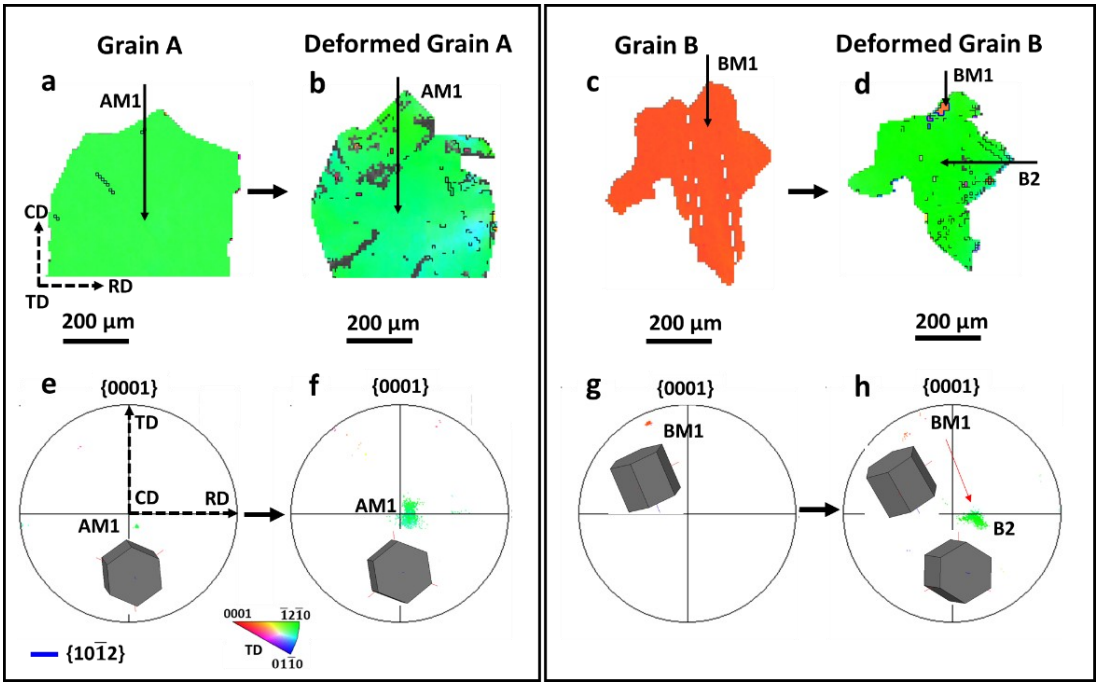

Figure 5.6 Typical grain evolution of Mg alloy AZ31 in compression tests to a strain of 0.08 at room temperature. (a, b) EBSD IPF maps, (e, f) corresponding {0001} pole figures of initial and deformed grain A, respectively. (c, d) EBSD IPF maps, (g, h) corresponding {0001} pole figures of initial and deformed grain B, respectively. The IPF key shows the colour scheme used in this figure. Observation along TD is applied to the IPF triangle.

According to Figure 5.7 (a, b), $\{10\bar{1}2\}$ TTWs and $(10\bar{1}2)$-$(01\bar{1}2)$ twin-twin interactions are both activated in grain C after compression tests at cryogenic temperature. In Figure 5.7 (a, e), the *c*-axis of initial grain C is almost parallel to the RD direction. After the compression test, a tension twin variant C2 is activated from the matrix CM1, with a lattice rotation of ~86º.

However, unlike grain B at room temperature, another tension twin variant C3 is generated on another $\{10\bar{1}2\}$ plane within the matrix, and meets with the tension twin variant C2 to form a $(10\bar{1}2)$-$(01\bar{1}2)$ twin-twin interaction.

The orientation of grain D (Figure 5.7 (c, g)) behaves differently from that of grain C (Figure 5.7 (a, e)). Most of the matrix in the deformed grain D is occupied by twins that are interacted, which is similar in structure to that observed in grain C. The two twin variants D2 and D3 undergo the same large reorientation of the basal pole in the grain D, and they are distributed in the two sides of pole figures along the TD direction and do not concentrate in the centre of the pole figure. A similar distribution is observed in the pole figure of grain C (Figure 5.7 (f)). This confirms that the twin-twin interactions, as seen in grain C and grain D, can produce a spread in texture around the basal pole and contribute to the texture weakening, which is observed in Figure 5.5 (b).

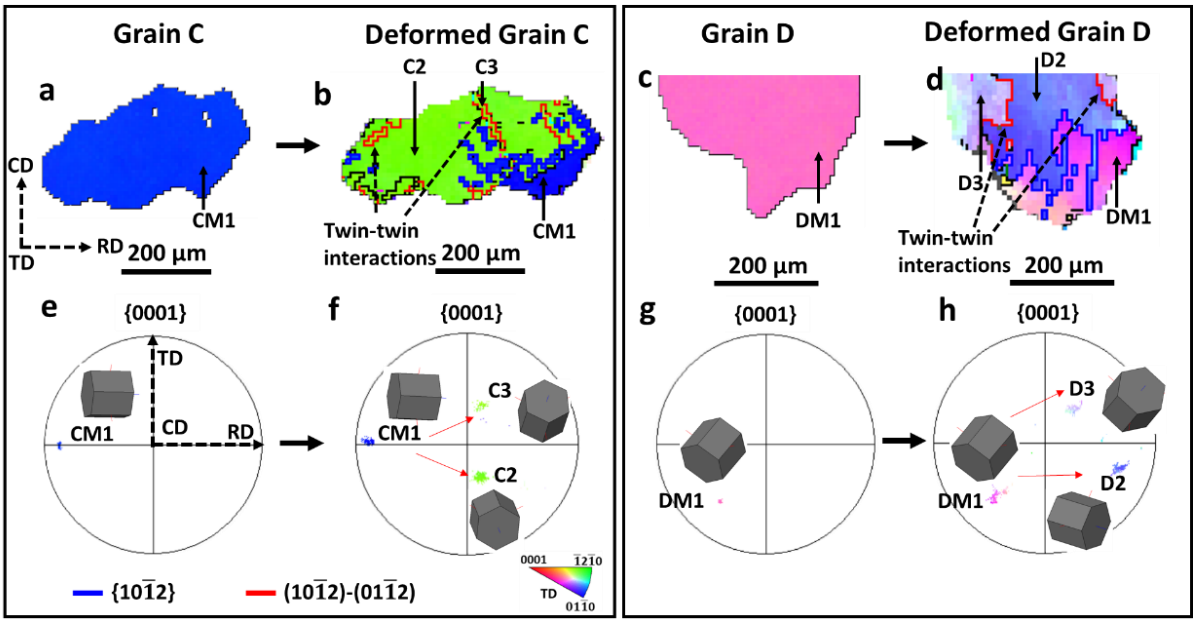

Figure 5.7 Typical grains evolution of Mg alloy AZ31 in compression tests to a strain of 0.08 at cryogenic temperature. (a, b) EBSD IPF maps, (e, f) corresponding {0001} pole figures of initial and deformed grain C, respectively. (c, d) EBSD IPF maps, (g, h) corresponding {0001} pole figures of initial and deformed grain D, respectively. The IPF key shows the colour scheme used in this figure. Observation along TD is applied to the IPF triangle.

5.3.4 Twinning and KAM behaviours of Mg alloy AZ31 at room and cryogenic temperature

In this section, detailed analyses of single grains are carried out to study their relationship between twinning behaviours and dislocations (via KAM). The EBSD maps are obtained with a finer step size of 0.5 μm. As shown in Figure 5.8 (a-c), the grain E is consumed by twins after compression testing at room temperature. The KAM maps imply a strongly heterogeneous distribution of dislocations after deformation in grain E. In general, the KAM value is low in most areas, particularly towards the grain interior, while it is higher towards the grain boundaries. Within the grain interior, there are few regions of relatively high KAM values in grain E. This implies that grain E has stored the low content of dislocations after twinning. Figure 5.8 (d-g) plots the twin activities and KAM maps in the typical grain C after compression testing at cryogenic temperature. The interactions of these two twin variants C2 and C3 divide the grain into smaller units and show fine structures, as seen in Figure 5.8 (e). Some twin-twin interactions are highlighted with the yellow box in Figure 5.8 (f) and (g). The analysis shows that the KAM value is very high near the boundaries of $(10\bar{1}2)$-$(01\bar{1}2)$ twin-twin interactions, indicating that the twin-twin interactions are the preferential sites for dislocation accumulations and their boundaries are effective dislocation barriers. It is also expected that the high dislocation density near twin-twin interactions would contribute to the high hardening rate and flow stress at cryogenic temperature.

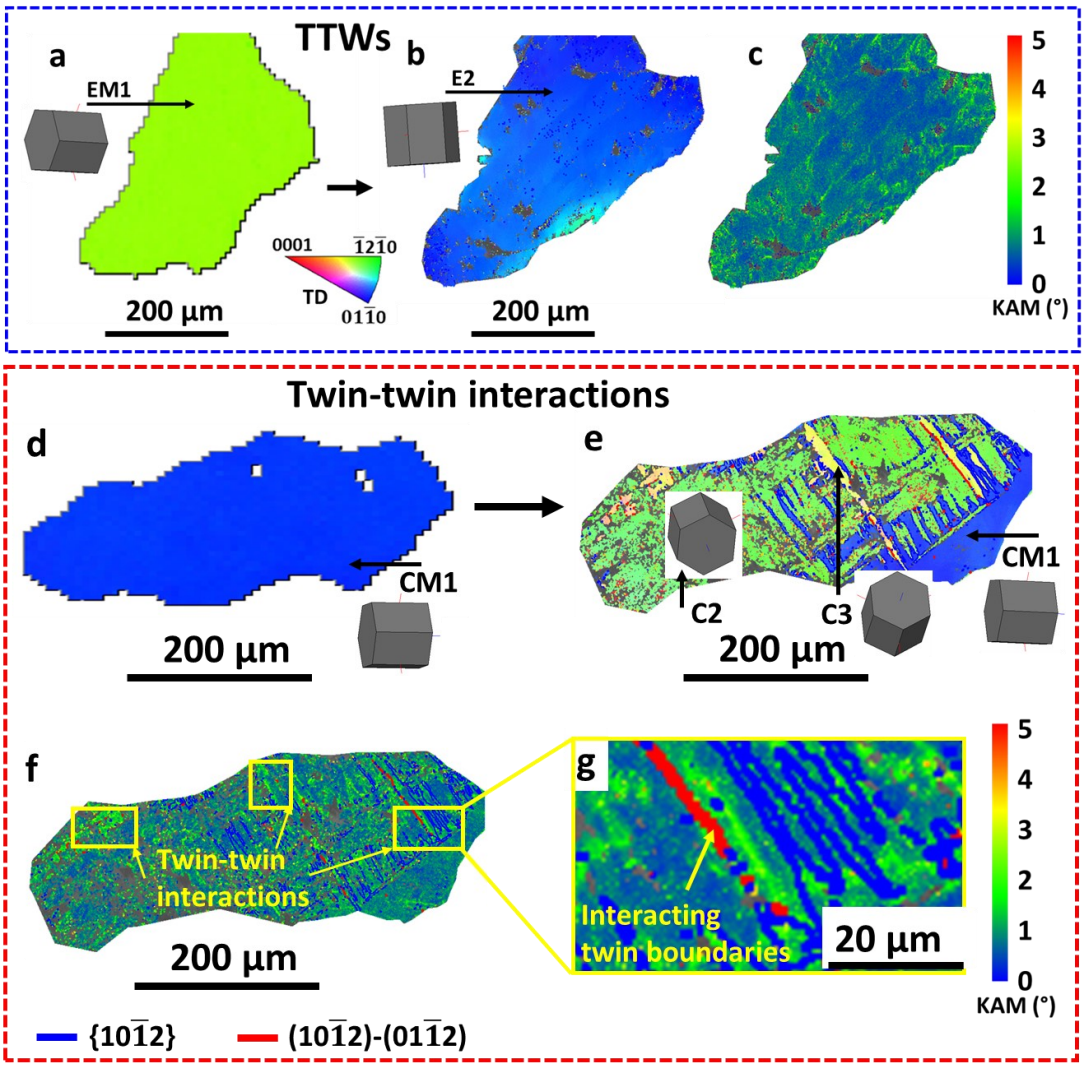

Figure 5.8 EBSD IPF maps of (a) initial and (b) RT-deformed grain E in compression tests at a strain of 0.08, and corresponding (c) KAM map in RT-deformed grain E, respectively. EBSD IPF maps of (d) initial and (e) CT-deformed grain C in compression tests at a strain of 0.08, and corresponding (f) KAM map and (g) enlarged map in CT-deformed grain C, respectively.

Figure 5.9 plots the statistical analysis of the KAM distribution of the sample deformed at various temperatures. The KAM distribution for the sample compressed at 20 °C is slightly skewed towards the higher values, indicating a slight increase in the stored geometrically necessary dislocation density overall. The increase in average KAM value is calculated from the average KAM value of the deformed samples minus that of the initial sample, and the increase in average KAM value for all deformed samples is presented in Figure 5.9 (b). The highest increase in KAM value is seen in the sample deformed at 20 °C. The increase in average

KAM value is smaller at a lower testing temperature and falls from 20 °C to -196 °C. This is consistent with an increased role of twinning and a decreased role of dislocation slip in accommodating deformation as the temperature is reduced.

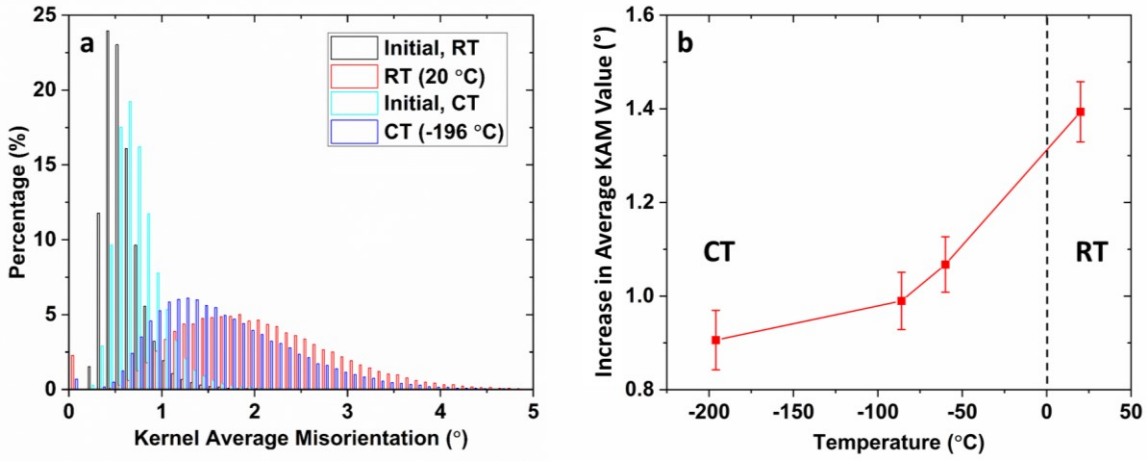

Figure 5.9 (a) The histograms of KAM distribution of two initial Mg alloy AZ31 samples and samples compressed to a strain of 0.08 at room temperature (RT, 20 °C) and cryogenic temperature (CT, -196 °C), (b) increase in average KAM value of samples compressed to a strain of 0.08 at room and cryogenic temperatures.

5.4 Discussion

Figure 5.10 illustrates the twinning and dislocation behaviour at RT and CT observed in this work schematically. Higher KAM values and fewer twins, mainly $\{10\bar{1}2\}$ TTWs, are found at RT, whereas the CT-deformed sample shows lower KAM values and more twins, which lead to a greater number of twin-twin interactions. The total area fraction of twins is also increased at CT compared to RT, and this is consistent with previous studies of deformation at CT [86, 87].

The high activity of twinning and twin-twin interactions would be attributed to limited dislocation slips and significant local stress concentrations in the cryogenic deformation. (i) Twinning and dislocation slips are the two main deformation modes in Mg alloys at low temperature. It is well-known that the CRSS for twinning is almost insensitive to the temperature, but the CRSS for dislocation slip increases with decreasing temperature [19, 83].

As temperature decreases to cryogenic temperature, it is difficult to activate dislocation slips due to their higher CRSS, resulting in the high density of twins to accommodate the plastic strain [19]. (ii) The limited dislocation slips could result in local stress concentrations near grain boundaries, since insufficient dislocation slips are activated to relieve the strain misfit between neighbour grains and cause low deformation compatibility [73]. The significant local stress concentration near the grain boundaries would promote the twin nucleation because twin nucleation generally requires the local stress concentration [122, 123]. The high activity of twin nucleation results in abundant twin variants, which would interact to form abundant twin-twin interactions [41, 64]. The high activity of twins could also be related to the shear related mechanisms of twins. With decreasing temperature, dislocation could be suppressed due to the restricted atomic diffusion, while twin activities could not be suppressed, as the shear related twins are generally insensitive to temperature [45]. Therefore, more twins were generated at cryogenic temperature to accommodate the plastic deformation.

Importantly, CT deformation leads to smaller twins and more twin variants in a single grain. The balance between the thickness and number of twins depends on the balance between twin nucleation and twin growth (thickening). If twin nucleation is promoted with respect to growth, then more twins will form, but for a fixed volume fraction of twinning, they will grow to a smaller thickness (on average). Twin nucleation is activated by local stress concentrations in the grain boundary region. At CT, dislocation slip could be suppressed [19], and this probably enables higher stress concentrations to develop in local regions at the grain boundaries. This will promote twin nucleation and also enable multiple twin variants to nucleate in quick succession before the stress in the grain is relaxed by twin growth. As twinning is generally active at a high strain rate [19], this behaviour could also be related to the relatively high strain rate used in this study (1 s^{-1}), which is more typical of industrial processing strain rates compared to the typically lower test rates (10^{-2} – 10^{-3} s^{-1}) used in previous studies [124, 125].

As discussed in detail elsewhere [61, 64], once a twin becomes blocked, it becomes harder for this twin to propagate and thicken. This promotes further twin nucleation in the grains since twin propagation and growth are suppressed. Therefore, many multiple twin variants form [64], which can subdivide the grain into small units.

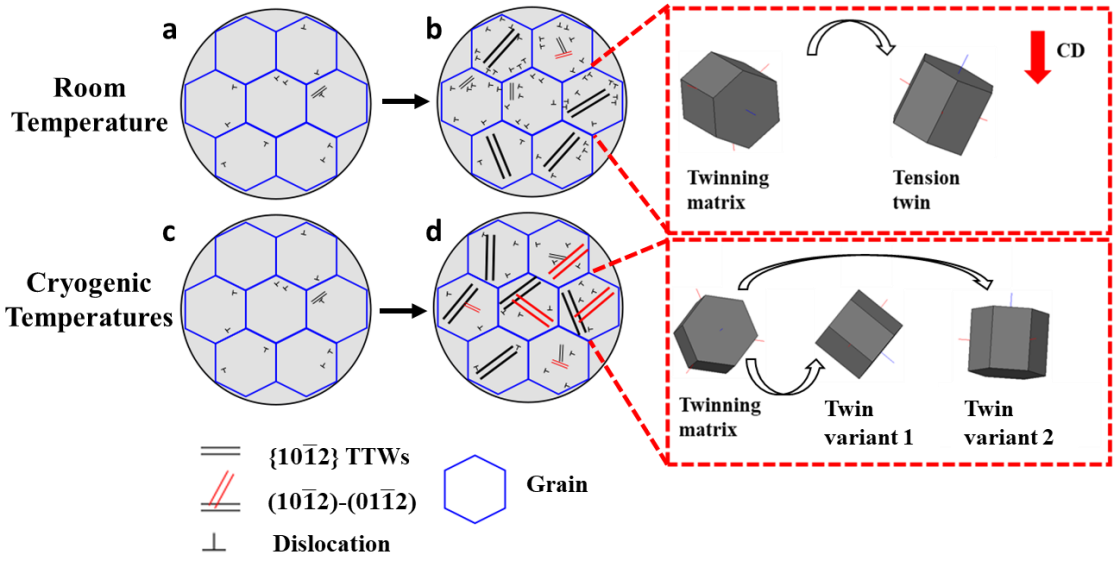

Figure 5.10 Schematic of twins and dislocation evolution in Mg alloys (a, c) at the initial state, and after deformation (b) at room temperature and (d) cryogenic temperatures with corresponding twinning behaviours, respectively.

An important observation in this work is that the strain hardening rate is much greater at CT than at RT. This leads to almost linear hardening and the higher flow stress at CT than at RT. This was also observed in previous studies comparing the deformation behaviour of a Mg alloy at CT and RT [86, 87]. In the previous work [86], the effect of CT deformation was accounted for by adjusting the CRSS and hardening rate values for slip and twinning, to enable good agreement between the measurements and the stress-strain response predicted by a VPSC model. This was shown to work well for slip dominated cases, but not for cases where deformation was twinning dominated. The increased hardening at CT deformation in the slip dominated cases was justified on the basis of reduced dynamic recovery, as dynamic recovery is a softening mechanism and reduces the dislocation density during deformation [86]. The

present study suggests that an important, and most probably dominant, contribution to the higher hardening rate at CT results from an increased incidence of multiple twin variants and therefore more twin-twin interactions. This effect is not accounted for in the VPSC model. As discussed in detail elsewhere [61, 64], interacting twins lead to a greater hardening rate by inhibiting the twin growth and inhibiting slip within twinned grains. The inhibition to slip arises from a resultant Hall-Petch effect, since the interacting twin boundaries subdivide the grains into smaller units. An estimate of this effect can be made through the Hall-Petch relationship [126]:

$$\sigma = \sigma_0 + kD^{-\frac{1}{2}} \tag{5}$$

Where σ is the flow strength, σ_0 is the friction stress, k is the stress intensity constant which is 0.7 MPa/m$^{1/2}$ in Mg alloy AZ31 [126, 127], and D is the mean twinning spacing. The mean twinning spacing can be calculated as [128]:

$$D = 2t\frac{1-f}{f} \tag{6}$$

Where t is the average twin thickness which is independent of strain, and f is the twinned area fraction. The average twin thickness t in the RT-deformed and CT-deformed samples is estimated to be approximately 334 μm and 69 μm, respectively. Therefore, the difference in twinning-induced strength $\Delta\sigma$ is estimated to be about 31 MPa. This suggests that a significant contribution to the measured flow stress difference at CT and RT (which is about 100 MPa at its greatest) may be attributed to the Hall-Petch strengthening effect against slip in grains twinned with multiple variants. The remainder of the strength difference is likely to come from the reduced dynamic recovery (as postulated by Jain et al. [86]) and the direct effect that twin-twin interactions have on the hardening against twinning [61, 64].

As shown in Figure 5.8, the high KAM value is high near twin boundaries, especially the boundaries of twin-twin interactions (Figure 5.8 (g)). This can be attributed to the Hall-Petch mechanism of twins, as twin boundaries act as the barrier to the dislocation movement [125, 129]. Twin-twin interactions contribute to the formation of fine structures and boundary dislocations near twin-twin boundaries, because twin propagation will be prevented by other twin boundaries, and twins hardly transmit across the twin boundary [61, 63]. These twin-twin interactions result in significant twinning-induced grain refinement, so the dislocation pile-up at the boundaries demonstrates the effective twin boundary hardening effect [107].

The high KAM values near the twin-twin interactions in the CT-deformed sample would provide high stored energy to activate recrystallization in the subsequent hot deformation process in Chapter 4 (Figure 4.8). More twin-twin interactions in the CT-deformed sample would provide more recrystallization nucleation sites, resulting in more active recrystallization in the CT-HD sample in Chapter 4. In addition, as shown in Figure 5.5 (b), a weaker texture was formed in the CT-deformed sample than that in the RT-deformed sample. This would be attributed to the various orientations of twin-twin interactions (Figure 5.7), while the coarse tension twins almost consume the whole grains in the RT-deformed sample and result in the formation of the strong basal texture. The weak texture in the CT-deformed sample could also contribute to the formation of the weak texture in the CT-HD sample during the hot deformation process (Chapter 4), because recrystallized grains near twins generally inherit the orientations of twin variants [96]. In addition, as the main twinning in RT-deformation is coarse tension twins, and recrystallization rarely occurs in the tension twins, it is reasonable that almost no recrystallization near twin boundaries are observed in the RT-HD sample in Chapter 4.

According to the reduced KAM values at lower temperatures (Figure 5.9), the dislocation density is higher in RT-deformation than in CT-deformation. This indicates that the strain

hardening effect induced by the dislocation density is more dominant at room temperature than at cryogenic temperatures. Therefore, the dislocation density hardening appears to be a minor contribution to the higher strain hardening rate at cryogenic temperatures, compared to the Hall-Petch strengthening effect resulting from twins and the direct hardening effects of twin-twin interactions against twinning. As the strain hardening is higher at cryogenic temperatures than at room temperature, these results indicate that twin boundary hardening could be more effective than dislocation density hardening. In addition, with decreasing temperature, a fine and homogeneous second phase could be precipitated from the matrix phase [130]. The second phase would act as barriers to dislocation slips, but this precipitate hardening effect of the second phase is less significant in Mg alloys [130], compared to the effects of twinning behaviours.

5.5 Summary

In this chapter, the deformation behaviour in Mg alloy AZ31 was studied using uniaxial compression tests at room and cryogenic temperatures to understand the twins and dislocations effects on the plasticity behaviour. A *quasi-in-situ* EBSD method was used to characterise the twinning and local misorientation evolution in the same group of grains before and after compression. The following conclusions can be drawn:

(1) The strain hardening rate is significantly higher at cryogenic temperatures than at room temperature. This higher hardening rate at cryogenic temperature is mainly attributed to the hardening induced by twin boundaries and twin-twin interactions, as twin boundaries can result in the Hall-Petch strengthening effect against slip and direct hardening effects of twin-twin interactions against twinning.

(2) More twins and lower average KAM values are observed in the cryogenically deformed samples than room-temperature deformed samples. This suggests that the twin boundary hardening could be considerably more effective than the stored dislocation density hardening.

(3) The appearance of more twin variants within the grains during the cryogenic deformation is found to lead to the formation of more twin-twin interactions and finer twins. The KAM value is high near twin boundaries, especially the boundaries of twin-twin interactions in the cryogenically deformed sample, which would be due to the boundary hardening effect.

(4) The high activity of twins and twin-twin interactions in the cryogenic deformation could be attributed to the limited dislocation slips and significant local stress.

(5) The mechanism reveals that more twin-twin interactions at cryogenic temperature result in new orientations to form a weak texture, while a stronger basal texture is formed at room temperature as the tension twin will consume the entire grain and transform the initial grain into a basal orientation.

6 Microstructure evolution during the cryogenic rolling process

6.1 Introduction

Deformation mechanisms including twinning and dislocations in uniaxial compression tests at room and cryogenic temperatures were studied in Chapter 5. It was found that more twins, particularly twin-twin interactions, were observed to accommodate plastic deformation at cryogenic temperature (CT) due to the limited dislocation slips and significant local stress concentration. However, the twinning sequence, another important twinning mode to accommodate the plastic deformation, was not studied in the previous chapter. It is worth exploring how the twinning sequence evolves at CT and its relationship with twin-twin interactions and dislocations. Furthermore, deformation bands, the main deformation structure at room temperature (RT), were not investigated in the previous chapter. It is essential to investigate how deformation bands evolve at RT and their relationship with dislocations and twins.

Rolling tests can be an effective way to trigger twin-twin interactions, twinning sequence (at CT) and deformation bands (at RT), due to the inhomogeneous deformation and multiaxial stress states induced by the rolling process [131]. In this chapter, to address these remaining questions of deformation behaviours, rolling tests at CT with various thickness reductions were conducted for Mg alloy AZ31 to study evolutions of tension twins, twin-twin interactions and twinning sequence. Rolling tests at RT with the corresponding thickness reductions were conducted to study the evolution of deformation bands and their relationship with twins. The interactions of these deformation structures with GND density manifested as KAM values were also systematically investigated.

6.2 Experimental programme

6.2.1 Materials and experimental tests

The material used in this chapter is an as-cast Mg alloy AZ31. The detailed information of this Mg alloy AZ31 is shown in Section 3.1. A schematic illustration of the RT-rolling and CT-rolling process is given in Figure 6.1. Rectangular samples with a thickness, width and length of 3, 8 and 25 mm were manufactured from the as-received Mg alloy AZ31. These samples were rolled at a moderate rolling speed of ~ 5 m/min to achieve a total thickness reduction (TR) of 3%, 9% and 13%, respectively. As the maximum TR is about 13% before cracking, the 13% was chosen, and 3% and 9% were chosen to show the microstructure evolution with the strain increasing. For the CT-rolling process, the samples were immersed in liquid nitrogen to ensure the entire sample reached the target liquid nitrogen temperature (cryogenic temperature) before each rolling. Then, the immersed samples were rapidly transferred to the rolling mill machine to achieve the designed TR. The temperature of immersed samples could change when the samples were transferred from liquid nitrogen immersion container to the roller, while the change should not be significant due to the rapid transfer. In addition, according to the microstructure results, the difference of microstructures between room and cryogenic temperature is significant, and conclusions are not affected.

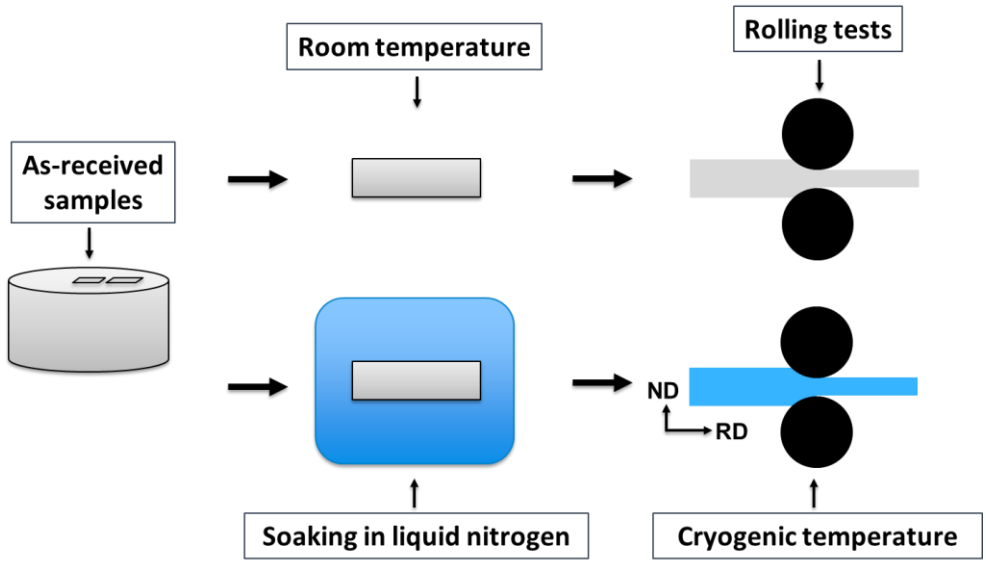

Figure 6.1 Schematic diagram of the experimental rolling processes at room and cryogenic temperature.

6.2.2 Microstructure characterisation

The rolled samples with the surface of RD × ND were prepared for microscopic examination. The rolled samples preparation, etching and optical microscopy observation processes were conducted to obtain large microstructure maps with respect to various deformation levels and temperatures (details are shown in Section 3.3.2).

EBSD observation was conducted to thoroughly examine the crystallographic morphology, identify the twinning types and misorientation distributions, and reveal the evolved deformation structures. A 2 μm step size was used to examine the detailed microstructures in the rolled samples. The obtained EBSD data were analysed to study twin boundaries and KAM maps using the HKL CHANNEL 5 software (details are shown in Section 3.3.1).

6.3 Results

6.3.1 Microstructure evolution of Mg alloy AZ31 during the RT-rolling and CT-rolling process

Figure 6.2 (a) and (b) show the optical microscope characterised microstructure of Mg alloy AZ31 samples after the RT-rolling process. Abundant black bands were observed, most bands

were insides grains and identified as deformation bands, and those that crossed the grain boundaries (GBs) were identified as shear bands (annotated in Figure 6.2 (b)). The quantity of these black bands notably increased with the increase in the deformation levels from 3% to 13%, which was in good agreement with the results in the literature [14]. With a TR =3% (Figure 6.2 (a)), these black bands were short and thin, and were mainly found inside the grains. When the TR increased to 13%, these black bands became thickened and considered as deformation bands. It is clearly demonstrated in Figure 6.2 (a) and (b) that the density of the deformation bands increased with higher TR values.

Figure 6.2 (c) and (d) present the microstructures of the Mg alloy AZ31 during the CT-rolling process. The short and straight grey lines could be deformation twins, which were further confirmed by the EBSD observations in Figure 6.3-8. At TR=3%, more twins were observed in the CT-rolled sample in Figure 6.2 (c), compared to that in the RT-rolled sample (Figure 6.2 (a)). As the TR increased to 13% (Figure 6.2 (d)), the density of twins in the CT-rolled sample increased, and these twin boundaries intersected and tangled with each other. Almost no deformation bands or shear bands were observed in the CT-rolled sample.

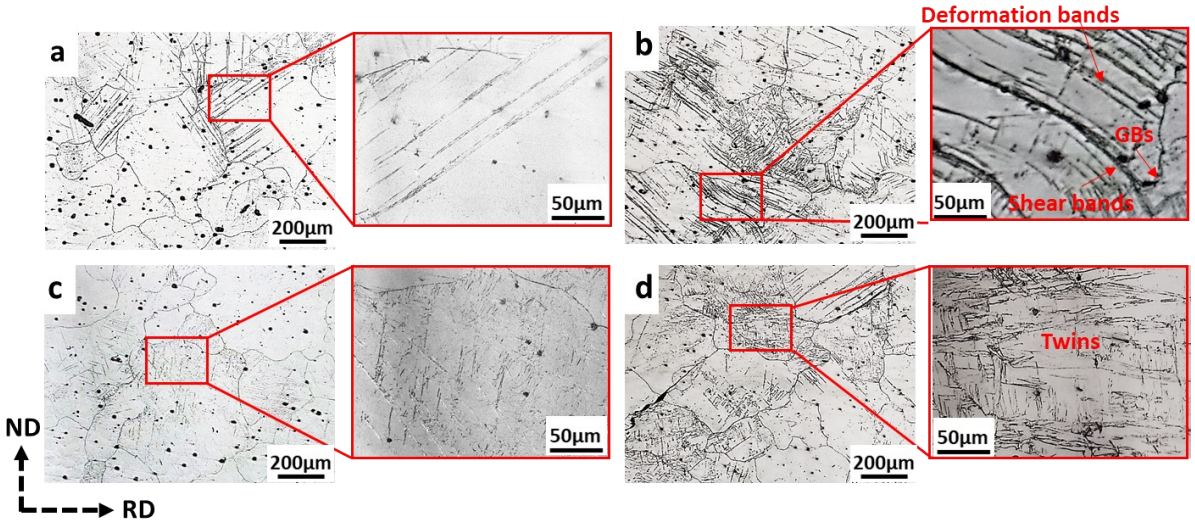

Figure 6.2 Optical images and the corresponding enlarged images of the (a-b) RT-rolled and (c-d) CT-rolled Mg alloy AZ31 samples. The total TRs of the samples are (a, c) 3% and (b, d) 13%.

Figure 6.3 provides a detailed analysis of the twin types in the 3% RT-rolled and the 3% CT-rolled samples. The twin boundaries were identified by their specific misorientations around the specific axis, such as, tension twins show ~ 86° about an <11$\bar{2}$0> axis. As shown in Figure 6.3 (a-d), three types of twins, i.e. {10$\bar{1}$2} TTWs, {10$\bar{1}$1}-{10$\bar{1}$2} DTWs and {10$\bar{1}$1} CTWs, were observed in the 3% RT-rolled sample. These twins were visualised in Figure 6.3 (b), where the green, blue and yellow lines represent {10$\bar{1}$1}-{10$\bar{1}$2} DTWs, {10$\bar{1}$2} TTWs and {10$\bar{1}$1} CTWs, respectively. According to Figure 6.3 (b) and (c), it can be concluded that the black bands in Figure 6.3 (c) and Figure 6.2 (a) were {10$\bar{1}$1}-{10$\bar{1}$2} DTWs, indicating that DTWs were the major deformation structure at the early stage of the RT-rolling process (i.e. TR=3%). These three twin types were also identified from the peaks in the misorientation distributions in Figure 6.3 (d). The misorientation axes and angles of these twins were plotted in the corresponding axis distribution in Figure 6.3 (d) and labelled with boxes and circles in corresponding colours. According to these axis distributions, the misorientation peaks at 38°, 56° and 86° all shared the <11$\bar{2}$0> axis and corresponded to {10$\bar{1}$1}-{10$\bar{1}$2} DTWs, {10$\bar{1}$1} CTWs, and {10$\bar{1}$2} TTWs, respectively.

Figure 6.3 (e-h) shows the analysed twinning behaviour in the 3% CT-rolled sample. Abundant TTWs were observed in the 3% CT-rolled sample in Figure 6.3 (f) and (h), confirming that the short black lines, presented in Figure 6.3 (g) and Figure 6.2 (c), were TTWs, which were the major microstructure at CT. The 3% CT-rolled sample had a much higher density of twins (Figure 6.3 (f)) than the 3% RT-rolled sample (Figure 6.3 (b)). As observed in Figure 6.3 (f) and (h), the main twin type in the CT-rolled sample was {10$\bar{1}$2} TTWs. A small fraction of (10$\bar{1}$2)-(01$\bar{1}$2) twin-twin interactions at 60˚ was also presented. The (10$\bar{1}$2)-(01$\bar{1}$2) twin-twin interaction forms when a grain twins on both the (10$\bar{1}$2) and (01$\bar{1}$2) planes, and 60° <10$\bar{1}$0> is the relationship between these two tension twin variants.

Table 2.1 listed three different misorientation relationships between two different tension twin variants [41]. From the axis distributions in the insets of Figure 6.3 (h), the peak at 86° around a <11$\bar{2}$0> axis was TTWs, and the peak at 60° around a <10$\bar{1}$0> rotation axis was the (10$\bar{1}$2)-(01$\bar{1}$2) twin-twin interactions. However, a rarely reported peak at 45° shared a <20$\bar{2}\bar{1}$> axis, as seen in Figure 6.3 (h). This peak is associated with the twinning sequence, which will be analysed in detail in the following section.

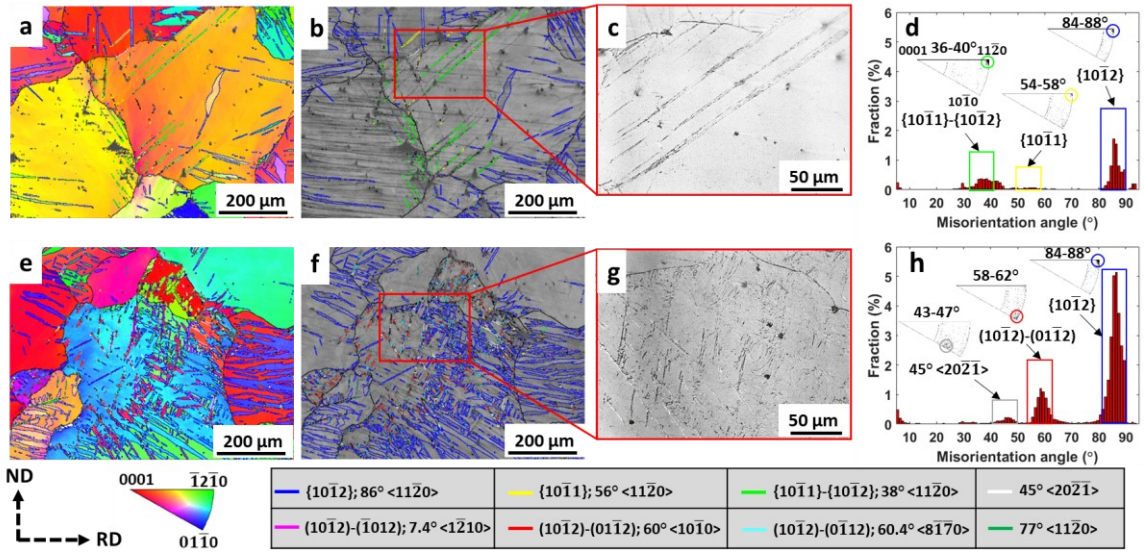

Figure 6.3 EBSD analysis of the (a-d) RT-rolled and (e-h) CT-rolled Mg alloy AZ31 samples with a total TR of 3%. (a) and (e) EBSD IPF maps, (b) and (f) band contrast maps with twin boundaries, (c) and (g) enlarged optical images, (d) and (h) misorientation distribution maps. Note that the characteristic misorientation axes and angles of the twins have been labelled using boxes and circles in (d) and (h) with the corresponding colours.

EBSD analysis was also performed on the 13% RT-rolled and 13% CT-rolled samples, as shown in Figure 6.4. By comparing Figure 6.4 to Figure 6.3, insights into the evolution of twinning and deformation bands can be gained. Abundant deformation bands with few twins were observed in the RT-rolled samples. As the grinding and polishing were conducted with care, the high-quality surface finishing was achieved. The grey colour represents the low band contrast (Figure 6.4 (b) and Figure 6.6 (b)), indicating the low degree of lattice perfection and high local misorientation density in the area. This would be attributed to the intensive shear strains and deformation localization in deformation bands [14, 82]. Therefore, the thick lines

with a grey colour were identified as deformation bands. This can also be confirmed by comparing the EBSD map with the optical image in Figure 6.4 (c), where bent and thickened lines were deformation bands and the bands which crossed GBs were shear bands. The similar structures were also reported in Mg alloy AM80 under dynamic loading conditions [77]. Considering the twin types, $\{10\bar{1}2\}$ TTWs, $\{10\bar{1}1\}$ CTWs and $\{10\bar{1}1\}$-$\{10\bar{1}2\}$ DTWs were observed in the 13% RT-rolled sample in Figure 6.4 (b) and (d), which were similar to that in the 3% RT-rolled sample (Figure 6.3 (b)). Comparing the 3% and 13% RT-rolled samples in Figure 6.3 (a-d) and Figure 6.4 (a-d), it can be concluded that, during the RT deformation, the formation of deformation bands was one of the important deformation mechanisms. Supplementary Figure B.1 plots more detailed features of the microstructures in the RT-deformed samples at 3% and 13%. It was found that DTWs, as evidenced by the straight lines in Supplementary Figure B.1, dominated at 3%, while deformation bands and few shear bands, which were thick and bent, dominated at 13%.

Figure 6.4 (e-h) presents the microstructure analysis in the 13% CT-rolled sample. More twin boundaries and fewer deformation bands were observed in Figure 6.4 (e) and (f). Additionally, a considerable amount of $\{10\bar{1}2\}$ TTWs and twin-twin interactions, mainly including $(10\bar{1}2)$-$(01\bar{1}2)$ and $(10\bar{1}2)$-$(\bar{1}012)$, were identified in the 13% CT-rolled sample, as shown in Figure 6.4 (f-h). Also, it is interesting to see that the 45° twin-twin misorientations around the $<20\bar{2}\bar{1}>$ axis are presented in the sample. Comparing the 3% and 13% CT-rolled samples in Figure 6.3 (e-h) and Figure 6.4 (e-h), as the plastic strain increased, the major twinning types were similar, but twinning activities were more commonly seen. For example, more $(10\bar{1}2)$-$(01\bar{1}2)$ twin-twin interactions and 45° $<20\bar{2}\bar{1}>$ twin boundaries were observed. Some rare 77° $<11\bar{2}0>$ boundaries, which could be generated by the TTW, were also seen in the CT-rolled sample, and these twin boundaries were also reported in the AZ80 Mg alloy under dynamic impact loading [132].

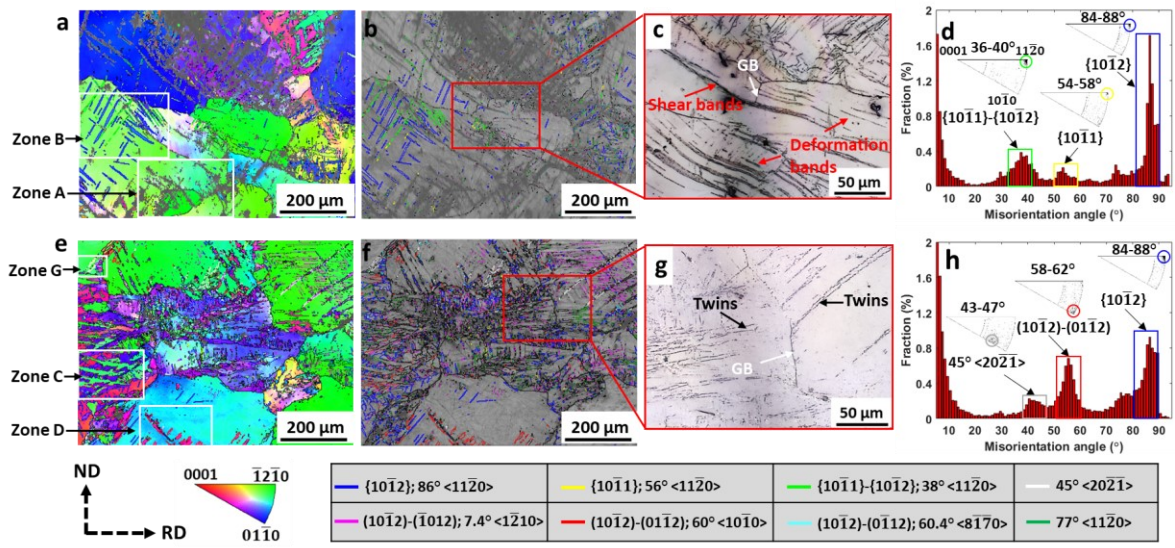

Figure 6.4 EBSD analysis of the (a-d) RT-rolled and (e-h) CT-rolled Mg alloy AZ31 samples with a total TR of 13%. (a) and (e) EBSD IPF maps, (b) and (f) band contrast maps with twin boundaries, (c) and (g) enlarged optical images, (d) and (h) misorientation distribution maps. The characteristic misorientation axes and angles of the twins have been labelled using boxes and circles in (d) and (h) with corresponding colours.

The KAM maps of the RT-rolled and CT-rolled samples with a TR of 3% and 13%, which can reflect the geometrically necessary dislocation (GND) density distributions [113, 133], were summarised in Figure 6.5. Generally, the KAM value progressively increased with the increase in deformation levels from 3% to 13% in both RT-rolled and CT-rolled samples, indicating that the higher GND density was generated in a higher TR. As shown in Figure 6.5 (a) and (c), the KAM value was low around TTWs, but was high around the DTWs and twin-twin interactions in the RT-rolled and CT-rolled samples, respectively. More deformation bands with high KAM values were presented in the 13% RT-rolled sample in Figure 6.5 (b), while more twin-twin interactions with high KAM values were presented in the 13% CT-rolled sample in Figure 6.5 (d).

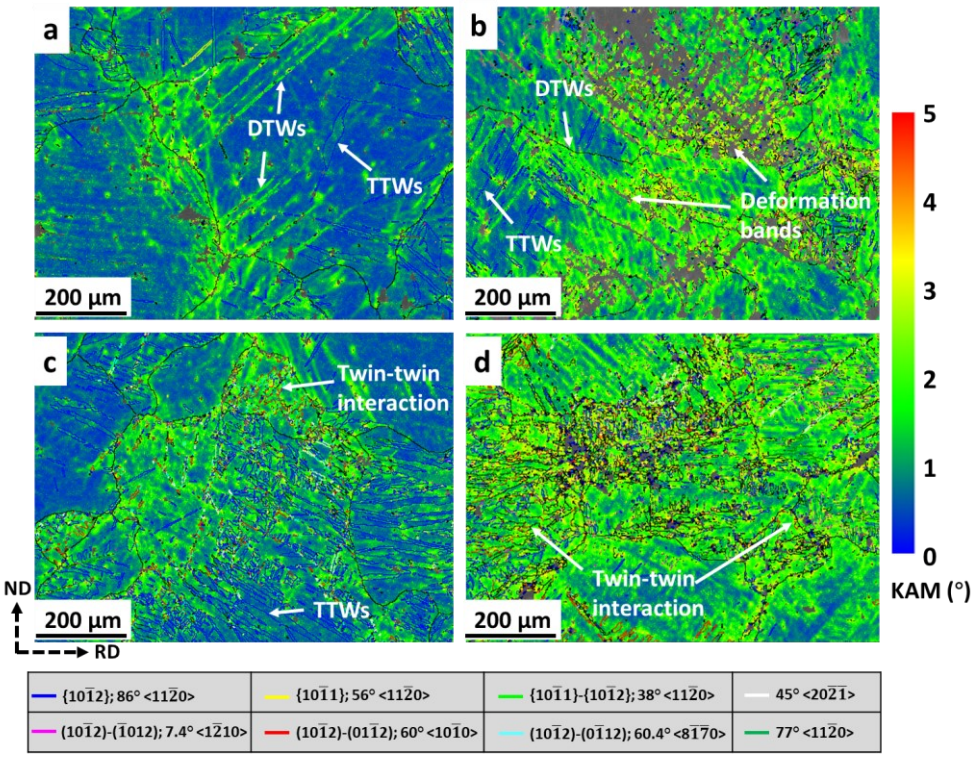

Figure 6.5 KAM maps of the RT-rolled samples with a total TR of (a) 3% and (b) 13%, and KAM maps of the CT-rolled samples with a total TR of (c) 3% and (d) 13%.

6.3.2 Typical zone analysis in the 13% RT-rolled and 13% CT-rolled Mg alloy AZ31 samples

Four typical zones, previously annotated as Zone A, Zone B, Zone C and Zone D in Figure 6.4 (a) and (e), were selected and analysed in detail to further reveal the twin and deformation bands distributions in the RT-rolled and CT-rolled samples. The detailed analyses, including EBSD IPF maps, band contrast maps, pole figures, KAM maps and misorientation distribution maps, were presented in Figure 6.6 and Figure 6.7. Zone G in Figure 6.4 (e) was also analysed in detail and presented in Supplementary Figure B.4 to show the 45° <20$\bar{2}\bar{1}$> boundaries clearly.

Figure 6.6 (a-d) shows the microstructures in Zone A, which contained significant deformation bands in the 13% RT-rolled sample. Deformation bands were narrow zones of intensive strains and hence high KAM values. From a careful observation of Figure 6.6 (a-c), high KAM values

were observed, especially around the deformation bands, indicating that deformation bands contained a wide range of internal misorientations and high local misorientation density.

Figure 6.6 (e-h) presents the microstructures in Zone B, aiming to understand the relationship between twins and deformation bands in the RT-rolling process. According to Figure 6.6 (e) and (h), twin variant B2 was $\{10\bar{1}2\}$ TTWs, and twin variants B3 and B4 were $\{10\bar{1}1\}$-$\{10\bar{1}2\}$ DTWs. As shown in Figure 6.6 (e) and (f), $\{10\bar{1}2\}$ TTWs were located outside the deformation bands, while $\{10\bar{1}1\}$-$\{10\bar{1}2\}$ DTWs were located in the deformation bands, indicating that DTWs would contribute to the deformation bands formation. This was also evidenced in the corresponding KAM maps in Figure 6.6 (g), where the local misorientation density was low in the $\{10\bar{1}2\}$ TTWs, while it was relatively high in the $\{10\bar{1}1\}$-$\{10\bar{1}2\}$ DTWs. The high local misorientation density in DTWs would be related to the high local misorientation density in deformation bands. Similar deformation bands and twinning behaviours were also observed in the RT-rolled sample with a TR of 9%, where abundant DTWs were located in the deformation bands with a high local misorientation density in Supplementary Figure B.2 (a-c) and Figure B.3 (a-b), confirming that DTWs are the major contributors to the deformation bands formation.

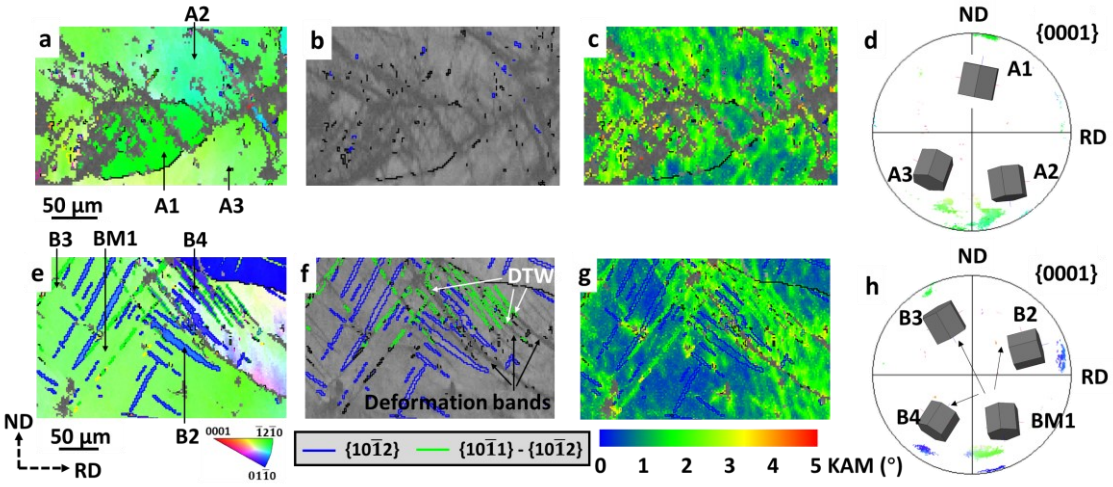

Figure 6.6 Microstructures in (a-d) Zone A and (e-h) Zone B of the 13% RT-rolled sample. Note that the locations of Zone A and Zone B are annotated in Figure 6.4 (a). (a, e) EBSD IPF maps, (b, f) band contrast maps with twin boundaries, (c, g) KAM maps and (d, h) {0001} pole figures.

Compared to the RT-rolled sample, the major deformation structure in the CT-rolled sample is twinning. There are abundant $(10\bar{1}2)$-$(01\bar{1}2)$ twin-twin interactions observed in the 13% CT-rolled sample. Figure 6.7 (a-d) gives a detailed microstructure analysis in Zone C from Figure 6.4 (e). The main twin types in Zone C were $\{10\bar{1}2\}$ TTWs and $(10\bar{1}2)$-$(01\bar{1}2)$ twin-twin interactions. As shown in Figure 6.7 (a), three tension twin variants, i.e. C2, C3 and C4, were generated from the parent matrix CM1, and the misorientations between the matrix and these twin variants were ~ 86°, as identified in Figure 6.7 (c) and (d). The $(10\bar{1}2)$-$(01\bar{1}2)$ twin-twin interactions were generated between twin variants C2 and C3. A 60° $<10\bar{1}0>$ misorientation between twin variants C2 and C3 was observed in Figure 6.7 (c) and (d). Figure 6.7 (b) presents the KAM map, where a high local misorientation density was observed around the boundaries of the twin-twin interactions.

Figure 6.7 (e-h) illustrates the microstructure analysis in Zone D of the 13% CT-rolled sample. The analysis of Zone D was used to clearly show the $(10\bar{1}2)$- $(01\bar{1}2)$ twin-twin interaction. As shown in Figure 6.7 (e), (g) and (h), the $(10\bar{1}2)$-$(01\bar{1}2)$ twin-twin interaction was observed between twin variants D1 and D2. The misorientation between twin variants D1 and D2 was approximately 60° around an $<10\bar{1}0>$ axis, where an apparent single peak was observed in Figure 6.7 (h). The matrix was almost consumed by these two twin variants. This indicates that twinning is an effective means to accommodate plastic deformation in the CT condition. Also, the twin-twin interaction is an effective dislocation barrier, as demonstrated by the high KAM values near the twin boundaries, in Figure 6.7 (f).

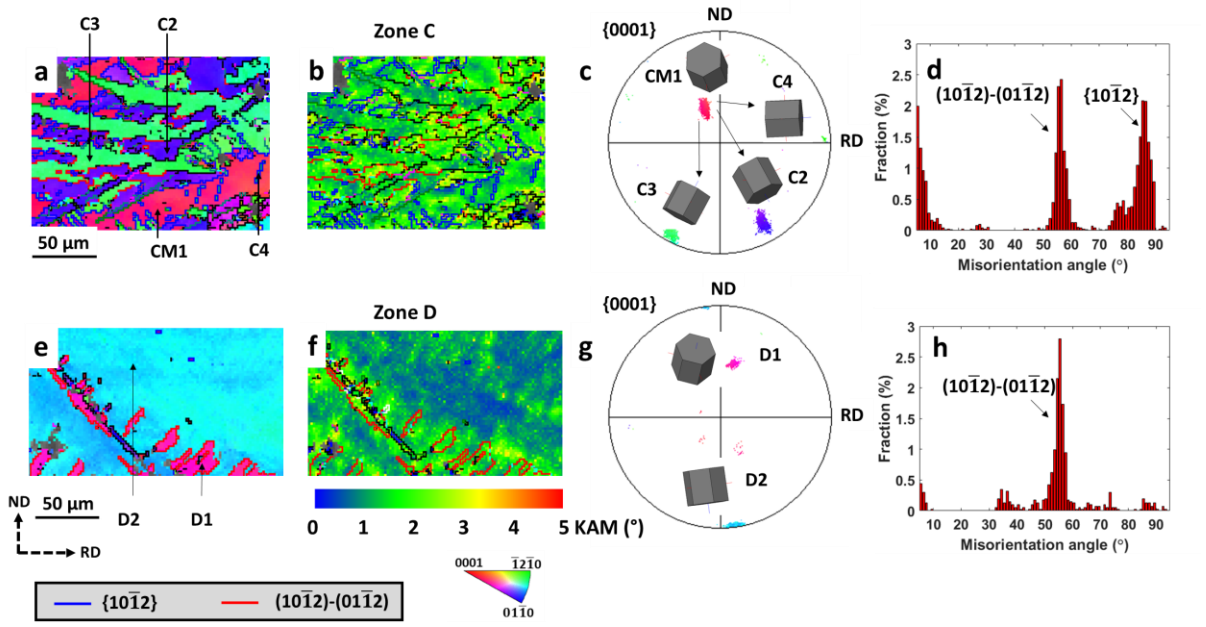

Figure 6.7 Microstructures in (a-d) Zone C and (e-h) Zone D of the 13% CT-rolled sample. Note that the locations of Zone C and Zone D are annotated in Figure 6.4 (e). (a, e) EBSD IPF maps, (b, f) KAM maps, (c, g) {0001} pole figures, (d, h) misorientation distribution maps.

6.3.3 Twinning sequence analysis

In the CT-rolled sample, a new twinning sequence was found. Primary TTWs formed first, and subsequently a set of secondary TTWs formed within them. To thoroughly study this twinning behaviour, two single grains, namely grain E and grain F, were taken from the 9% CT-rolled sample and analysed in detail in Figure 6.8. For clarity, the full EBSD maps of the 9% CT-rolled sample are presented in Supplementary Figure B.2 and Figure B.3.

Figure 6.8 (a-d) presents the analysis of grain E. It is difficult to use the captured EBSD map to distinguish the matrix with the twin variant and the sequence of the twin variants. Hence, possible twinning behaviours were described in this work, based on the misorientations and axes of typical twins. Figure 6.8 (a) and (c) plot the IPF map and the corresponding orientations of the matrix and twin variants in the {0001} pole figure. Three primary tension twin variants E2, E5 and E8 were generated from the matrix EM1, as observed in Figure 6.8 (a) and (c). The primary tension twin variants, E2, E5 and E8 interacted and formed the (10$\bar{1}$2)-(01$\bar{1}$2) twin-

twin interactions. The tension twin variant E8 consumed the majority of the matrix EM1, and no secondary twin was generated in twin variant E8. However, secondary tension twin variants, E3 and E4, were generated from primary twin variant E2. The two secondary tension twin variants, E3 and E4, also formed the secondary $(10\bar{1}2)$-$(01\bar{1}2)$ twin-twin interactions. It is worth noting that the primary twin variant E2 and secondary twin variants E3 and E4 were distributed along a line which was parallel to the red dotted line in Figure 6.8 (a). Secondary tension twin variants E6 and E7 were also generated from primary twin variant E5 and formed the secondary $(10\bar{1}2)$-$(01\bar{1}2)$ twin-twin interactions. These twin variants, E5, E6 and E7, were distributed along a line which was parallel to the black dotted line in Figure 6.8 (a). Therefore, a new twinning sequence of primary TTW-TTW interaction → secondary TTW-TTW interaction can be established. This special twinning sequence would result from the suppression of dislocation slips to accommodate the plastic strain at cryogenic temperature.

The secondary twin variants, i.e. E3, E4, E6 and E7, interacted with the primary twin variant E8 to generate a special ~45° misorientation around an $<20\bar{2}\bar{1}>$ axis (45° $<20\bar{2}\bar{1}>$). As shown in Figure 6.8 (c), in addition to the misorientation peak of 86° $\{10\bar{1}2\}$ TTWs and 60° $(10\bar{1}2)$-$(01\bar{1}2)$ twin-twin interaction, a ~45° misorientation peak was observed, resulting from the interactions between the secondary and the primary twin variants. Figure 6.8 (b) presents the KAM distributions around these twin-twin interactions. High KAM values were observed around the interactions, indicating that the boundaries of these twin-twin interactions would block the dislocation slips and result in a high local misorientation density. The active twinning behaviour would also contribute to the twinning-induced grain refinement.

Figure 6.8 (e-h) provides a similar microstructure analysis of grain F to confirm this twinning structure. As shown in Figure 6.8 (e-f), a similar twinning sequence was observed. The primary tension twin variants F2, F5 and F8 were generated from the matrix FM1. Although the volume

fraction of F8 is high, F8 is more likely to be a twin variant. As the *c*-axis of F8 is almost parallel to ND and the compression direction in the pole figure, it would be more difficult to activate the TTWs in this orientation of F8 than FM1 whose *c*-axis is almost perpendicular to the compression direction [37]. It is also reasonable to observe the high volume fraction of F8, because TTWs can form a profuse and coarse structure and consume the majority of the parent structure at 9% deformation [94]. The primary twin variants F2 and F5 interacted with the twin variant F8 to form 60° <$10\bar{1}0$> boundaries, namely ($10\bar{1}2$)-($01\bar{1}2$) twin-twin interactions. The secondary tension twin variants F3 and F4 were generated from the primary twin variant F2, and these three twin variants were distributed parallel to the red dotted line in Figure 6.8 (e). These two secondary tension twin variants F3 and F4 interacted and formed the secondary ($10\bar{1}2$)-($01\bar{1}2$) twin-twin interaction. The secondary twin variants F6, F7 and primary twin variant F5 also showed a similar relationship to the secondary twin variants F3, F4 and primary twin variant F2, but the twin variants F5, F6 and F7 were distributed parallel to the black dotted line in Figure 6.8 (e). According to Figure 6.8 (e) and (g), the secondary tension twin variants F3, F4, F6 and F7 interacted with the primary tension twin variant F8 to form 45° <$20\bar{2}\bar{1}$> boundaries. Three misorientation distribution peaks, including 86°{$10\bar{1}2$} TTWs, 60° ($10\bar{1}2$)-($01\bar{1}2$) twin-twin interactions and 45° <$20\bar{2}\bar{1}$> boundaries, were observed in Figure 6.8 (h). As shown in Figure 6.8 (f), higher KAM values were observed around boundaries of these twin-twin interactions, compared to other areas in grain F, indicating that these boundaries of twin-twin interactions would block and accumulate GNDs effectively. The analysis of grain E and grain F concluded that there was a special twinning sequence behaviour in the CT-rolled sample, where secondary TTWs formed on the primary TTWs and interacted with another set of primary TTWs to form 45° <$20\bar{2}\bar{1}$> boundaries. The detailed analysis of grain E and grain F confirmed the occurrence of the specific twinning sequence and twin-twin interactions in the

CT-rolled sample. Additionally, the twinning behaviour was thoroughly explained with the configurations of the lattice orientations.

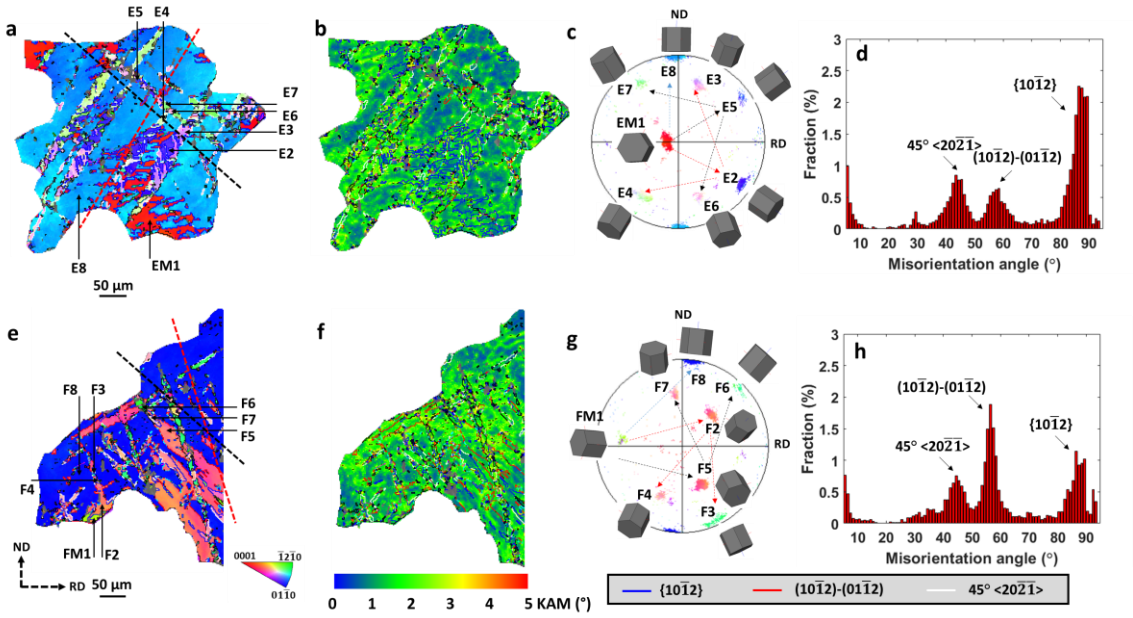

Figure 6.8 Detailed microstructure analysis of (a-d) grain E and (e-h) grain F in the 9% CT-rolled sample. (a, e) EBSD IPF maps, (b, f) KAM maps, (c, g) {0001} pole figures and (d, h) misorientation distribution maps.

6.4 Discussion

6.4.1 Illustration of the microstructure evolution during the RT-rolling and CT-rolling process

An integrated schematic illustration of the microstructure evolution during the RT-rolling and CT-rolling process with respect to deformation levels was presented in Figure 6.9. At the early stage of the RT-rolling (from Figure 6.9 (a) to (b)), some {10$\bar{1}$1}-{10$\bar{1}$2} DTWs, few TTWs and deformation bands were generated. With the increase in the deformation levels (from Figure 6.9 (b) to (c)), more deformation bands were generated and transformed from the existing DTWs, to accommodate the plastic deformation. Some deformation bands were transferred into shear bands crossing the grain boundaries, and a small amount of TTWs and DTWs were still left in the matrix. Abundant dislocations were observed in the RT-rolled

sample and accumulated around the deformation bands and DTWs (Figure 6.5-6 and Figure 6.9).

During the CT-rolling process, the main deformation structures were twins, including TTWs, twin-twin interactions and twinning sequence. At the initial deformation stage, a significant amount of thin and individual twins, especially the TTWs, were generated in the CT-rolled sample, as shown in Figure 6.3 (e-h), Figure 6.9 (d) and (e). With the increase in deformation levels, unlike the RT-rolled sample, where DTWs were transformed into deformation bands, active twin behaviours occurred to accommodate further plastic strains during the CT-rolling process. As shown in Figure 6.4 (e-h) and Figure 6.9 (f), the TTWs interacted to form $(10\bar{1}2)$-$(01\bar{1}2)$ twin-twin interactions. Additionally, the secondary TTWs were generated from the primary TTWs to form $\{10\bar{1}2\}$-$\{10\bar{1}2\}$ double tension twins, which is the so-called twinning sequence. More importantly, the secondary twin-twin interaction in the primary twin-twin interaction was observed for the first time, creating a specific misorientation of ~45° between the primary TTW variant and another secondary TTW variant, as shown in Figure 6.8 and Figure 6.9 (f). The detailed twinning behaviours, including the twinning sequence, were shown in the insets below. Primary twin variants T1 and T2 formed the twin-twin interaction, and then the secondary twin variant T3 in the primary twin variant T1 would meet with another primary twin variant T2 to form the specific boundaries, namely 45° $<20\bar{2}\bar{1}>$ boundaries. The GND accumulations were mainly located around the boundaries of twin-twin interactions and twinning sequence in the CT-rolled sample, according to Figure 6.5-9.

Regarding the investigation of deformation behaviours in the uniaxial compression tests in Chapter 5, this special twinning sequence was not observed in the CT compression test, and almost no deformation bands and shear bands were observed in the RT compression test. This could be attributed to the more inhomogeneous deformation in the rolling tests than the uniaxial

compression tests. The Mg alloy sample was deformed under compressive stress in the uniaxial compression tests, while the sample was deformed under both compressive and shear stress in the rolling tests, resulting in multiaxial stress states and more inhomogeneous deformation. This would promote twinning sequence (at CT) and deformation bands or shear bands (at RT) to accommodate the plastic deformation in the rolling tests.

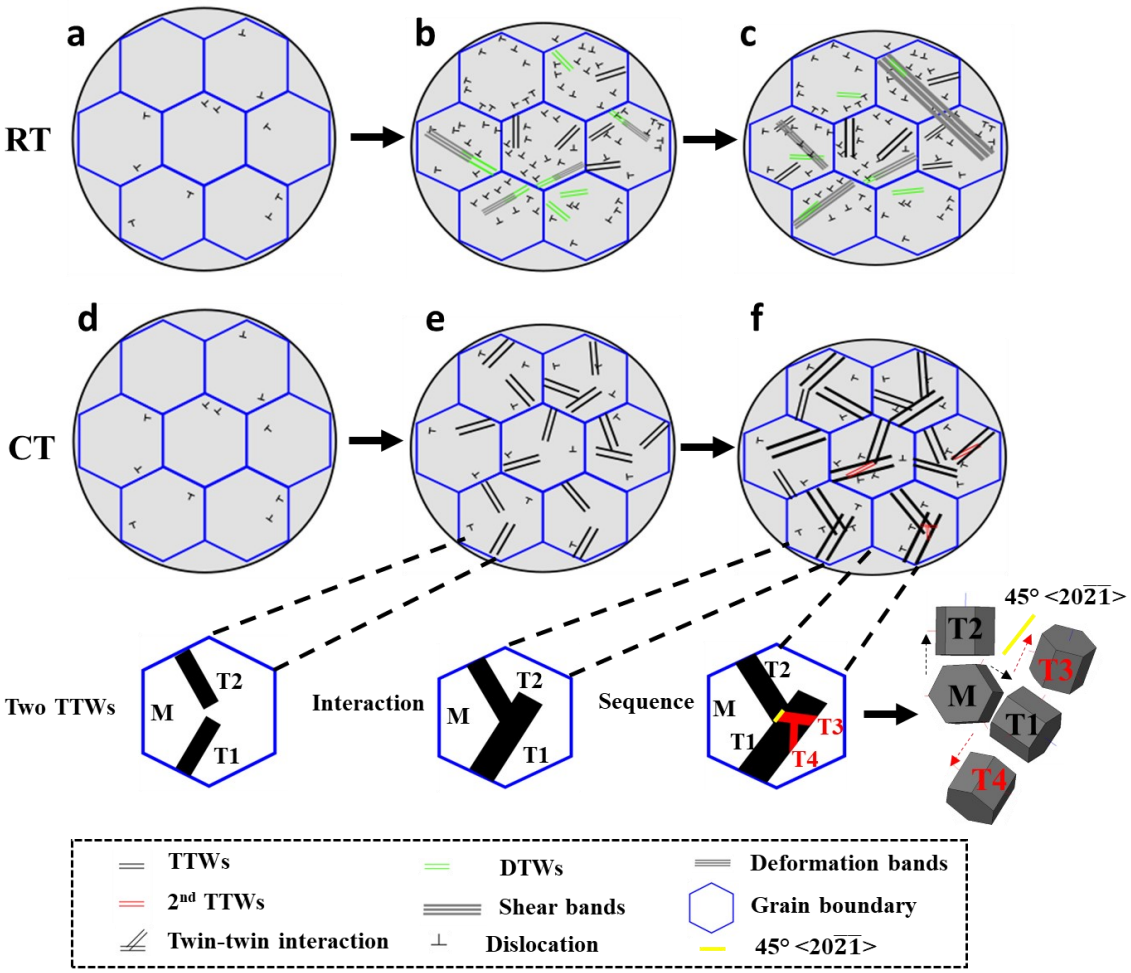

Figure 6.9 Schematic illustration of the microstructure evolution during (a-c) the RT-rolling and (d-f) CT-rolling process. Insets plot the formation process of twin-twin interactions and twinning sequence. Note that deformation bands are located inside grains while shear bands cross grain boundaries.

6.4.2 Twinning behaviours during the CT-rolling process

During the CT-rolling process, the active twinning behaviour including abundant TTWs and twin-twin interactions would be attributed to the limited dislocation slips and significant local

stress concentrations. Abundant twins were also reported in the CT-rolling of titanium, and it was speculated that it was easier to activate the twins at CT compared to at RT, which would be attributed to the significant local stress concentrations near grain boundaries [73]. The formation of abundant twins and twin-twin interactions in the CT-rolled Mg alloy is also consistent with the twinning behaviours in the CT-deformed sample under the uniaxial compression tests in Chapter 5. The explanations for the active twin behaviour at CT can be seen in Section 5.4. However, more rarely reported twinning behaviours, including $\{10\bar{1}2\}$-$\{10\bar{1}2\}$ double tension twins and the special twinning sequence were observed in the CT-rolled sample, this could be due to more significant stress concentrations induced by inhomogeneous deformation during the rolling tests.

The rare $\{10\bar{1}2\}$-$\{10\bar{1}2\}$ double tension twins were observed during the CT-rolling process, and the twins were different from $\{10\bar{1}1\}$-$\{10\bar{1}2\}$ DTWs, which were commonly observed in the deformation process at RT [26, 31]. $\{10\bar{1}2\}$-$\{10\bar{1}2\}$ double tension twins were generally observed in multiaxial stress fields [68, 71] or a cryogenic temperature [72]. The reason for the formation of the unusual $\{10\bar{1}2\}$-$\{10\bar{1}2\}$ double tension twins could also be attributed to the high local stress. It was proposed that the formation of $\{10\bar{1}2\}$-$\{10\bar{1}2\}$ double tension twins was caused by difficult non-basal slips at the cryogenic temperature [72], which could result in stress concentrations, because no sufficient dislocation slips were effectively generated to relieve the local stresses. In addition, the twin transformations, such as ~13% shear induced by TTWs, could induce local stress near the twins [134], and the high local stress near TTWs could provide the stress for the nucleation of secondary TTWs.

Regarding the formation of the special twinning sequence, i.e. the secondary twin-twin interaction in the primary twin-twin interaction, it could be attributed to the following reasons. (i) The primary twin-twin interaction would generate high local stress around the boundaries

[62], which could promote secondary twin nucleations. (ii) As the required stress for dislocation slip is higher at lower temperatures, more secondary twins were generated to accommodate the further plastic strain. Finally, these secondary twins would grow and meet to form the secondary twin-twin interactions in the primary twin-twin interactions.

The high local misorientation density was observed around the boundaries of twin-twin interactions and twinning sequence. The high local misorientation density around these twin boundaries would be attributed to the following reasons. Firstly, the structures of twin-twin interactions and twinning sequence are generally fine, so the dislocation slips will be blocked effectively by their twin boundaries, according to the boundary hardening effects [107]. Secondly, the twin variants in twin-twin interactions and the twinning sequence would show different orientations and provide various paths for dislocation slips, resulting in abundant dislocation accumulations. In addition, twin-twin boundaries in twin-twin interactions could react to form boundary dislocations [61, 63].

6.4.3 Deformation bands formation during the RT-rolling process

According to Figure 6.2, Figure 6.4-6 and Supplementary Figure B.1, abundant deformation bands were observed in the RT-rolled sample, as these bands contained shear layers and accumulated abundant GNDs. For the bent bands which passed through the grain boundaries in the 13% RT-rolled sample, they would be shear bands. These phenomena were the typical features in deformation bands and shear bands, confirming that these bands in the 13% RT-rolled sample were mainly deformation bands and few shear bands [74].

The formation of deformation bands in Mg alloys generally resulted from the evolvement of twinning or dislocations [74, 75]. As shown in Figure 6.3 (a-d) and Figure 6.6, the main microstructures in the RT-rolled sample with a TR of 3% were $\{10\bar{1}2\}$ TTWs, $\{10\bar{1}1\}$-$\{10\bar{1}2\}$ DTWs and $\{10\bar{1}1\}$ CTWs. In Figure 6.4 (a-d) and Figure 6.6, with the TR increasing to 13%,

abundant deformation bands were generated in the RT-rolled AZ31 sample, and some $\{10\bar{1}1\}$-$\{10\bar{1}2\}$ DTWs and $\{10\bar{1}1\}$ CTWs were observed. Only DTWs were located within the deformation bands with a high local misorientation density, indicating that these DTWs accommodated the large plastic strain and could contribute to the formation of deformation bands.

DTWs in deformation bands provided a favoured path for basal slips, and substantial dislocation slips would pile up around these twin boundaries, resulting in stress concentrations and the distortion of these twin boundaries (Figure 6.6 (g)). The local misorientation density was generally high inside deformation bands, which could be related to the high local misorientation density in DTWs, as observed in Figure 6.6 (c) and (g) and also in Ref [135]. In addition, the basal planes in DTWs were reoriented to be well oriented for slips, and this could also result in crystallographic softening in these twins [31]. Therefore, these phenomena in DTWs were strongly linked to the deformation bands where abundant dislocation slips and softening occurred, confirming that the deformation bands originated from DTWs in the RT-rolled sample. This result was in good agreement with some research on the formation of deformation bands [14, 136].

TTWs were located outside these deformation bands with low local misorientation density in Figure 6.6 (f) and (g), indicating that TTWs may not play an important role in the formation of deformation bands. TTWs were generally unfavourably oriented for basal slips, while basal slips were frequently observed in DTWs [16]. Hence a higher local misorientation density was expected around DTWs compared to TTWs. It was found that basal slips could be easily transmitted through TTWs boundaries [95], so the dislocation pile-ups along TTWs boundaries could be low, resulting in difficulty accumulating GNDs around these boundaries and contributing to the deformation bands formation.

6.5 Summary

In this chapter, a detailed microstructure analysis was performed on the RT-rolled and CT-rolled Mg alloy AZ31 samples. The deformation structures at RT and CT were examined, delivering comprehensive understandings of the evolved deformation twins, deformation bands, GNDs and their dynamic interactions. More importantly, a rarely observed twinning sequence formed in the CT-rolling process to accommodate the plastic deformation. The following conclusions were made:

(1) A new deformation behaviour (i.e. twinning sequence): primary TTW-TTW interactions → secondary TTW-TTW interactions, with a 45° <$20\bar{2}\bar{1}$> misorientation peak, was discovered in the CT-rolling process. This 45° <$20\bar{2}\bar{1}$> misorientation peak was created between the secondary and another primary tension twin variant.

(2) The major deformation structure during the RT-rolling process was identified as {$10\bar{1}1$}-{$10\bar{1}2$} DTWs → deformation bands, in which high local misorientation density accumulated around DTWs and contributed to the formation of deformation bands.

(3) Abundant twins, starting from {$10\bar{1}2$} TTWs to twin-twin interactions and the twinning sequence, were observed during the CT-rolling process. These active twinning behaviours would mainly result from the limited dislocation slips and high local stress in the CT-rolling process.

(4) The boundaries of twin-twin interactions and the twinning sequence were the preferential sites for dislocation accumulations, while the local misorientation density was low in TTWs.

7 Recrystallization mechanisms in twin-twin interactions and deformation bands

7.1 Introduction

In Chapter 6, it was found that twin-twin interactions and deformation bands were the main deformation structures in CT-rolled and RT-rolled samples, respectively. These two deformation structures also have a significant influence on recrystallization in the CT-deformed and RT-deformed samples during the hot deformation process in Chapter 4. However, it is still unclear how the texture and microstructure evolve in the recrystallization near twin-twin interactions and deformation bands. It is also worth conducting a detailed investigation of the recrystallization in these two deformation structures and their relationship with dislocations.

In this chapter, to study the individual effects of twin-twin interactions and deformation bands on recrystallization, the microstructure evolution of the CT-rolled and RT-rolled samples during the annealing process was analysed using the *quasi-in-situ* EBSD method, respectively. The texture evolution at different annealing periods was studied to explain the texture formation in these two annealed samples and their relationship with twin-twin interactions and deformation bands. Their grain size evolution was also studied and compared. Furthermore, the recrystallization and its relationship with dislocations in twin-twin interactions, tension twins and deformation bands were analyzed using KAM maps.

7.2 Experimental programme

7.2.1 Material and experimental tests

The as-received material in this research is an as-cast Mg alloy AZ31 (Mg-Al-Zn alloys class) provided by Magnesium Elektron, and its chemical compositions are shown in Table 3.1.

Figure 7.1 shows the schematic processing of rolling at RT and CT, and the subsequent annealing. The rolling plates with a length, width and thickness of 100 mm, 35mm and 10 mm were machined from as-received samples using an electro-discharged machine (EDM).

The rolling tests were conducted at a rolling speed of ~ 5 m/min using a FSM200 powered rolling mill. The same nominal thickness reduction for the rolling tests was applied for all materials, and the final thickness reduction of these rolling tests at RT and CT was measured as ~9%. After the rolling process, two samples were cut from a similar location of the RT-rolled and CT-rolled samples, respectively. These samples were annealed at 300 °C for 5, 10, 70 and 110 min to study the recrystallization nucleation during the initial stage. As 300 °C is a common recrystallization temperature [137], this temperature was chosen to achieve the effective grain refinement through recrystallization.

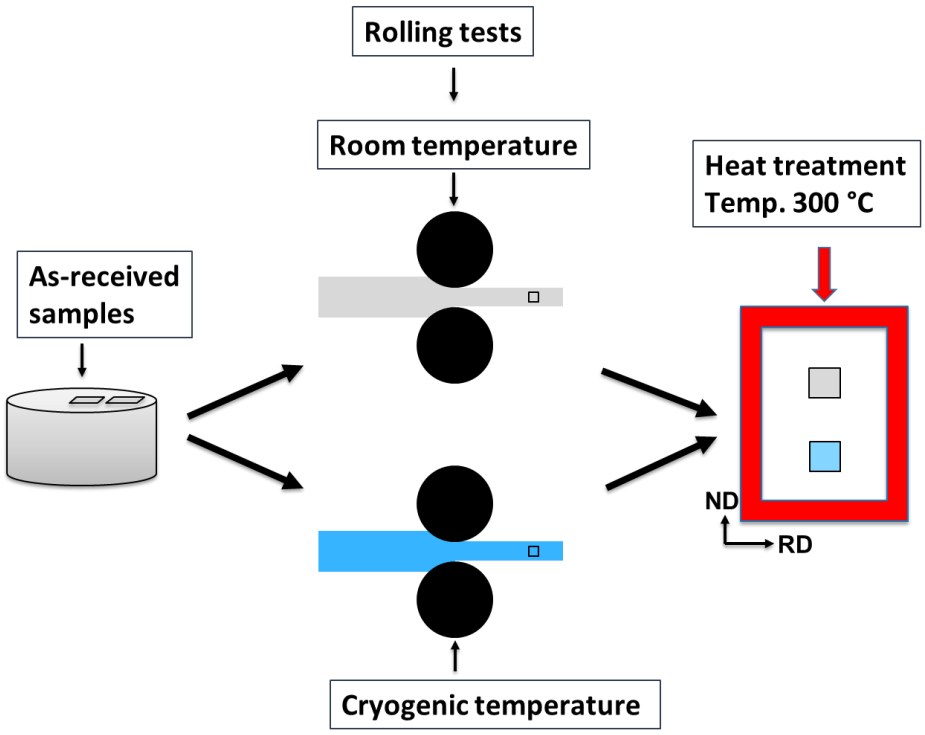

Figure 7.1 Schematic processing diagram of the rolling tests at room and cryogenic temperatures, and the subsequent heat treatment processes.

7.2.2 Microstructure characterisation

The EBSD characterization was made on the RD × ND planes. For the annealed samples, the same region of interest at the corner of the surface was traced by EBSD during the annealing process. A 2505 μm × 1887 μm EBSD map with 3 μm step size at ×50 magnification was obtained to capture the microstructure of the rolled samples. For the annealed samples, the step size of EBSD scanning was set as 8 μm. The step size of 8 μm is sufficient to capture the essential microstructure information for these samples, while the finer step size of 3 μm was selected for the rolled samples to obtain the detailed information about twinning and deformation bands. The EBSD pattern indexing rate was about 90~95%, which met the requirement to obtain high-quality images. The number of grains in the annealed samples was about 1000~1500 grains, which could ensure a statistical EBSD analysis. During the annealing process, these samples were repeatedly characterized and annealed from SEM to a preheated Lenton furnace. Note that water quenching was undertaken for these two samples to retain the annealing microstructure. Gentle OPS polishing was also conducted to remove the thin oxide formed on the sample surface.

The acquired EBSD data were analysed using the HKL CHANNEL 5 software. The detailed analysis processes of the twin boundaries, KAM maps, texture and grain size were shown in Section 3.3.1. The recrystallized grains in the RT-rolled and CT-rolled samples were detected using the recrystallized fraction component of this software [93]. The grains with internal average misorientation angles above 1° were identified as deformed grains. If internal average misorientation angles of some grains were below 1° but the misorientations between subgrains in these grains were above 1°, these grains were identified as substructured grains. The remaining grains were classified as recrystallized grains [138]. The texture of the recrystallized grains in these samples was analysed using the pole figure. For brevity, the microstructure

analysis including IPF maps and pole figures for 5 and 110 min was shown in Supplementary Figure C.1.

7.3 Experimental results

7.3.1 The microstructures of the RT-rolled and CT-rolled samples

Figure 7.2 (a) and (c) show the Inverse Pole Figure (IPF) images of the RT-rolled and CT-rolled Mg alloy AZ31 samples, respectively. According to the band contrast (BC) image superimposed by various twin boundaries in Figure 7.2 (b), abundant deformation bands are observed in the RT-rolled sample. Few twins including $\{10\bar{1}2\}$ tension twins (TTWs) and $\{10\bar{1}1\}$-$\{10\bar{1}2\}$ double twins (DTWs) are also observed. This is in good agreement with the results reported in the cold-rolled pure Mg and Mg alloys [14].

Compared to the RT-rolled Mg alloy AZ31 sample, fewer deformation bands and more twin boundaries are observed in the CT-rolled Mg alloy AZ31 sample, as shown in Figure 7.2 (b) and (d). The main twin types in the CT-rolled sample are $\{10\bar{1}2\}$ TTWs and $(10\bar{1}2)$-$(01\bar{1}2)$ twin-twin interactions. Abundant twin boundaries interact with each other to form twin-twin interactions, and these twin-twin interactions show finer structures. As the deformation structures are different in CT-rolled and RT-rolled samples, distinct recrystallization behaviours would be expected in the annealed CT-rolled and RT-rolled samples.

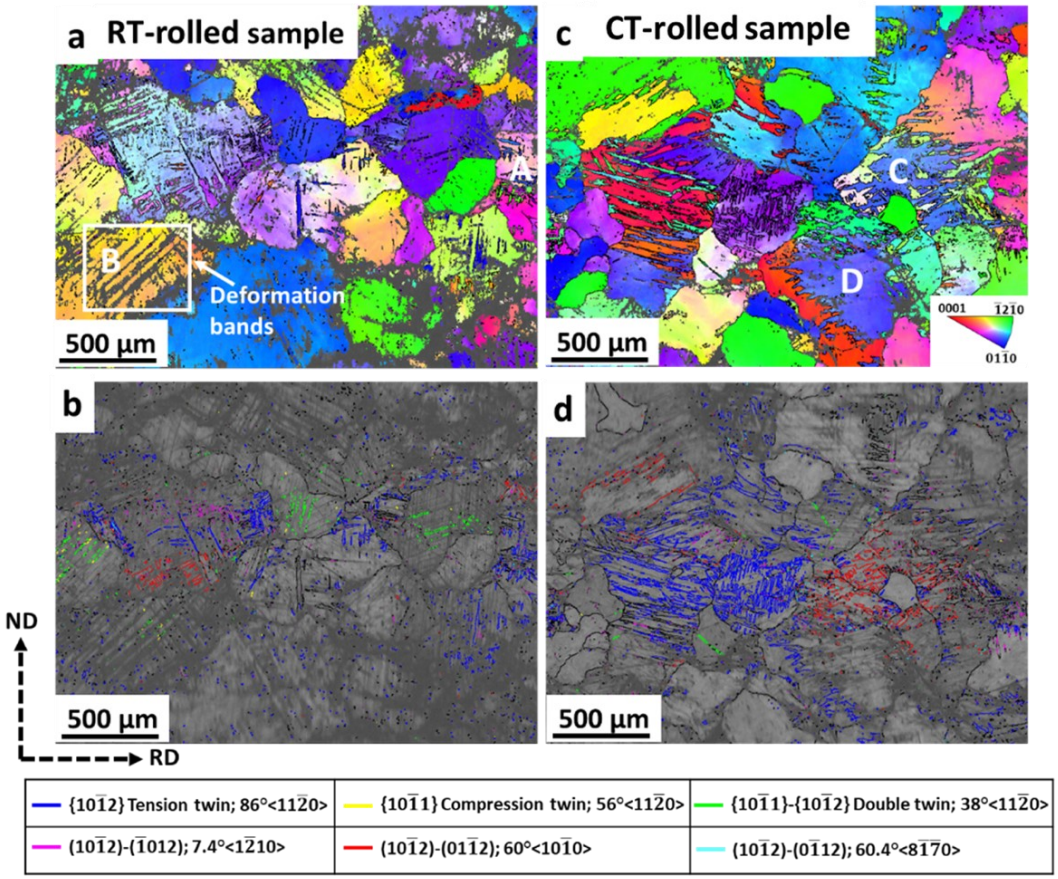

Figure 7.2 (a, c) EBSD inverse pole figure (IPF) maps, and the corresponding (b, d) band contrast (BC) maps superimposed by various twin boundaries of the room-temperature (RT)-rolled and cryogenic-temperature (CT)-rolled samples, respectively.

7.3.2 Microstructure evolution during the annealing process

In order to systematically study the microstructure evolution during the annealing process, the *quasi-in-situ* EBSD tests are conducted for both RT-rolled and CT-rolled samples. Figure 7.3 plots IPF maps of the RT-rolled and CT-rolled samples, and the corresponding samples in the annealing process at 300 ℃ for 10 and 70 min, respectively. The recrystallized grains are highlighted in a bright colour, and the unrecrystallized grains are not plotted. The corresponding {0001} pole figures from the recrystallized grains are plotted in the subsets.

After the annealing process at 300 ℃ for 10 min in Figure 7.3 (b), most new grains in the RT-rolled sample nucleate around the deformation bands including the deformed areas near grain boundaries. The texture of recrystallized grains in the annealed RT-rolled sample is strong and

close to the centre of pole figure. However, in Figure 7.3 (e), the recrystallized grains in the annealed CT-rolled sample are located around $(10\bar{1}2)$-$(01\bar{1}2)$ twin-twin interactions, resulting in a much weaker and more scattered texture than that in the annealed RT-rolled sample.

In Figure 7.3 (c) and (f), after the annealing process at 300 °C for 70 min, more new grains nucleate, and the grain growth also occurs in these two samples. The deformation bands including the deformed areas near grain boundaries in the RT-rolled sample are almost consumed by the recrystallized grains, while the twin boundaries in the CT-rolled sample, especially boundaries of twin-twin interactions, are consumed by the recrystallized grains. The newly recrystallized grains in annealed CT-rolled sample could show more uniform grain size distribution than that in the annealed RT-rolled sample. The texture of the recrystallized grains in the annealed RT-rolled sample becomes stronger and concentrates in the centre of the pole figure, resulting in a typical basal texture. However, the texture of recrystallized grains in the annealed CT-rolled sample in Figure 7.3 (f) becomes weaker and more scattered, and several separate texture peaks are situated away from the centre of basal texture. Therefore, recrystallization around twin boundaries, especially twin-twin interactions, can weaken the texture and avoid forming a strong basal texture in the annealing process of the CT-rolled sample.

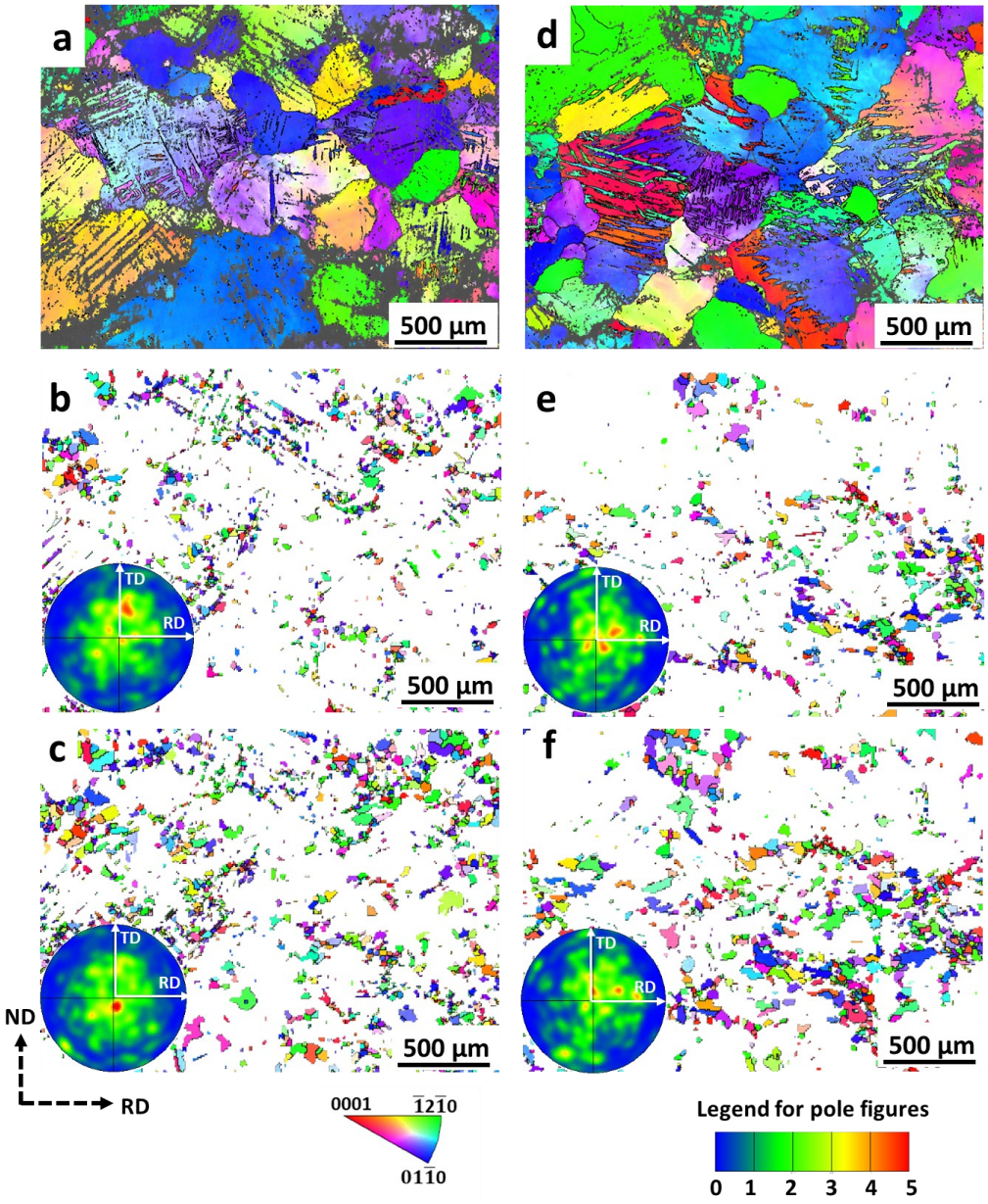

Figure 7.3 EBSD IPF maps and {0001} pole figures of recrystallized grains in the RT-rolled and CT-rolled samples during annealing at 300 ℃ for (a, d) 0, (b, e) 10 min, (c, f) 70 min, respectively. The unit of the colour bar is mud.

7.3.3 Texture evolution and its mechanisms during the annealing process

Four typical zones in the RT-rolled and CT-rolled samples are selected to investigate the texture behaviours during the annealing process, respectively, as shown in Figure 7.4. The recrystallized grains are highlighted in a bright colour, and the unrecrystallized grains are

plotted in a dark colour. The corresponding {0001} pole figures of the recrystallized grains in different zones are plotted in the subsets.

The main deformation structures in the RT-rolled sample are deformation bands, which provide the nucleation sites for recrystallization. As shown in Figure 7.4 (a), many deformation bands are distributed in this zone. At 10 min, most grains are recrystallized around the deformation bands, and the texture distribution of the recrystallized grains in this sample is relatively scattered (Figure 7.4 (b) and (g)). However, at 70 min, oriented grain growth occurs and basal grains shown as blue ones grow faster than non-basal grains, resulting in the concentration of the texture in the centre of the pole figure (Figure 7.4 (c) and (h)). This is in good agreement with the result reported in Ref [14], in which the strong basal texture is formed after hot rolling in Mg alloy AZ31.

As shown in Figure 7.4 (d), for another zone in the RT-rolled sample, some black deformation bands are located around grain boundaries, which generally result from the high dislocation density in these areas. Recrystallization tends to occur around these grain boundaries with the high dislocation density. At 10 min, as shown in Figure 7.4 (e), the recrystallized grains mainly nucleated along grain boundaries, and some basal grains shown as green ones are larger than non-basal grains, which contribute to the strengthening of the central part in the pole figure. After 70 min, more basal grains grow, and the central part of the pole figure becomes stronger (Figure 7.4 (f) and (h)). This result indicates that the preferential basal grain growth around deformation bands and grain boundaries contributes to the basal texture strengthening.

Texture evolution analysis is also conducted for the CT-rolled sample during the annealing process. As shown in Figure 7.4 (i), the main deformation structure of the CT-rolled sample in this zone is $(10\bar{1}2)$-$(01\bar{1}2)$ twin-twin interactions. At 10 min, in Figure 7.4 (j), many new grains with various orientations nucleate around the boundaries of $(10\,\bar{1}\,2)$-$(01\,\bar{1}\,2)$ twin-twin

interactions, and these recrystallized grains represent different orientations from the matrix, which contribute to the formation of a weak texture. At 70 min, more grains are generated around the twin boundaries and show a homogeneous distribution and uniform grain growth, resulting in a scattered and weak texture (Figure 7.4 (k) and (p)).

Figure 7.4 (l) shows another typical zone in the CT-rolled sample, and $(10\bar{1}2)$-$(01\bar{1}2)$ twin-twin interactions and TTWs are both located in this grain. According to Figure 7.4 (l-n), the main recrystallized sites are the boundaries of $(10\bar{1}2)$-$(01\bar{1}2)$ twin-twin interactions, and very few grains recrystallize around TTWs. The texture in this zone is scattered and weak, as shown in Figure 7.4 (n) and (p), because more non-basal grains with various orientations nucleate and grow uniformly. Therefore, unlike texture strengthening in the annealed RT-rolled sample, the texture of the CT-rolled sample becomes much weaker during the annealing process, because the recrystallization with randomized orientations and the uniform grain growth occurs around the boundaries of twin-twin interactions.

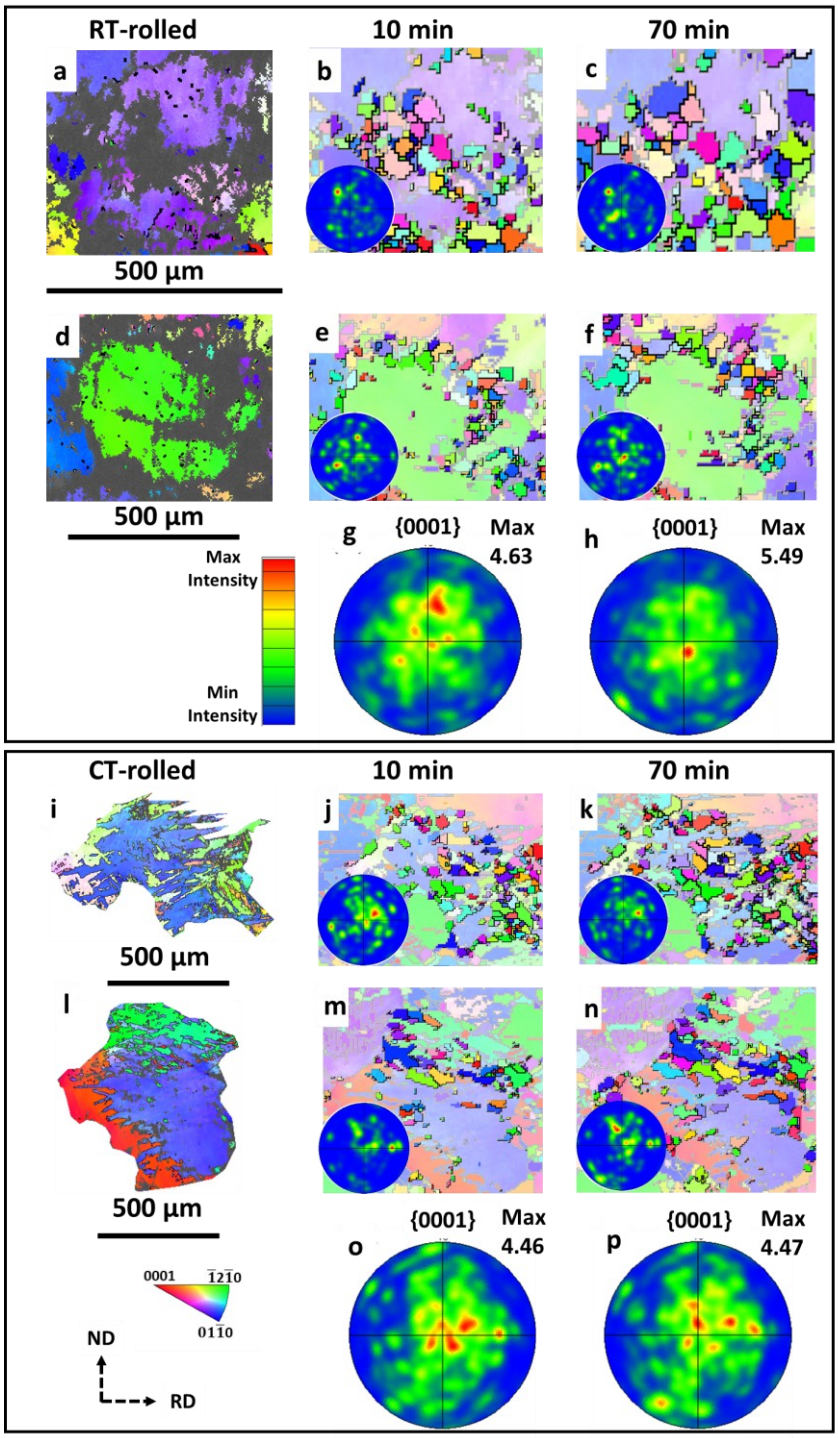

Figure 7.4 IPF maps and their corresponding {0001} pole figures of the recrystallized grains in the typical zones of the RT-rolled and CT-rolled samples during the annealing process at 300 °C for (a, d, i, l) 0, (b, e, j, m) 10, (c, f, k, n) 70 min, respectively. The {0001} pole figures of all recrystallized grains in Figure 7.3 of the RT-rolled and CT-rolled samples during the annealing process at 300 °C for (g, o) 10 and (h, p) 70 min, respectively. The unit of the colour bar is mud.

7.3.4 Typical deformation structures in the RT-rolled and CT-rolled samples

Figure 7.5 plots the microstructural analysis of the four typical zones in RT-rolled and CT-rolled samples to investigate their main deformation structures, as these deformation structures, including deformation bands and twin-twin interactions, could have a significant influence on recrystallization. In Figure 7.5 (a) and (b), Zone A and Zone B in the RT-rolled sample are plotted to show TTWs and deformation bands, respectively. In Figure 7.5 (a), a grain with $\{10\bar{1}2\}$ TTWs is plotted in Zone A. Twin variant A1 shows a misorientation of ~86° from matrix M, according to its pole figure and misorientation distribution map. In Figure 7.5 (b), some deformation bands are distributed and interacted in the matrix M. Few $\{10\bar{1}1\}$-$\{10\bar{1}2\}$ DTWs, such as twin variant B1, are located in these deformation bands, and the misorientation of these twin boundaries is ~38°. These microstructural behaviours are in good agreement with the results in the research on cold-rolled Mg alloys [14].

Figure 7.5 (c) and (d) plot the microstructure of the CT-rolled sample in Zone C and D. The main twin types in the CT-rolled sample are TTWs and $(10\bar{1}2)$-$(01\bar{1}2)$ twin-twin interactions. In Figure 7.5 (c), two twin variants C1 and C2 consume the most parts of the matrix M and interact with each other to form $(10\bar{1}2)$-$(01\bar{1}2)$ twin-twin interactions, which also contribute to the formation of fine structures. According to the {0001} pole figure, twin variants C1 and C2 are scattered and show different orientations from its matrix M. A high peak is observed near the misorientation of ~60° in the misorientation distribution map, indicating that abundant $(10\bar{1}2)$-$(01\bar{1}2)$ twin-twin interactions are formed in this zone.

In Figure 7.5 (d), the two TTW variants D1 and D2 interact to form $(10\bar{1}2)$-$(01\bar{1}2)$ twin-twin interactions in matrix M. Similar to the twin-twin interactions in Figure 7.5 (c), these two variants are located away from the centre of the pole figure and result in a scattered distribution, according to its pole figure. The two peaks with specific misorientations of ~86° and ~60° are

both high, indicating that abundant boundaries of TTWs and $(10\bar{1}2)$-$(01\bar{1}2)$ twin-twin interactions are presented in this zone.

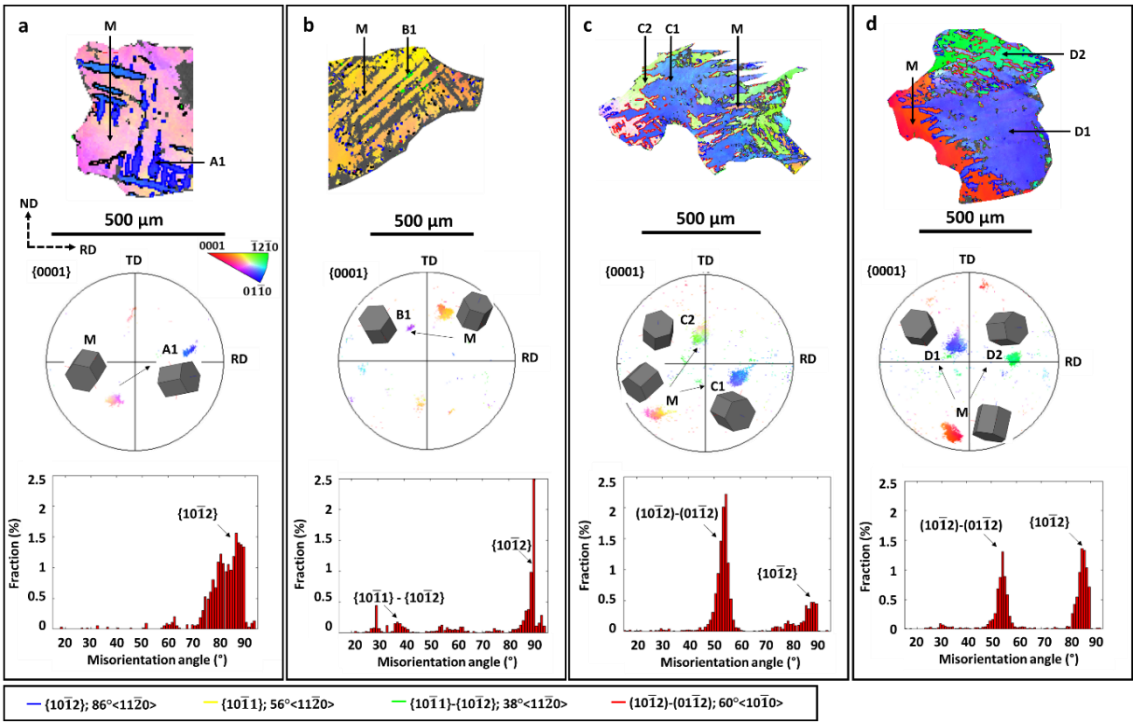

Figure 7.5 Typical zones in Figure 7.2 for the RT-rolled and CT-rolled samples, respectively: (a) Zone A, (b) Zone B in the RT-rolled sample, and (c) Zone C, (d) Zone D in the CT-rolled sample, where the first row presents the IPF maps in these zones; the second row shows their corresponding {0001} pole figures, and the hexagonal prisms are superimposed in these pole figures to present their orientations; the third row displays their misorientation distribution maps.

7.3.5 Recrystallization in different deformation structures

The main deformation structure in the CT-rolled sample is twinning including TTWs and $(10\bar{1}2)$-$(01\bar{1}2)$ twin-twin interactions. Therefore, the recrystallization sites in this sample are mainly located around these twin boundaries. As shown in Figure 7.6 (a) and (b), few recrystallized grains are observed around the TTWs, which is in agreement with the result in Ref [93, 98]. It is worth noting that very few recrystallized grains are also observed around the TTWs in the annealed RT-rolled sample, as shown in Figure 7.2 (b) and Figure 7.3 (c). Figure 7.6 (e) shows the KAM map to reflect the GND density distributions. For example, the KAM values in these TTWs are low, indicating that their GND density is low and the stored energy

is insufficient to activate recrystallization in the area. In addition, in Figure 7.6 (e) and (f), some sites with high KAM values are located in the matrix of grains, but no recrystallized grains are observed in these sites. This could be due to no typical nucleation sites near these sites.

As shown in Figure 7.6 (c) and (d), it is also rare to observe the recrystallization in these TTWs, as the KAM value is low in these twins (Figure 7.6 (g)). However, some recrystallized grains are observed in the boundaries of twin-twin interactions which show high KAM values, according to Figure 7.6 (g) and (h). In Figure 7.6 (f) and (h), the KAM value in these recrystallized grains is low, confirming that few dislocations exist in the newly formed grains. The average KAM values of recrystallized grains in the annealed grain A and grain B are 0.61° and 0.55°, which are much lower than the average KAM values of 1.28° and 1.36° in the deformed grain A and grain B, respectively.

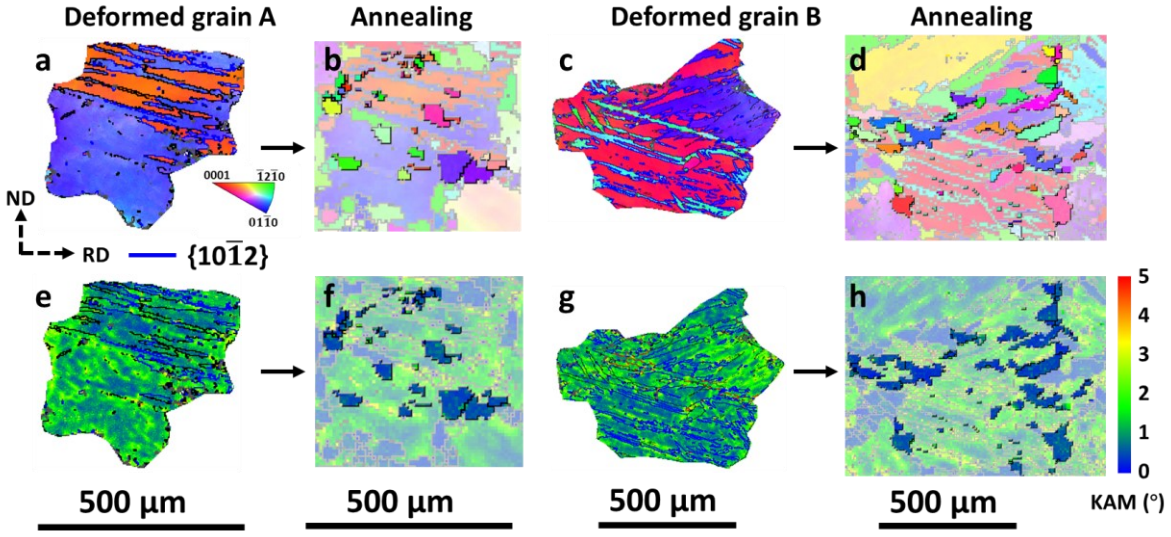

Figure 7.6 (a, b) IPF maps of the deformed and annealed grain A at 300 °C for 70 min, and (e, f) their corresponding KAM maps, respectively; (c, d) IPF maps of the deformed and annealed grain B at 300 °C for 70 min, and (g, h) their corresponding KAM maps, respectively.

Another typical deformation structure in the CT-rolled sample is (10$\bar{1}$2)-(01$\bar{1}$2) twin-twin interactions, according to Figure 7.2 (d). As shown in Figure 7.7 (a) and (b), abundant recrystallized grains are formed around these boundaries of twin-twin interactions in grain C,

resulting in significant grain refinement. In Figure 7.7 (e), the KAM value around the twin-twin interactions is high, which would provide adequate stored energy to initiate recrystallization. The average KAM value in the deformed grain C containing twin-twin interactions is 1.68° and higher than the average KAM value of 1.28° in the deformed grain A containing the single tension twin variant.

As shown in Figure 7.7 (c), both TTWs and twin-twin interactions are observed in grain D. The recrystallized grains are mainly located around the boundaries of twin-twin interactions rather than the boundaries of TTWs, which could be attributed to higher KAM values around the boundaries of twin-twin interactions than that around TTWs in Figure 7.7 (g). According to Figure 7.7 (c) and (d), TTWs are profuse and show coarse structures, while twin-twin interactions are fine and dense. The dislocation distributions in TTWs and twin-twin interactions are also different. Although there are few sites with high KAM values in TTWs, these sites are scattered and away from the twin boundaries. However, abundant sites with high KAM values are distributed around the twin-twin interactions and close to the twin boundaries and interacting sites. After the annealing process, very few recrystallized grains are found around the twin boundaries of TTWs, while abundant recrystallized grains are formed near the boundaries of twin-twin interactions. The difference of recrystallization in these two areas of grain D may also be related to the different orientations of these areas, as the different orientations could affect the dislocation activities in these areas.

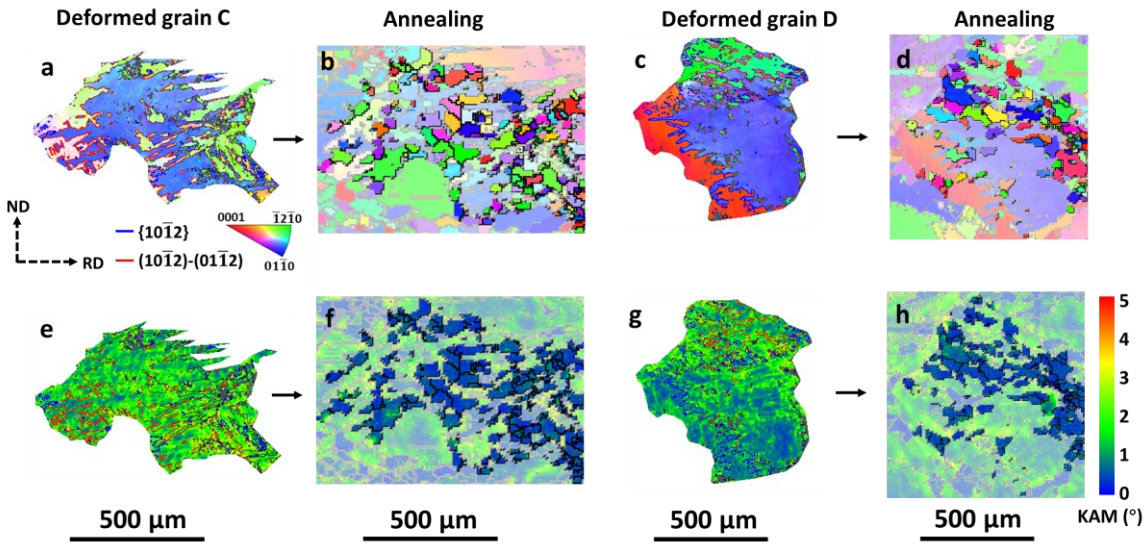

Figure 7.7 (a, b) IPF maps of the deformed and annealed grain C at 300 °C for 70 min, and (e, f) their corresponding KAM maps, respectively; (c, d) IPF maps of the deformed and annealed grain D at 300 °C for 70 min, and (g, h) their corresponding KAM maps, respectively.

Recrystallization in the annealed RT-rolled sample mainly occurs around deformation bands including the deformed areas near grain boundaries (Figure 7.3). Two typical zones are selected to gain an in-depth analysis of their recrystallization mechanisms. In Figure 7.8 (a) and (e), deformation bands are observed in Zone E, and the KAM value in the area is high, resulting in active recrystallization and a large recrystallized area in Figure 7.8 (b) and (f). Similarly, the recrystallized grains in Zone F are situated along the grain boundaries, and the recrystallized area is small, as shown in Figure 7.8 (c) and (d). This would be attributed to the high KAM value around deformation bands including the areas near grain boundaries (Figure 7.8 (g) and (h)), which could promote the recrystallization in these sites. The average KAM values in deformed Zone E and Zone F are 1.22° and 1.04°, which are both higher than the average KAM values of 0.52° and 0.53° in recrystallized grains of these two zones after annealing, respectively.

As shown in Figure 7.8 (e) and (g), the sites with high KAM values are close to the deformation bands and grain boundaries, while the KAM values are low inside the grains. After the

annealing process, the recrystallized grains are located near these boundaries, and very few recrystallized grains are observed inside the original grain. This result indicates that high KAM values near these boundaries are essential to activate recrystallization.

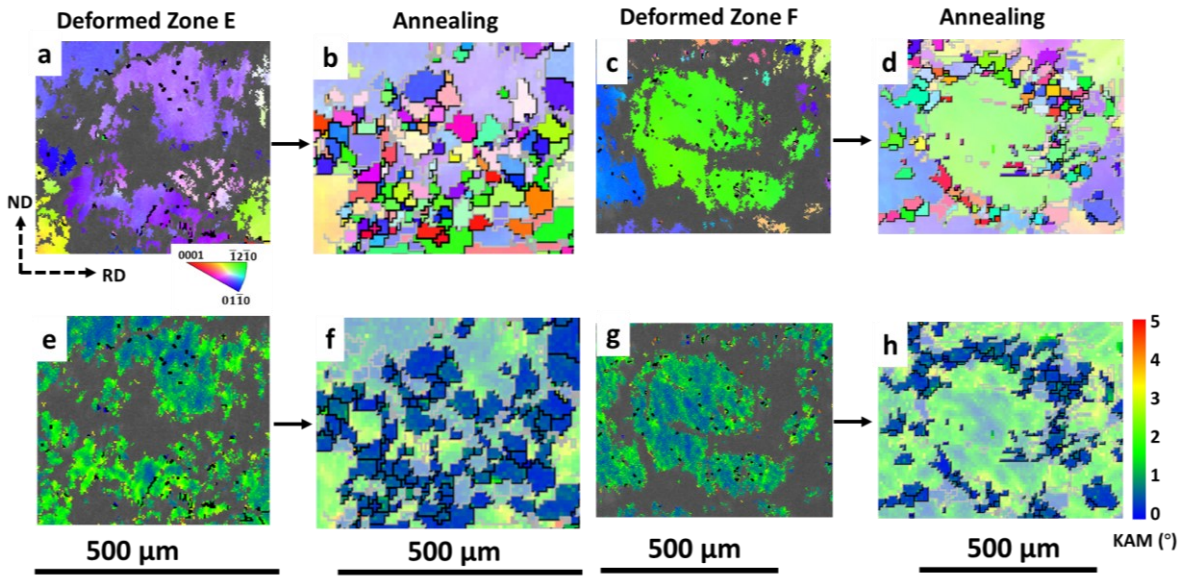

Figure 7.8 (a, b) IPF maps of deformed and annealed Zone E at 300 °C for 70 min, and (e, f) their corresponding KAM maps, respectively; (c, d) IPF maps of deformed and annealed Zone F at 300 °C for 70 min, and (g, h) their corresponding KAM maps, respectively.

7.3.6 Grain size evolution during the annealing process

The grain size information of the RT-rolled and CT-rolled samples during the annealing process is summarized in Figure 7.9. In Figure 7.9 (a), the average grain size decreases with a diminishing rate during the annealing process. In the initial stage, the recrystallization starts to occur, resulting in a fast decrease of the average grain size, and then the decrease of the average grain size approaches a stable state. The average grain size of the CT-rolled sample is smaller than that of the RT-rolled sample in the annealing process, indicating that the grain refinement in recrystallization of the annealed CT-rolled sample is more effective than that of the annealed RT-rolled sample.

The grain size distribution of the RT-rolled and CT-rolled samples in the annealing process at 110 min is plotted in Figure 7.9 (b). Compared to the annealed RT-rolled sample, the grain size distribution of the annealed CT-rolled sample, especially the small grains below the average grain size, is more homogenous, and more fine grains are observed. The fine and homogenous microstructure in the annealed CT-rolled sample could be attributed to its active recrystallization and uniform grain growth around the twin boundaries and twin-twin interactions. In addition, compared with deformation bands in the RT-rolled sample, twin boundaries in the CT-rolled sample are distributed more homogenously, resulting in more active twin recrystallization and the formation of a more homogenous microstructure.

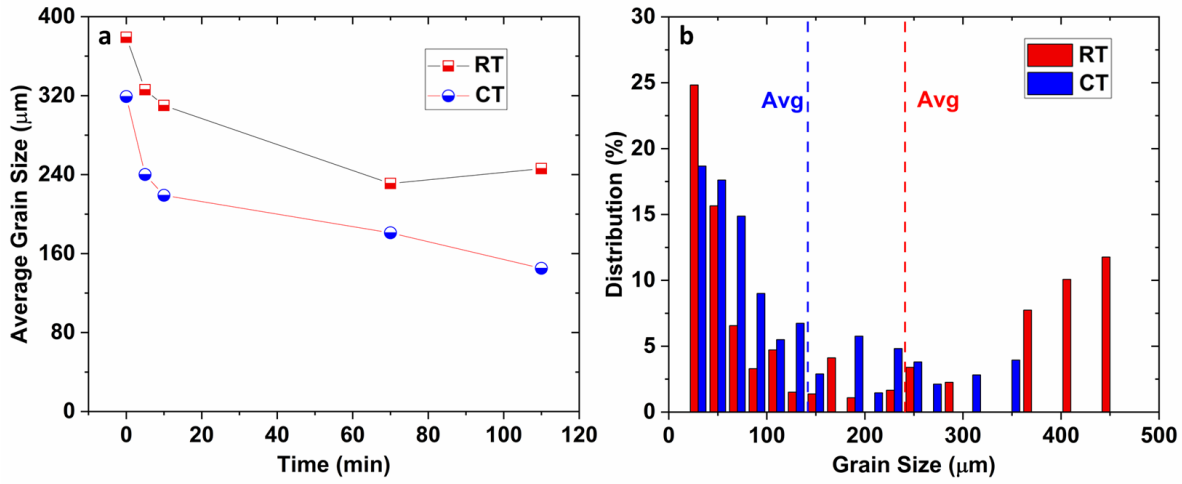

Figure 7.9 (a) Grain size evolution of the RT-rolled and CT-rolled samples during the annealing process at 300 ℃, (b) grain size distribution in the RT-rolled and CT-rolled samples after annealing at 300 ℃ for 110 min.

7.4 Discussion

7.4.1 Illustration of recrystallization mechanisms in the annealed RT-rolled and CT-rolled samples

Figure 7.10 (a) and (b) plot the schematic of deformation mechanisms for Mg alloy AZ31 in the RT-rolling and CT-rolling processes, based on the experimental observations. As shown in

Figure 7.10 (a), initial samples show the homogenous microstructure with a low dislocation density. After the rolling process, the main deformation microstructures in the RT-rolled sample are deformation bands and few twins including $\{10\bar{1}2\}$ TTWs and $\{10\bar{1}1\}$-$\{10\bar{1}2\}$ DTWs, this is consistent with the results reported in cold-rolled Mg alloys samples [14]. However, more twins including $(10\bar{1}2)$- $(01\bar{1}2)$ twin-twin interactions are generated in the CT-rolled sample. The reason for the active twin behaviours in the cryogenic deformation is discussed in Section 6.4.2.

Figure 7.10 (c-e) plots the schematic of microstructure evolution in the subsequent annealing process. In the initial stage, few static recrystallized (SRXed) grains mainly nucleate around the deformation bands including the deformed areas near grain boundaries in the RT-rolled sample, and some SRXed grains nucleate around the twin boundaries of the CT-rolled sample, as shown in Figure 7.10 (c). With increasing annealing time, in Figure 7.10 (d), more SRXed grains in the RT-rolled sample nucleate around the deformation bands, and oriented grain growth also occurs, resulting in texture strengthening. However, most recrystallized grains in the CT-rolled sample are generated around the twin boundaries, especially $(10\bar{1}2)$-$(01\bar{1}2)$ twin-twin interactions, which contribute to weakening the texture. In addition, due to the more homogenous distribution of twin boundaries than deformation bands, the microstructure of the annealed CT-rolled sample during the annealing process is more homogenous and finer than that of the annealed RT-rolled sample. Finally, the nucleation and growth of the SRXed grains become stable, as shown in Figure 7.10 (e).

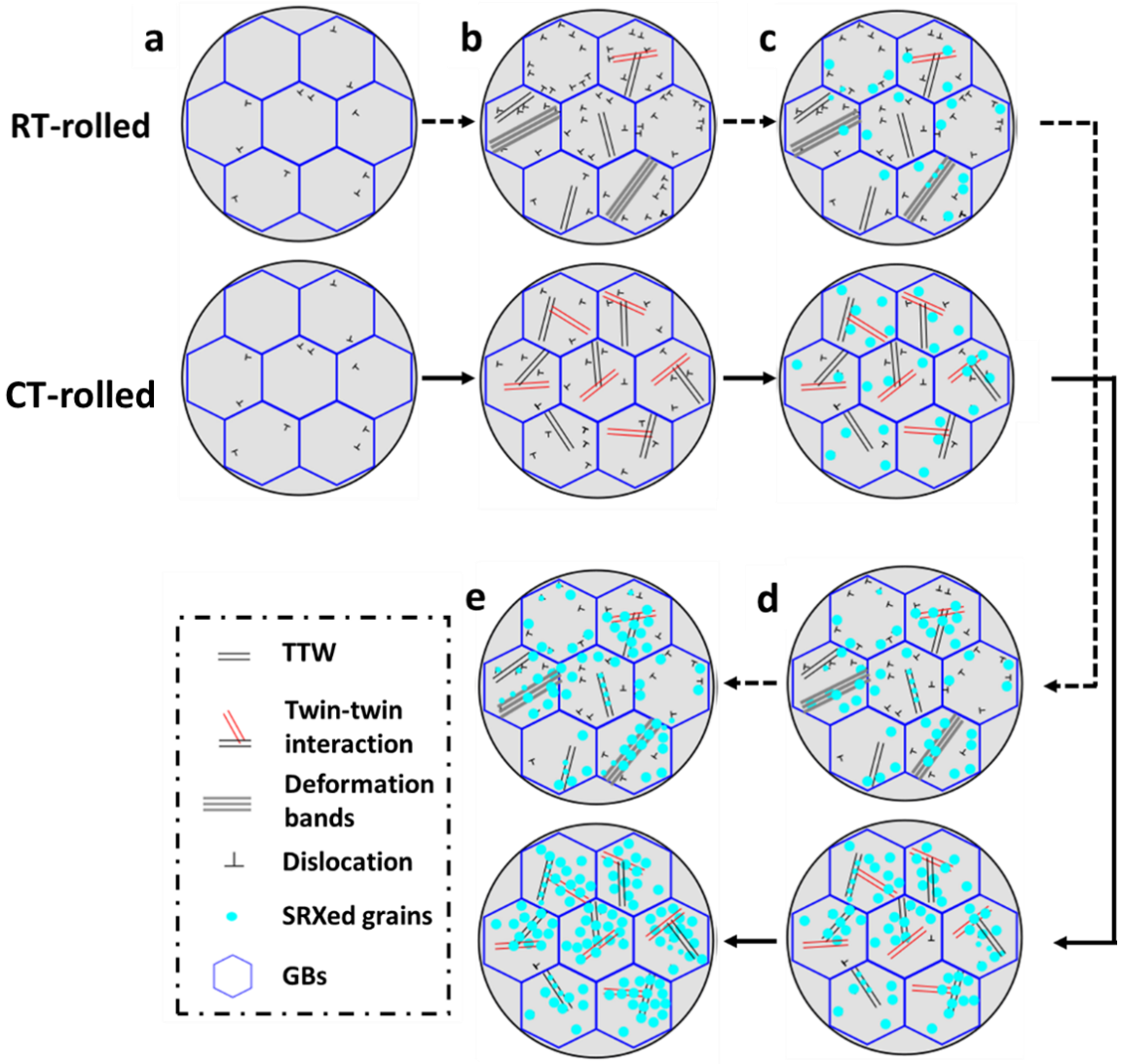

Figure 7.10 Schematic of mechanisms in the RT-rolling and CT-rolling with subsequent annealing process: (a) the microstructure of initial Mg alloy AZ31; (b) the microstructure of Mg alloy AZ31 after the RT-rolling and CT-rolling; (c) the few static recrystallized (SRXed) grains nucleate at the initial stage of annealing process; (d) the fast generation of SRXed grains; (e) the stabilized SRXed grain generations in the recrystallization.

7.4.2 Recrystallization and texture evolution of the RT-rolled sample during the subsequent annealing process

The main deformation structures in the RT-rolled Mg alloy AZ31 are deformation bands, which would become the main recrystallized sites in the annealing process [139]. As shown in Figure 7.8, abundant dislocations accumulate around the deformation bands including the deformed

areas near grain boundaries, providing enough stored energy to induce the nucleation of recrystallization.

Texture strengthening is observed during the recrystallization of the annealed RT-rolled Mg alloy AZ31, and it would be attributed to the effects of deformation bands including the deformed areas near grain boundaries. According to Figure 7.4, the texture is scattered during the initial nucleation stage, but it becomes stronger when the grains grow. The strong basal texture in the annealed RT-rolled sample would be attributed to the oriented and inhomogeneous grain growth around deformation bands, i.e. basal grains grow much faster than non-basal grains near deformation bands or grain boundaries. The reason could be that the recrystallized grains generally inherit the orientation of matrix grains which were basal orientations in most cases [74]. The preferential basal grain growth could also be related to the anisotropic grain boundary energy and mobility in Mg alloy AZ31 [13]. To clarify the mechanisms, it may require the detailed *in-situ* testing to observe the evolution of basal and non-basal grains during recrystallization. This preferential grain growth was also observed in the recrystallization near deformation bands in the cold-rolled Mg-0.4Zn alloy, resulting in the formation of the strong basal texture [91]. Although some twins, including TTWs, are observed in the RT-rolled sample in Figure 7.3, it is rare to observe recrystallization around these twin boundaries, which make negligible contributions to the texture [93, 140]. Therefore, the main recrystallization sites in the RT-rolled sample are deformation bands, and it is reasonable to form a strong texture when recrystallization occurs in these sites.

7.4.3 Recrystallization and texture evolution of the CT-rolled sample during the subsequent annealing process

For the CT-rolled sample, abundant twins including TTWs and twin-twin interactions formed. It is rare to observe recrystallization around TTWs, because the KAM value around the TTWs is low, which cannot provide the sufficient stored energy to activate recrystallization, as shown

in Figure 7.6. The low KAM value around TTWs is attributed to the abundant slips which can easily transmit across TTW boundaries to effectively relieve the local stress and dislocation pile-ups [95]. Furthermore, TTWs are suggested to be profuse and show coarse structures, as TTWs could completely absorb the dislocations in the twin boundary to promote twin propagation [94]. As a result, the twin shear localization and dislocation accumulation are limited [93]. However, according to Figure 7.7, the dislocation slips are easily pinned and accumulate around these interacting twin boundaries of twin-twin interactions [61, 65], resulting in high KAM values around these twin boundaries. Unlike coarse TTWs, twin-twin interactions are fine and dense, which could block the dislocation slips easily. As it is difficult for twins to transmit across the twin boundaries, twin propagation can be prevented by other twin boundaries [63], resulting in fine structures. Instead, twin-twin boundaries form and contain boundary dislocations [61]. As a result, these interacting twin boundaries with high KAM values would provide abundant sites for twin recrystallization [113].

Unlike texture strengthening in the RT-rolled sample during the annealing process, texture weakening is observed in the annealed CT-rolled sample. This would result from the active recrystallization around twin boundaries, especially the boundaries of twin-twin interactions in the annealed CT-rolled sample. In Figure 7.4, as the annealing time increases, more recrystallized grains with randomised orientations are generated around twin-twin interactions, and the orientations of these grains are different from the matrix and away from the centre of the pole figure. This could be attributed to the random orientations of twin variants in twin-twin interactions, and recrystallized grains inherit the random orientations of these twin variants [96], resulting in a weak texture. In addition, the basal and non-basal grains in the twin recrystallization of the CT-rolled sample grow more uniformly, compared to the oriented grain growth in deformation bands of the RT-rolled sample. Therefore, the random new orientations and uniform grain growth of recrystallized grains can result in texture weakening in the

annealed CT-rolled sample. This also explains why the weak texture and fine grains form in the cryogenic-hot deformed sample in Figure 4.3-5 (Chapter 4), because recrystallization near abundant twin-twin interactions of the CT-deformed sample results in forming random orientations and uniform grain growth. However, the recrystallization near deformation bands contributes to the formation of coarse grains and a strong texture in the direct-HD and RT-HD samples in Figure 4.3-5, due to the oriented basal grain growth.

It is worth noting that the annealed CT-rolled sample shows a more homogenous microstructure with a finer average grain size than the annealed RT-rolled sample. In the RT-rolled sample, deformation bands are the main recrystallization nucleation sites, but the density of the deformation bands is low in the Mg alloy AZ31 [82], and they are not distributed homogeneously, especially inside grains, as shown in Figure 7.2. In addition, the recrystallization and grain growth in deformation bands including the deformed areas near grain boundaries are oriented and inhomogeneous. Whereas the density of twins, especially twin-twin interactions, is high in the CT-rolled sample, and they are distributed homogenously in each grain. More active recrystallization and homogenous grain growth in these twin boundaries would contribute to the formation of the more homogenous microstructure with finer grains [15]. The homogenous and fine microstructure could also contribute to weakening the texture in the annealed CT-rolled sample. These microstructural behaviours in the annealed CT-rolled sample are also consistent with those in the CT-HD samples after the cryogenic-hot deformation process in Chapter 4. However, the grain refinement is more significant in the cryogenic-hot deformation process, this could be attributed to the more effective grain refinement in dynamic recrystallization than that in static recrystallization [7].

7.5 Summary

In this chapter, the RT-rolling and the CT-rolling with subsequent annealing processes are studied to investigate the recrystallization mechanisms in various deformation structures, namely, deformation bands and twinning. The evolutions of grain orientations and KAM values during recrystallization are analysed using the *quasi-in-situ* EBSD method. The following conclusions are drawn:

(1) Substantial twin boundaries, especially twin-twin interactions, in the CT-rolled sample provide abundant nucleation sites for recrystallization, which contribute to the formation of a weak texture and finer grain sizes in the annealed CT-rolled sample.

(2) Texture weakening in the annealed CT-rolled sample results from its active recrystallization and homogeneous grain growth around twin-twin interactions in which randomly oriented grains are generated.

(3) The nucleation and growth of SRXed grains in the annealed RT-rolled sample mainly occur around the deformation bands including the deformed areas near grain boundaries, resulting in texture strengthening. Texture strengthening is attributed to the oriented and inhomogeneous grain growth around deformation bands, as basal grains grow much faster than non-basal grains.

(4) Twin-twin interactions show the fine structures and high KAM values, which provide sufficient stored energy for active recrystallization, while TTWs are coarse and difficult to accumulate dislocations, resulting in fewer recrystallized grains.

8 Conclusions and future work

8.1 Conclusions

Mg alloys are promising lightweight materials to reduce weight of car body to reduce energy consumption and air pollution, but their ductility and strength are limited due to the coarse grains and strong basal texture. In order to deal with these problems, this research proposed a novel cryogenic-hot deformation method to refine the grains and weaken the texture in Mg alloy AZ31, thus improving its ductility and strength. Then, the deformation behaviour at cryogenic and room temperature and the subsequent recrystallization mechanisms were investigated. This is helpful to improve the applications of Mg alloys in automotive industries. Further conclusions are summarized in the following four subsections.

8.1.1 A novel cryogenic-hot deformation method to achieve fine grains and a weak texture in Mg alloys

The novel cryogenic-hot deformation method was developed to achieve significant grain refinement and texture weakening, resulting in the high ductility and strength of Mg alloy AZ31. The homogenous microstructure with fine grains and a weak texture in the cryogenic-hot deformed sample would be attributed to the active dynamic recrystallization around twin-twin interactions. However, recrystallization mainly occurred near deformation bands in the direct-hot-deformed and RT-hot-deformed samples, resulting in the formation of coarse grains and a strong texture.

8.1.2 Deformation mechanisms at cryogenic and room temperature

More twins, particularly twin-twin interactions, were observed in the CT-deformed sample than in the RT-deformed sample, which contributed to the higher hardening rate in the CT-deformation due to the Hall-Petch strengthening of twin boundaries and direct hardening effects of twin-twin interactions against twins. While lower average KAM values were shown

in the CT-deformed sample than in the RT-deformed sample, indicating that twin boundary hardening could be more effective than stored dislocation density hardening. The abundant twin-twin interactions in the CT-deformed sample tended to accumulate dislocations and contributed to forming the weak and scattered texture. The active twinning behaviour in the CT-deformation could be attributed to the limited dislocation slips and significant local stress concentrations.

8.1.3 Evolution of twin-twin interactions, twinning sequence and deformation bands

Deformation bands are the main deformation structures in the RT-rolling process, while twin-twin interactions and twinning sequence dominate in the CT-rolling process. In the RT-rolling process, $\{10\bar{1}1\}$- $\{10\bar{1}2\}$ DTWs were generated during the initial process and then transferred into deformation bands with increasing rolling reductions. However, abundant twins, starting from $\{10\bar{1}2\}$ TTWs to twin-twin interactions and twinning sequence, were generated during the CT-rolling process. Besides, a rarely observed twinning sequence, namely primary twin-twin interaction → secondary twin-twin interaction, with a 45° $<20\bar{2}\bar{1}>$ misorientation peak, was observed in the CT-rolled sample. This could be due to the more significant local stress concentrations in the CT-rolling process.

8.1.4 Recrystallization mechanisms in twin-twin interactions and deformation bands

To study the recrystallization mechanisms near deformation bands and twin-twin interactions, the microstructure evolution of the RT-rolled and CT-rolled samples during the annealing process was investigated with the *quasi-in-situ* EBSD. The recrystallized grains in the annealed RT-rolled sample mainly occurred around the deformation bands, resulting in texture strengthening. This was attributed to the oriented and inhomogeneous grain growth around deformation bands, as the growth of basal grains was faster than that of non-basal grains. However, the main recrystallized sites in the annealed CT-rolled sample were around twin

boundaries, mainly twin-twin interactions, resulting in the homogeneous grain growth with randomly oriented grains. Therefore, the weak texture and the fine grain size were generated in the annealed CT-rolled sample.

8.2 Suggestions for future work

8.2.1 The improvement of the cryogenic-hot deformation method

In this research, a novel and effective cryogenic-hot deformation method to refine the grains and weaken the texture was achieved. To achieve finer grains, the initial material can be fine-grained samples, which would be helpful to obtain ultra-fine grains after this process. Besides, it is unclear whether it is feasible to apply the cryogenic-hot deformation method to other Mg alloys to achieve fine grains and weak textures. It will be a promising topic to broaden the application of cryogenic deformation in other Mg alloys. The novel process combining cryogenic and hot deformation is expected to be applied in industrial work, such as forging processes, so it can optimize microstructures and improve mechanical properties of the Mg alloy components.

8.2.2 The modelling of cryogenic deformation

There are extensive experimental results about the cryogenic deformation of Mg alloys in this work, but it lacks modelling studies to explain the deformation behaviour systematically. Crystal plasticity finite-element (CPFE) modelling would help explain the twinning and dislocation slip behaviours at different temperatures. For example, the mechanisms of twin nucleation and the formation of twin-twin interactions at cryogenic temperature could be related to the local stress and dislocation density. These mechanisms can be systematically revealed by combining CPFE modelling and EBSD analysis.

8.2.3 Investigation of grain size and texture effects on deformation mechanisms in Mg alloys at cryogenic temperature

The deformation mechanisms in the as-cast coarse-grained Mg alloy AZ31 were investigated in this thesis, and the ductility (strain to failure) showed a slight decrease in compression tests at cryogenic temperature compared to room temperature. As the grain size also has a significant influence on twinning and dislocation, it is worth investigating the effects of grain size on deformation mechanisms at cryogenic temperature. Therefore, the relationship between temperatures effects with grain size effects can be investigated. Furthermore, it could be possible to find a way to improve the ductility of Mg alloys at cryogenic temperature with optimal grain sizes. This research will broaden the application of cryogenic deformation in Mg alloys.

Reference

[1] E. Commission, CO_2 emission performance standards for cars and vans. https://ec.europa.eu/clima/policies/transport/vehicles/regulation_en, 2020 [Cited 12 July 2021]).

[2] T.N. ARCHIVES, The Passenger Car (Fuel Consumption and CO2 Emissions Information) Regulations 2001. http://www.legislation.gov.uk/uksi/2001/3523/schedule/1/made, 2001 [Cited 12 July 2021]).

[3] W.J. Joost, P.E. Krajewski, Towards magnesium alloys for high-volume automotive applications, Scripta Materialia 128 (2017) 107-112.

[4] H. Watarai, Trend of Research and Development for Magnesium Alloys-Reducing the Weight of Structural Materialsin Motor Vehicles, NISTEP Science & Technology Foresight Center, 2006.

[5] T.M. Pollock, Weight Loss with Magnesium Alloys, Science 328(5981) (2010) 986-987.

[6] S.C. Davis, and Robert G. Boundy., Transportation Energy Data Book: Edition 37.2, Oak Ridge National Laboratory (2019).

[7] C. Bettles, M. Barnett, Advances in wrought magnesium alloys: fundamentals of processing, properties and applications, Elsevier2012.

[8] Q. Li, C.A. Rottmair, R.F. Singer, CNT reinforced light metal composites produced by melt stirring and by high pressure die casting, Composites Science and Technology 70(16) (2010) 2242-2247.

[9] B.-Y. Liu, F. Liu, N. Yang, X.-B. Zhai, L. Zhang, Y. Yang, B. Li, J. Li, E. Ma, J.-F. Nie, Z.-W. Shan, Large plasticity in magnesium mediated by pyramidal dislocations, Science 365(6448) (2019) 73-75.

[10] Z. Wu, R. Ahmad, B. Yin, S. Sandlöbes, W.A. Curtin, Mechanistic origin and prediction of enhanced ductility in magnesium alloys, Science 359(6374) (2018) 447-452.

[11] Z. Zeng, N. Stanford, C.H.J. Davies, J.-F. Nie, N. Birbilis, Magnesium extrusion alloys: a review of developments and prospects, International Materials Reviews 64(1) (2018) 27-62.

[12] K. Huang, R.E. Logé, A review of dynamic recrystallization phenomena in metallic materials, Materials & Design 111 (2016) 548-574.

[13] J.J. Bhattacharyya, S.R. Agnew, G. Muralidharan, Texture enhancement during grain growth of magnesium alloy AZ31B, Acta Materialia 86 (2015) 80-94.

[14] M.R. Barnett, M.D. Nave, C.J. Bettles, Deformation microstructures and textures of some cold rolled Mg alloys, Materials Science and Engineering: A 386(1-2) (2004) 205-211.
[15] S.Q. Zhu, H.G. Yan, X.Z. Liao, S.J. Moody, G. Sha, Y.Z. Wu, S.P. Ringer, Mechanisms for enhanced plasticity in magnesium alloys, Acta Materialia 82 (2015) 344-355.
[16] D. Guan, W.M. Rainforth, J. Gao, J. Sharp, B. Wynne, L. Ma, Individual effect of recrystallisation nucleation sites on texture weakening in a magnesium alloy: Part 1- double twins, Acta Materialia 135 (2017) 14-24.
[17] A. Levinson, R.K. Mishra, R.D. Doherty, S.R. Kalidindi, Influence of deformation twinning on static annealing of AZ31 Mg alloy, Acta Materialia 61(16) (2013) 5966-5978.
[18] Z.W. Huang, S.B. Jin, H. Zhou, Y.S. Li, Y. Cao, Y.T. Zhu, Evolution of twinning systems and variants during sequential twinning in cryo-rolled titanium, International Journal of Plasticity (2018).
[19] M.A. Meyers, O. Vöhringer, V.A. Lubarda, The onset of twinning in metals: a constitutive description, Acta Materialia 49(19) (2001) 4025-4039.
[20] K. Zhang, Z. Shao, C.S. Daniel, M. Turski, C. Pruncu, L. Lang, J. Robson, J. Jiang, A comparative study of plastic deformation mechanisms in room-temperature and cryogenically deformed magnesium alloy AZ31, Materials Science and Engineering: A 807 (2021).
[21] K. Zhang, J.-H. Zheng, Y. Huang, C. Pruncu, J. Jiang, Evolution of twinning and shear bands in magnesium alloys during rolling at room and cryogenic temperature, Materials & Design 193 (2020).
[22] K. Zhang, Z. Shao, J. Jiang, Effects of twin-twin interactions and deformation bands on the nucleation of recrystallization in AZ31 magnesium alloy, Materials & Design 194 (2020).
[23] K. Zhang, Z. Shao, J. Jiang, Achieving fine grains and a weak texture in magnesium alloy AZ31 by cryogenic-hot deformation, Acta Materialia (Submitted) (2020).
[24] R. Von Mises, Mechanics of the ductile form changes of crystals, Zeitschrift Fur Angewandte Mathematik Und Mechanik 8 (1928) 161-185.
[25] R. Sánchez-Martín, M.T. Pérez-Prado, J. Segurado, J. Bohlen, I. Gutiérrez-Urrutia, J. Llorca, J.M. Molina-Aldareguia, Measuring the critical resolved shear stresses in Mg alloys by instrumented nanoindentation, Acta Materialia 71 (2014) 283-292.
[26] M. Lentz, M. Risse, N. Schaefer, W. Reimers, I.J. Beyerlein, Strength and ductility with {1011} - {1012} double twinning in a magnesium alloy, Nat Commun 7 (2016) 11068.
[27] M.R. Barnett, Twinning and the ductility of magnesium alloys Part I: “Tension” twins, Materials Science and Engineering: A 464(1-2) (2007) 1-7.

[28] Z. Wu, W.A. Curtin, The origins of high hardening and low ductility in magnesium, Nature 526 (2015) 62.
[29] S. Sandlöbes, S. Zaefferer, I. Schestakow, S. Yi, R. Gonzalez-Martinez, On the role of non-basal deformation mechanisms for the ductility of Mg and Mg–Y alloys, Acta Materialia 59(2) (2011) 429-439.
[30] S. Balasubramanian, L. Anand, Plasticity of initially textured hexagonal polycrystals at high homologous temperatures: application to titanium, Acta Materialia 50(1) (2002) 133-148.
[31] M.R. Barnett, Twinning and the ductility of magnesium alloys Part II. "Contraction" twins, Materials Science and Engineering: A 464(1-2) (2007) 8-16.
[32] S.R. Agnew, M.H. Yoo, C.N. Tomé, Application of texture simulation to understanding mechanical behavior of Mg and solid solution alloys containing Li or Y, Acta Materialia 49(20) (2001) 4277-4289.
[33] C. Guo, R. Xin, Y. Xiao, G. Liu, Q. Liu, Observation and analysis of the coexistence of two "opposite" twin modes in a Mg-Al-Zn alloy, Materials & Design 102 (2016) 196-201.
[34] C.M. Cepeda-Jiménez, J.M. Molina-Aldareguia, M.T. Pérez-Prado, Origin of the twinning to slip transition with grain size refinement, with decreasing strain rate and with increasing temperature in magnesium, Acta Materialia 88 (2015) 232-244.
[35] A. Chapuis, J.H. Driver, Temperature dependency of slip and twinning in plane strain compressed magnesium single crystals, Acta Materialia 59(5) (2011) 1986-1994.
[36] M.R. Barnett, Twinning and the ductility of magnesium alloys: Part I: "Tension" twins, Materials Science and Engineering: A 464(1) (2007) 1-7.
[37] T.B. Britton, F.P.E. Dunne, A.J. Wilkinson, On the mechanistic basis of deformation at the microscale in hexagonal close-packed metals, Proceedings of the Royal Society A: Mathematical, Physical and Engineering Science 471(2178) (2015).
[38] S.-G. Hong, S.H. Park, C.S. Lee, Role of {10–12} twinning characteristics in the deformation behavior of a polycrystalline magnesium alloy, Acta Materialia 58(18) (2010) 5873-5885.
[39] Z.R. Zeng, M.Z. Bian, S.W. Xu, C.H.J. Davies, N. Birbilis, J.F. Nie, Texture evolution during cold rolling of dilute Mg alloys, Scripta Materialia 108 (2015) 6-10.
[40] D.W. Brown, S.R. Agnew, M.A.M. Bourke, T.M. Holden, S.C. Vogel, C.N. Tomé, Internal strain and texture evolution during deformation twinning in magnesium, Materials Science and Engineering: A 399(1-2) (2005) 1-12.

[41] M.D. Nave, M.R. Barnett, Microstructures and textures of pure magnesium deformed in plane-strain compression, Scripta Materialia 51(9) (2004) 881-885.
[42] A. Serra, D. Bacon, R. Pond, Twins as barriers to basal slip in hexagonal-close-packed metals, Metallurgical and materials transactions A 33(13) (2002) 809-812.
[43] F. Wang, S.R. Agnew, Dislocation transmutation by tension twinning in magnesium alloy AZ31, International Journal of Plasticity 81 (2016) 63-86.
[44] P. Cizek, M.R. Barnett, Characteristics of the contraction twins formed close to the fracture surface in Mg–3Al–1Zn alloy deformed in tension, Scripta Materialia 59(9) (2008) 959-962.
[45] J.W. Christian, S. Mahajan, Deformation twinning, Progress in Materials Science 39(1) (1995) 1-157.
[46] Z.R. Zeng, Y.M. Zhu, R.L. Liu, S.W. Xu, C.H.J. Davies, J.F. Nie, N. Birbilis, Achieving exceptionally high strength in Mg 3Al 1Zn-0.3Mn extrusions via suppressing intergranular deformation, Acta Materialia 160 (2018) 97-108.
[47] E. Hall, The deformation and ageing of mild steel: III discussion of results, Proceedings of the Physical Society. Section B 64(9) (1951) 747.
[48] N. Petch, The cleavage strength of polycrystals, Journal of the Iron and Steel Institute 174 (1953) 25-28.
[49] W.D. Callister, D.G. Rethwisch, Materials science and engineering, John wiley & sons NY2011.
[50] N.J. Petch, The ductile-brittle transition in the fracture of α-iron: I, The Philosophical Magazine: A Journal of Theoretical Experimental and Applied Physics 3(34) (1958) 1089-1097.
[51] J. Koike, T. Kobayashi, T. Mukai, H. Watanabe, M. Suzuki, K. Maruyama, K. Higashi, The activity of non-basal slip systems and dynamic recovery at room temperature in fine-grained AZ31B magnesium alloys, Acta Materialia 51(7) (2003) 2055-2065.
[52] M.R. Barnett, Z. Keshavarz, A.G. Beer, D. Atwell, Influence of grain size on the compressive deformation of wrought Mg–3Al–1Zn, Acta Materialia 52(17) (2004) 5093-5103.
[53] A. Jain, O. Duygulu, D.W. Brown, C.N. Tomé, S.R. Agnew, Grain size effects on the tensile properties and deformation mechanisms of a magnesium alloy, AZ31B, sheet, Materials Science and Engineering: A 486(1-2) (2008) 545-555.

[54] T. Mukai, M. Yamanoi, H. Watanabe, K. Ishikawa, K. Higashi, Effect of Grain Refinement on Tensile Ductility in ZK60 Magnesium Alloy under Dynamic Loading, MATERIALS TRANSACTIONS 42(7) (2001) 1177-1181.

[55] N.J. Petch, E. Wright, The plasticity and cleavage of polycrystalline beryllium II. The cleavage strength and ductility transition temperature, Proceedings of the Royal Society of London. A. Mathematical and Physical Sciences 370(1740) (1980) 29-39.

[56] AIST, Development of a New Rolling Process for Commercial Magnesium Alloy Sheets with High Room-temperature Formability. https://www.aist.go.jp/aist_e/list/latest_research/2010/20100217/20100217.html, 2010).

[57] A. Jain, S.R. Agnew, Modeling the temperature dependent effect of twinning on the behavior of magnesium alloy AZ31B sheet, Materials Science and Engineering: A 462(1-2) (2007) 29-36.

[58] M.A. Steiner, J.J. Bhattacharyya, S.R. Agnew, The origin and enhancement of {0001}〈112¯0〉 texture during heat treatment of rolled AZ31B magnesium alloys, Acta Materialia 95 (2015) 443-455.

[59] U.M. Chaudry, K. Hamad, J.-G. Kim, On the ductility of magnesium based materials: A mini review, Journal of Alloys and Compounds 792 (2019) 652-664.

[60] W.J. Kim, J.B. Lee, W.Y. Kim, H.T. Jeong, H.G. Jeong, Microstructure and mechanical properties of Mg–Al–Zn alloy sheets severely deformed by asymmetrical rolling, Scripta Materialia 56(4) (2007) 309-312.

[61] Q. Yu, J. Wang, Y. Jiang, R.J. McCabe, N. Li, C.N. Tomé, Twin–twin interactions in magnesium, Acta Materialia 77 (2014) 28-42.

[62] M. Arul Kumar, M. Gong, I.J. Beyerlein, J. Wang, C.N. Tomé, Role of local stresses on co-zone twin-twin junction formation in HCP magnesium, Acta Materialia 168 (2019) 353-361.

[63] M. Gong, S. Xu, Y. Jiang, Y. Liu, J. Wang, Structural characteristics of {1¯012} non-cozone twin-twin interactions in magnesium, Acta Materialia 159 (2018) 65-76.

[64] H. El Kadiri, J. Kapil, A.L. Oppedal, L.G. Hector, S.R. Agnew, M. Cherkaoui, S.C. Vogel, The effect of twin–twin interactions on the nucleation and propagation of twinning in magnesium, Acta Materialia 61(10) (2013) 3549-3563.

[65] L. Jiang, J.J. Jonas, A.A. Luo, A.K. Sachdev, S. Godet, Influence of {10-12} extension twinning on the flow behavior of AZ31 Mg alloy, Materials Science and Engineering: A 445-446 (2007) 302-309.

[66] Q. Ma, H. El Kadiri, A.L. Oppedal, J.C. Baird, B. Li, M.F. Horstemeyer, S.C. Vogel, Twinning effects in a rod-textured AM30 Magnesium alloy, International Journal of Plasticity 29 (2012) 60-76.

[67] L. Jiang, J.J. Jonas, A.A. Luo, A.K. Sachdev, S. Godet, Twinning-induced softening in polycrystalline AM30 Mg alloy at moderate temperatures, Scripta Materialia 54(5) (2006) 771-775.

[68] Z.-Z. Shi, Y. Zhang, F. Wagner, T. Richeton, P.-A. Juan, J.-S. Lecomte, L. Capolungo, S. Berbenni, Sequential double extension twinning in a magnesium alloy: Combined statistical and micromechanical analyses, Acta Materialia 96 (2015) 333-343.

[69] S.H. Park, S.-G. Hong, C.S. Lee, Activation mode dependent {10−12} twinning characteristics in a polycrystalline magnesium alloy, Scripta Materialia 62(4) (2010) 202-205.

[70] S.H. Park, S.-G. Hong, J.H. Lee, C.S. Lee, Multiple twinning modes in rolled Mg–3Al–1Zn alloy and their selection mechanism, Materials Science and Engineering: A 532 (2012) 401-406.

[71] A. Jäger, A. Ostapovets, P. Molnár, P. Lejček, { }-{ } Double twinning in magnesium, Philosophical Magazine Letters 91(8) (2011) 537-544.

[72] J. Jain, J. Zou, C.W. Sinclair, W.J. Poole, Double tensile twinning in a Mg-8Al-0.5Zn alloy, J Microsc 242(1) (2011) 26-36.

[73] S.-W. Choi, J.W. Won, S. Lee, J.K. Hong, Y.S. Choi, Deformation twinning activity and twin structure development of pure titanium at cryogenic temperature, Materials Science and Engineering: A 738 (2018) 75-80.

[74] F.J. Humphreys, M. Hatherly, Recrystallization and related annealing phenomena, Elsevier2012.

[75] K. Hantzsche, J. Bohlen, J. Wendt, K.U. Kainer, S.B. Yi, D. Letzig, Effect of rare earth additions on microstructure and texture development of magnesium alloy sheets, Scripta Materialia 63(7) (2010) 725-730.

[76] K. Higashida, J. Takamura, N. Narita, The formation of deformation bands in f.c.c. crystals, Materials Science and Engineering 81 (1986) 239-258.

[77] P. Guo, L. Li, X. Liu, T. Ye, S. Cao, C. Xu, S. Li, Compressive deformation behavior and microstructure evolution of AM80 magnesium alloy under quasi-static and dynamic loading, International Journal of Impact Engineering 109 (2017) 112-120.

[78] G.D. Köhlhoff, A.S. Malin, K. Lücke, M. Hatherly, Microstructure and texture of rolled {112}〈111〉 copper single crystals, Acta Metallurgica 36(10) (1988) 2841-2847.

[79] H.L. Kim, J.H. Lee, C.S. Lee, W. Bang, S.H. Ahn, Y.W. Chang, Shear band formation during hot compression of AZ31 Mg alloy sheets, Materials Science and Engineering: A 558 (2012) 431-438.

[80] K. Atik, M. Efe, Twinning-induced shear banding and its control in rolling of magnesium, Materials Science and Engineering: A 725 (2018) 267-273.

[81] Y.B. Chun, C.H.J. Davies, Texture effects on development of shear bands in rolled AZ31 alloy, Materials Science and Engineering: A 556 (2012) 253-259.

[82] D. Guan, W.M. Rainforth, J. Gao, L. Ma, B. Wynne, Individual effect of recrystallisation nucleation sites on texture weakening in a magnesium alloy: Part 2- shear bands, Acta Materialia 145 (2018) 399-412.

[83] S.V. Zherebtsov, G.S. Dyakonov, A.A. Salem, V.I. Sokolenko, G.A. Salishchev, S.L. Semiatin, Formation of nanostructures in commercial-purity titanium via cryorolling, Acta Materialia 61(4) (2013) 1167-1178.

[84] T. Obara, H. Yoshinga, S. Morozumi, {1122}〈1123〉 Slip system in magnesium, Acta Metallurgica 21(7) (1973) 845-853.

[85] F. Zarandi, S. Yue, Magnesium Sheet; Challenges and Opportunities, Magnesium Alloys-Design, Processing and Properties, InTech2011.

[86] J. Jain, W.J. Poole, C.W. Sinclair, The deformation behaviour of the magnesium alloy AZ80 at 77 and 293K, Materials Science and Engineering: A 547 (2012) 128-137.

[87] F. Kabirian, A.S. Khan, T. Gnäupel-Herlod, Visco-plastic modeling of mechanical responses and texture evolution in extruded AZ31 magnesium alloy for various loading conditions, International Journal of Plasticity 68 (2015) 1-20.

[88] Y. Zhang, N.R. Tao, K. Lu, Effect of stacking-fault energy on deformation twin thickness in Cu–Al alloys, Scripta Materialia 60(4) (2009) 211-213.

[89] M.H. Yoo, Slip, twinning, and fracture in hexagonal close-packed metals, Metallurgical Transactions A 12(3) (1981) 409-418.

[90] R.D. Doherty, D.A. Hughes, F.J. Humphreys, J.J. Jonas, D.J. Jensen, M.E. Kassner, W.E. King, T.R. McNelley, H.J. McQueen, A.D. Rollett, Current issues in recrystallization: a review, Materials Science and Engineering: A 238(2) (1997) 219-274.

[91] Z.R. Zeng, Y.M. Zhu, S.W. Xu, M.Z. Bian, C.H.J. Davies, N. Birbilis, J.F. Nie, Texture evolution during static recrystallization of cold-rolled magnesium alloys, Acta Materialia 105 (2016) 479-494.

[92] X. Li, P. Yang, L.N. Wang, L. Meng, F. Cui, Orientational analysis of static recrystallization at compression twins in a magnesium alloy AZ31, Materials Science and Engineering: A 517(1-2) (2009) 160-169.

[93] D. Guan, W.M. Rainforth, L. Ma, B. Wynne, J. Gao, Twin recrystallization mechanisms and exceptional contribution to texture evolution during annealing in a magnesium alloy, Acta Materialia 126 (2017) 132-144.

[94] H. El Kadiri, C.D. Barrett, J. Wang, C.N. Tomé, Why are {101¯2} twins profuse in magnesium?, Acta Materialia 85 (2015) 354-361.

[95] K.D. Molodov, T. Al-Samman, D.A. Molodov, Profuse slip transmission across twin boundaries in magnesium, Acta Materialia 124 (2017) 397-409.

[96] T. Al-Samman, K.D. Molodov, D.A. Molodov, G. Gottstein, S. Suwas, Softening and dynamic recrystallization in magnesium single crystals during c-axis compression, Acta Materialia 60(2) (2012) 537-545.

[97] K.D. Molodov, T. Al-Samman, D.A. Molodov, G. Gottstein, Mechanisms of exceptional ductility of magnesium single crystal during deformation at room temperature: Multiple twinning and dynamic recrystallization, Acta Materialia 76 (2014) 314-330.

[98] T. Al-Samman, G. Gottstein, Dynamic recrystallization during high temperature deformation of magnesium, Materials Science and Engineering: A 490(1-2) (2008) 411-420.

[99] L.M. Technologies, TEST REPORT/ CERTIFICATE OF CONFORMANCE, Luxfer MEL Technologies 2018.

[100] S. Kurukuri, M.J. Worswick, D. Ghaffari Tari, R.K. Mishra, J.T. Carter, Rate sensitivity and tension-compression asymmetry in AZ31B magnesium alloy sheet, Philos Trans A Math Phys Eng Sci 372(2015) (2014) 20130216.

[101] Standard Practice for Compression Tests of Metallic Materials at Elevated Temperatures with Conventional or Rapid Heating Rates and Strain Rates.

[102] A.J. Schwartz, M. Kumar, B.L. Adams, D.P. Field, Electron backscatter diffraction in materials science, Springer2000.

[103] G. Liu, S. Winwood, K. Rhodes, S. Birosca, The effects of grain size, dendritic structure and crystallographic orientation on fatigue crack propagation in IN713C nickel-based superalloy, International Journal of Plasticity 125 (2020) 150-168.

[104] Y. Guo, H. Abdolvand, T.B. Britton, A.J. Wilkinson, Growth of {112¯2} twins in titanium: A combined experimental and modelling investigation of the local state of deformation, Acta Materialia 126 (2017) 221-235.

[105] A.J. Wilkinson, T.B. Britton, Strains, planes, and EBSD in materials science, Materials Today 15(9) (2012) 366-376.
[106] S. Birosca, G. Liu, R. Ding, J. Jiang, T. Simm, C. Deen, M. Whittaker, The dislocation behaviour and GND development in a nickel based superalloy during creep, International Journal of Plasticity 118 (2019) 252-268.
[107] J. Jiang, T.B. Britton, A.J. Wilkinson, Evolution of dislocation density distributions in copper during tensile deformation, Acta Materialia 61(19) (2013) 7227-7239.
[108] M.F. Ashby, The deformation of plastically non-homogeneous materials, Philosophical Magazine 21(170) (1970) 399-424.
[109] H. Gao, Y. Huang, Geometrically necessary dislocation and size-dependent plasticity, Scripta Materialia 48(2) (2003) 113-118.
[110] M. Calcagnotto, D. Ponge, E. Demir, D. Raabe, Orientation gradients and geometrically necessary dislocations in ultrafine grained dual-phase steels studied by 2D and 3D EBSD, Materials Science and Engineering: A 527(10-11) (2010) 2738-2746.
[111] N. Allain-Bonasso, F. Wagner, S. Berbenni, D.P. Field, A study of the heterogeneity of plastic deformation in IF steel by EBSD, Materials Science and Engineering: A 548 (2012) 56-63.
[112] C. Moussa, M. Bernacki, R. Besnard, N. Bozzolo, About quantitative EBSD analysis of deformation and recovery substructures in pure Tantalum, IOP Conference Series: Materials Science and Engineering 89 (2015).
[113] C.K. Yan, A.H. Feng, S.J. Qu, G.J. Cao, J.L. Sun, J. Shen, D.L. Chen, Dynamic recrystallization of titanium: Effect of pre-activated twinning at cryogenic temperature, Acta Materialia 154 (2018) 311-324.
[114] S. Suwas, R.K. Ray, Representation of Texture, Crystallographic Texture of Materials2014, pp. 11-38.
[115] S.M. Fatemi-Varzaneh, A. Zarei-Hanzaki, H. Beladi, Dynamic recrystallization in AZ31 magnesium alloy, Materials Science and Engineering: A 456(1-2) (2007) 52-57.
[116] R.K. Mishra, A.K. Gupta, P.R. Rao, A.K. Sachdev, A.M. Kumar, A.A. Luo, Influence of cerium on the texture and ductility of magnesium extrusions, Scripta Materialia 59(5) (2008) 562-565.
[117] O. El Fakir, L. Wang, D. Balint, J.P. Dear, J. Lin, T.A. Dean, Numerical study of the solution heat treatment, forming, and in-die quenching (HFQ) process on AA5754, International Journal of Machine Tools and Manufacture 87 (2014) 39-48.

[118] I.J. Beyerlein, L. Capolungo, P.E. Marshall, R.J. McCabe, C.N. Tomé, Statistical analyses of deformation twinning in magnesium, Philosophical Magazine 90(16) (2010) 2161-2190.

[119] S.H. Park, J.H. Lee, B.G. Moon, B.S. You, Tension–compression yield asymmetry in as-cast magnesium alloy, Journal of Alloys and Compounds 617 (2014) 277-280.

[120] A. Ghaderi, F. Siska, M.R. Barnett, Influence of temperature and plastic relaxation on tensile twinning in a magnesium alloy, Scripta Materialia 69(7) (2013) 521-524.

[121] Y.N. Wang, J.C. Huang, Texture analysis in hexagonal materials, Materials Chemistry and Physics 81(1) (2003) 11-26.

[122] J. Wang, I.J. Beyerlein, C.N. Tomé, An atomic and probabilistic perspective on twin nucleation in Mg, Scripta Materialia 63(7) (2010) 741-746.

[123] L. Capolungo, I.J. Beyerlein, Nucleation and stability of twins in hcp metals, Physical Review B 78(2) (2008).

[124] S. Yi, J. Bohlen, F. Heinemann, D. Letzig, Mechanical anisotropy and deep drawing behaviour of AZ31 and ZE10 magnesium alloy sheets, Acta Materialia 58(2) (2010) 592-605.

[125] G. Proust, C.N. Tomé, A. Jain, S.R. Agnew, Modeling the effect of twinning and detwinning during strain-path changes of magnesium alloy AZ31, International Journal of Plasticity 25(5) (2009) 861-880.

[126] C.H. Cáceres, P. Lukáč, A. Blake, Strain hardening due to {10 12} twinning in pure magnesium, Philosophical Magazine 88(7) (2009) 991-1003.

[127] J. Koike, Enhanced deformation mechanisms by anisotropic plasticity in polycrystalline Mg alloys at room temperature, Metallurgical and Materials Transactions A 36(7) (2005) 1689-1696.

[128] O. Bouaziz, N. Guelton, Modelling of TWIP effect on work-hardening, Materials Science and Engineering: A 319-321 (2001) 246-249.

[129] I.J. Beyerlein, C.N. Tomé, A dislocation-based constitutive law for pure Zr including temperature effects, International Journal of Plasticity 24(5) (2008) 867-895.

[130] X.D. Jiao, Mechanical Properties of Low Density Alloys at Cryogenic Temperatures, AIP Conference Proceedings, 2006, pp. 69-76.

[131] W. He, X. Chen, N. Liu, B. Luan, G. Yuan, Q. Liu, Cryo-rolling enhanced inhomogeneous deformation and recrystallization grain growth of a zirconium alloy, Journal of Alloys and Compounds 699 (2017) 160-169.

[132] L. Mao, C. Liu, T. Chen, Y. Gao, S. Jiang, R. Wang, Twinning behavior in a rolled Mg-Al-Zn alloy under dynamic impact loading, Scripta Materialia 150 (2018) 87-91.
[133] D.-X. Wei, Y. Koizumi, M. Nagasako, A. Chiba, Refinement of lamellar structures in Ti-Al alloy, Acta Materialia 125 (2017) 81-97.
[134] M. Arul Kumar, I.J. Beyerlein, C.N. Tomé, Effect of local stress fields on twin characteristics in HCP metals, Acta Materialia 116 (2016) 143-154.
[135] A. Duckham, R.D. Knutsen, O. Engler, Influence of deformation variables on the formation of copper-type shear bands in Al–1Mg, Acta Materialia 49(14) (2001) 2739-2749.
[136] P. Changizian, A. Zarei-Hanzaki, M. Ghambari, A. Imandoust, Flow localization during severe plastic deformation of AZ81 magnesium alloy: Micro-shear banding phenomenon, Materials Science and Engineering: A 582 (2013) 8-14.
[137] H.Y. Chao, H.F. Sun, W.Z. Chen, E.D. Wang, Static recrystallization kinetics of a heavily cold drawn AZ31 magnesium alloy under annealing treatment, Materials Characterization 62(3) (2011) 312-320.
[138] B.R. Chen, A.C. Yeh, J.W. Yeh, Effect of one-step recrystallization on the grain boundary evolution of CoCrFeMnNi high entropy alloy and its subsystems, Sci Rep 6 (2016) 22306.
[139] C.W. Su, L. Lu, M.O. Lai, Recrystallization and grain growth of deformed magnesium alloy, Philosophical Magazine 88(2) (2008) 181-200.
[140] É. Martin, R.K. Mishra, J.J. Jonas, Effect of twinning on recrystallisation textures in deformed magnesium alloy AZ31, Philosophical Magazine 91(27) (2011) 3613-3626.

Appendix A. Grain size distribution and texture in the hot-deformed samples

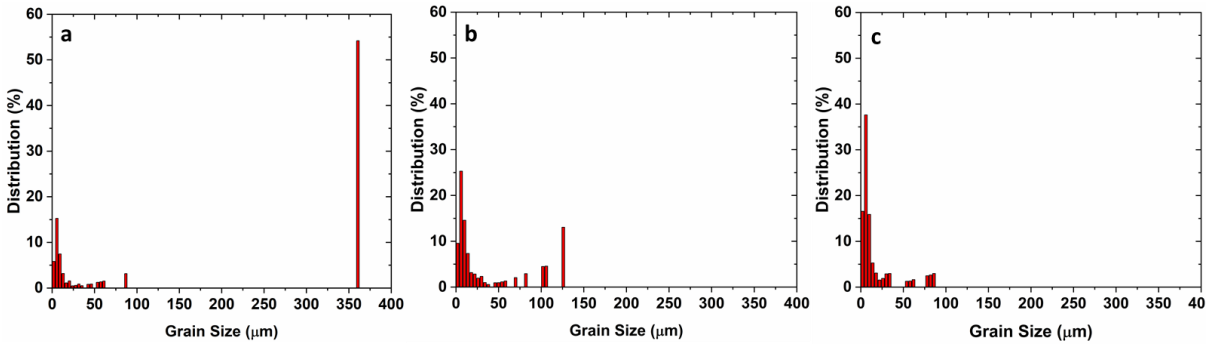

Figure A.1 Grain size distribution in the (a) direct-HD, (b) RT-HD, and (c) CT-HD samples.

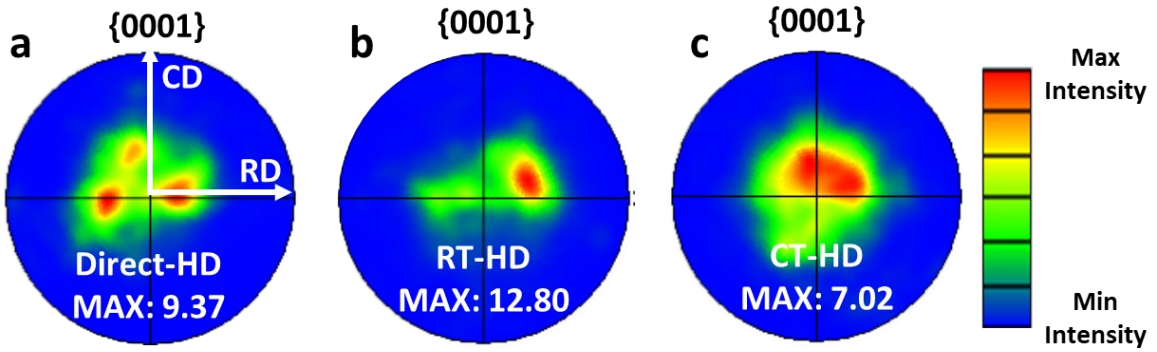

Figure A.2 {0001} pole figures in fine-grained zones of (a) direct-HD sample, (b) RT-HD sample, and (c) CT-HD sample. The unit of the colour bar is in multiples of a uniform distribution (mud).

Appendix B. The microstructure during the RT-rolling and CT-rolling processes

Appendix I. Enlarged optical images in the 3% and 13% RT-rolled samples

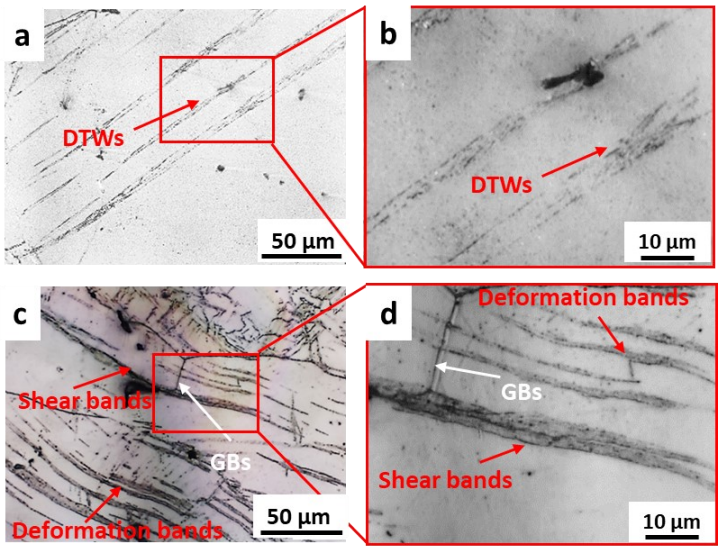

Figure B.1 Optical images and the corresponding enlarged images of the RT-rolled sample with a total TR of (a-b) 3% and (c-d) 13%.

Appendix II. IPF maps, band contrast maps, optical images and KAM maps in the 9% RT-rolled and CT-rolled samples

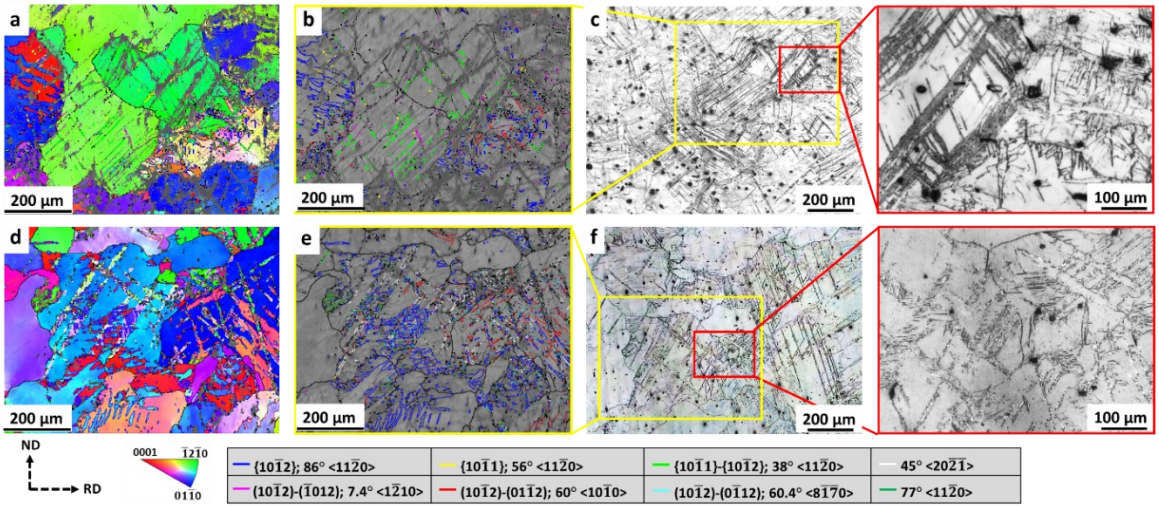

Figure B.2 EBSD analysis of the (a-c) RT-rolled and (d-f) CT-rolled AZ31 samples with a total TR of 9%. (a) and (d) EBSD IPF maps. (b) and (e) band contrast maps with twin boundaries. (c) and (f) optical images with the corresponding enlarged images.

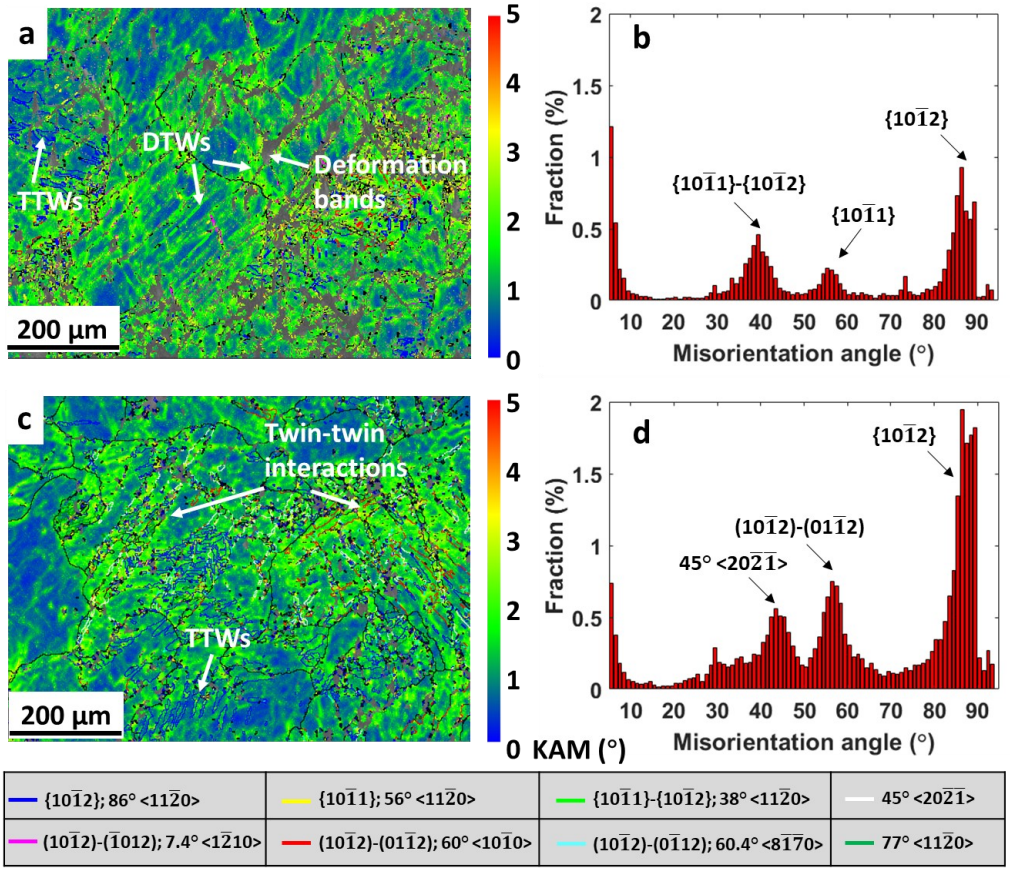

Figure B.3 KAM maps of (a) RT-rolled and (c) CT-rolled samples with a TR of 9%, and (b, d) their corresponding misorientation distributions, respectively.

Appendix III. IPF map, pole figure, and misorientation distribution map of Zone G in the 13% CT-rolled sample

As seen in Supplementary Figure B.4, the boundaries with white colours are 45° <20$\bar{2}\bar{1}$> boundaries, i.e. a 45° misorientation around the <20$\bar{2}\bar{1}$> axis. The peak near 45° in the misorientation distribution map also confirms the existence of these boundaries. The 45° <20$\bar{2}\bar{1}$> boundaries are formed between the primary twin variant G2 and the secondary twin variant G4, which are in good agreement with the results in Figure 6.8.

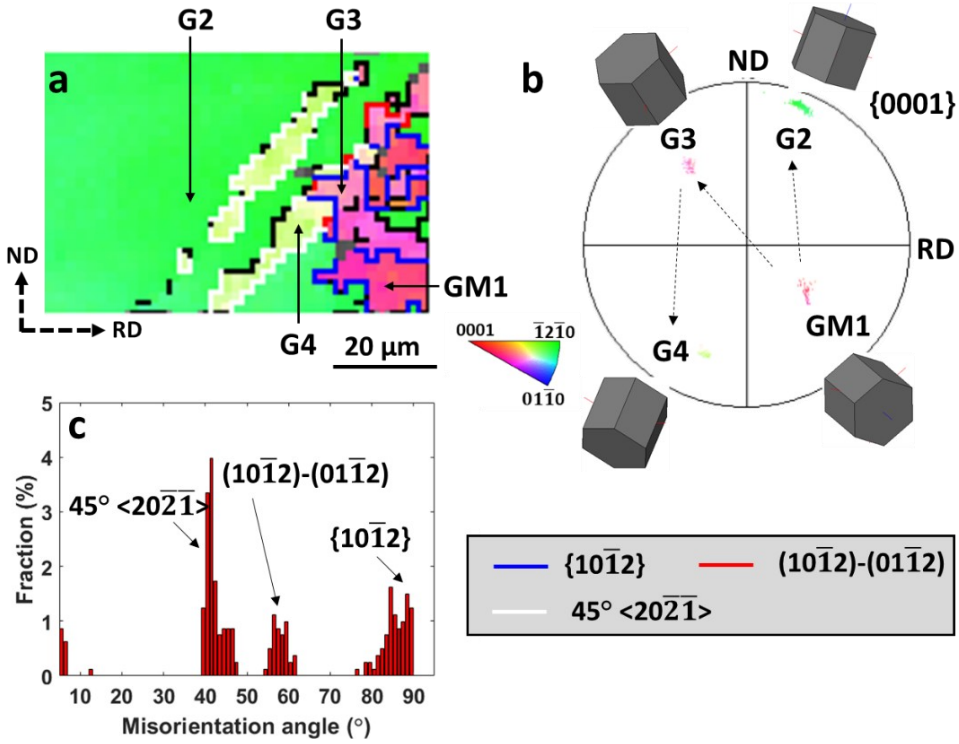

Figure B.4 Detailed microstructure analysis of Zone G in the 13% CT-rolled sample. (a) EBSD IPF map, (b) {0001} pole figure and (c) misorientation distribution map.

Appendix C. The microstructure evolution in the RT-rolled and CT-rolled samples during the annealing process

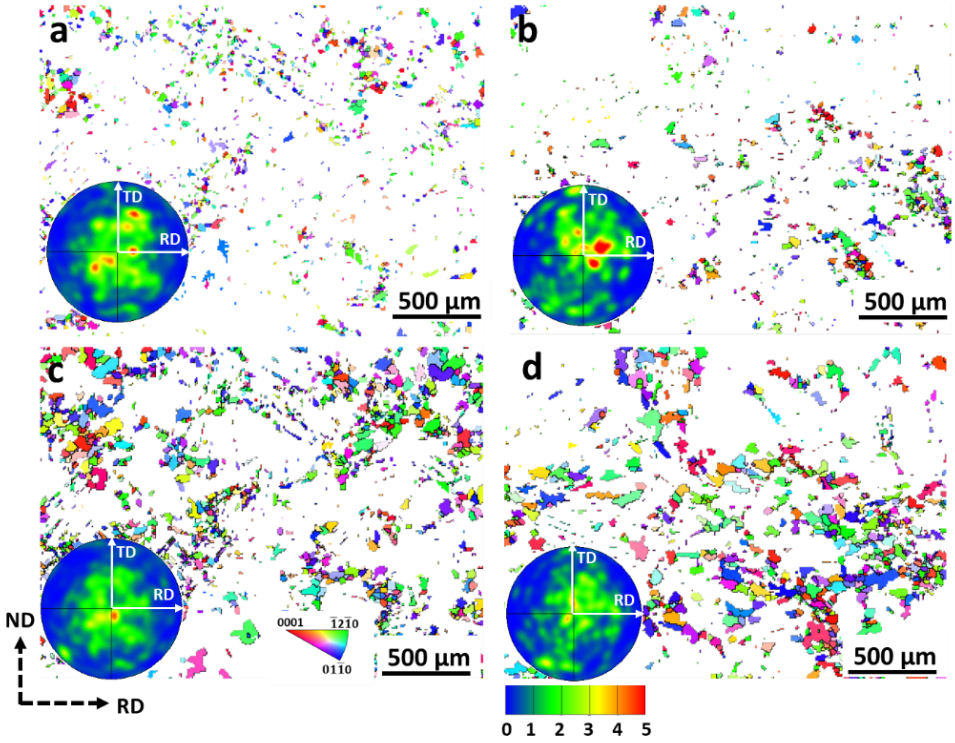

Figure C.1 EBSD IPF maps and {0001} pole figures of the recrystallized grains in the RT-rolled and CT-rolled samples during annealing at 300 °C for (a, b) 5 min, (c, d) 110 min, respectively. The unit of the colour bar is mud.